Doctoral theses at NTNU, 2020:362

Fredrik Eikeland Fossan

Physics-based and data-driven reduced-order blood flow models:

Applications to coronary artery disease diagnostics

Doctoral thesis

Fredrik Eikeland Fossan

ISBN 978-82-326-5070-5 (printed ver.)
ISBN 978-82-326-5071-2 (electronic ver.)
ISSN 1503-8181

NTNU
Norwegian University of Science and Technology

NTNU
Norwegian University of Science and Technology
Thesis for the Degree of
Philosophiae Doctor
Faculty of Engineering
Department of Structural Engineering

Doctoral theses at NTNU, 2020:362

NTNU
Norwegian University of Science and Technology

Fredrik Eikeland Fossan

Physics-based and data-driven reduced-order blood flow models:

Applications to coronary artery disease diagnostics

Thesis for the Degree of Philosophiae Doctor

Trondheim, November 2020

Norwegian University of Science and Technology
Faculty of Engineering
Department of Structural Engineering

NTNU
Norwegian University of
Science and Technology

NTNU
Norwegian University of Science and Technology

Thesis for the Degree of Philosophiae Doctor

Faculty of Engineering
Department of Structural Engineering

ISBN 978-82-326-5070-5 (printed ver.)
ISBN 978-82-326-5071-2 (electronic ver.)
ISSN 1503-8181

Doctoral theses at NTNU, 2020:362

Printed by NTNU Grafisk senter

Preface

This thesis is submitted to the Norwegian University of Science and Technology (NTNU) for partial fulfillment of the requirements for the degree of philosophiae doctor. This doctoral work has been performed at the Department of Structural Engineering, NTNU, Trondheim from September 2016 through August 2020 under the supervision of Leif Rune Hellevik.

This thesis is a collection of papers published in or submitted to international peer-reviewed journals. The thesis is organized in two parts. Part I is an introductory section that presents the themes and background of the thesis and part II includes the journal papers.

Abstract

In this thesis we have developed reduced-order models for the prediction of pressure and flow in the arterial system and for the diagnosis of coronary artery disease. By reduced-order model we refer to a reduction of dimensionality, *i.e.* the conversion of a 3D problem to a 1D problem, or a 1D problem to a 0D problem. The reductions in dimensionality require simplifications of the problem, which are associated with a range of assumptions. These simplifications and assumptions lead to computationally affordable, and thereby clinically relevant models, which may be used for diagnosis, treatment and decision support. However, these benefits have to be counterweighted with the model errors introduced by the simplifications and assumptions, to maintain the clinically relevant predictability of the models.

We have developed a framework for optimizing the number of segments to be included in arterial 1D blood flow models. We found that a model where all aortic segments are represented, but with a minimal description of other parts of the cardiovascular system (head and extremities), is sufficient to capture important features of the aortic pressure waveform.

Furthermore, we have developed a noninvasive reduced-order model for the estimation of the hemodynamic significance of coronary artery disease, based on coronary computed tomography angiography (CCTA) imaging and computational fluid dynamics. We demonstrated how global sensitivity analysis can be used as a part of model validation and assist in parameter estimation to reduce errors with respect to a corresponding, more detailed 3D model. Moreover, the errors related to the reduced-order model were further reduced by application of neural networks for prediction of pressure loss in coronary segments. We evaluated the effect of incorporating prior physics-based knowledge in the learning process. This modification resulted in significantly improved predictions by the neural networks and also reduced the amount of training data required to achieve a specific accuracy.

We characterized the diagnostic accuracy of the reduced-order model to classify ischemia using invasive Fractional Flow Reserve (FFR) measurements as reference. Our model predictions of FFR obtained an accuracy, sensitivity and specificity of 89%, 79% and 93% respectively, in an unblinded study on 63 patients. Moreover, we found that the estimation and distribution of baseline coronary flow had a significant impact on diagnostic performance. However, even imposition of the correct baseline flow would still lead to high uncertainty in predicted FFR due to uncertainties related to geometry and the effect of hyperemic inducing drugs.

Acknowledgments

There are many people I would like to thank for this PhD. First of all I would like to thank my main supervisor, Leif Rune Hellevik for providing me with the possibility to work at the division of biomechanics. Thank you for your (contagious) passion for cardiovascular biomechanics, your open mindedness and for your abilities to provide a joyful and positive working environment. I would also like to thank you for all the discussions and guidance throughout this thesis.

I would also like to give a special thanks to my co-supervisor Lucas Omar Müller, for your essential work in the FFR-project. Your contributions to this thesis has been fundamental. Thank you for your kindness and also for your ability to be cruel to be kind. I would like to thank you, my other co-supervisor Hans Torp, and also Rune Wiseth for all the discussions and guidance throughout this thesis, and for your efforts in establishing and coordinating the FFR-project.

I would also like to give a special thanks to cardiologist and colleague Anders Tjellaug Bråten. Thank you for all the meetings and Facetime discussions and for your ways of giving me insights into the clinical practice of coronary artery disease. Your efforts in coordinating the recruitment of patients have been fundamental for this thesis. Thank you for your passion and for your willingness to learn about and question computational models of the cardiovascular system. I would also like to thank radiologist Arve Jørgensen, for all your work and contributions to the project and this thesis. I would also like to thank Stefano Fiorentini, Frank Lindseth and the other collaborators in the FFR-project, for providing a great interdisciplinary working environment. Moreover, I would like to thank all nurses and doctors at St. Olavs hospital who have helped with examinations of recruited patients, and a special thanks is given to Erik Andreas Rye Berg and Espen Holte for performing ultrasound examinations.

I would like to thank my friends and colleagues, Andreas Strand, Nikolai Lid Bjørdalsbakke and in particular Jacob Sturdy. Thank you for all discussions, contributions and collaborations throughout this PhD. I would also like to thank Bjørn Helge Skallerud and Viktorien Emile Prot for your work and passion for the division of Biomechanics. I would like to thank you and the rest of the colleagues at the department of Structural Engineering for providing a good learning and working environment.

I would like to thank Jordi Alastruey and Jordi Mariscal-Harana at King's College London for the interesting collaboration and discussions that culminated in the first paper of my PhD.

I would also like to give a special thanks to my girlfriend Ingrid, for your love and support during this thesis. Thank you for your interest and enthusiasm for my work. I would also like to thank my family and especially my mom and dad, Reidun and Rune, for all your support and care.

List of papers

Journal papers

Paper 1: Optimization of topological complexity for one-dimensional arterial blood flow models
F.E. Fossan, J. Mariscal-Harana, J. Alastruey, L.R. Hellevik

Published in *Journal of the Royal Society Interface*, 2018.

Paper 2: Uncertainty Quantification and Sensitivity Analysis for Computational FFR Estimation in Stable Coronary Artery Disease
F.E. Fossan, J. Sturdy, L.O. Müller, A. Strand, A. Bråten, A. Jørgensen, R. Wiseth, L.R. Hellevik
Published in *Cardiovascular Engineering and Technology*, 2018.

Paper 3: Impact of baseline coronary flow and its distribution on fractional flow reserve prediction
L.O. Müller, F.E. Fossan, A. Bråten, A. Jørgensen, R. Wiseth, L.R. Hellevik

Published in the *International Journal of Numerical Methods in Biomedical Engineering*, 2019.

Paper 4: Machine learning augmented reduced order models for FFR-prediction
F.E. Fossan, L.O. Müller, J. Sturdy, A. Bråten, A. Jørgensen, R. Wiseth, L.R. Hellevik
Submitted to *Computer Methods in Applied Mechanics and Engineering*, 2020.

Other contributions

Compensating for flow to side branches does not affect computed fractional flow reserve but is significant for other indices in coronary artery disease
R. Gosling, J. Sturdy, P.D. Morris, F.E. Fossan, L.R. Hellevik, P. Lawford, D.R. Hose, J. Gunn
Published in *Journal of Biomechanics*, 2020.

Contents

Part I

Introductory section

Nomenclature

0D - Zero dimensional

1D - One dimensional

3D - Three dimensional

CAD - Coronary artery disease

CCTA - Coronary computed tomography angiography

FFR - Fractional Flow Reserve

ICA - Invasive coronary angiography

ROM - Reduced-order model

SA - Sensitivity analysis

UQ - Uncertainty quantification

Chapter 1

Introduction

This thesis was conducted at the Department of Structural Engineering at the Norwegian University of Science and Technology, with focus on the cardiovascular system (*i.e.* the heart and blood vessels) and with a particular emphasis put on the development of a non-invasive model for assessing the significance of coronary artery disease. At first it might seem odd to conduct such a PhD at a department which core is to study the strengths, mechanics and dynamics of man made systems and structures. However, a link is made by the term biomechanics, which relates to the study of the structure and function of biological (*i.e.* living) systems. Similar to the way Newtons 2nd law of motion is used to predict stresses and deformations in man made structures, it may also be used to predict pressure and flow distribution in the heart and blood vessels that comprise the cardiovascular system of the human body.

The cardiovascular system is a critical system, which primary function is to provide rapid convective transport of oxygen, nutrients etc. to the tissues, and corresponding washout of metabolic waste products from the tissues [1]. The cardiovascular system consists of the heart, which is the driving force (pump) of the system, arteries, which provide a passage of the blood from the heart to the tissues, and veins, which direct blood back towards the heart. Arteries and veins are blood vessels, and in order to provide exchange of oxygen, waste products etc. to all the tissues and cells of the body, they form branching networks with countless number of vessels[1]. The size of the vessels and mechanical properties of the vessels'

[1] Most cells lie within 20 μm of a blood vessel. At this distance, diffusion takes over as the means of transport of oxygen, waste products etc to/from the tissues/cells [1].

walls are different depending on their purpose and distance from the heart. They may have large diameters ($\sim 1\,\mathrm{cm}$), be thin-walled and elastic with the primary purpose of serving as conduits for the rest of the network. They may have thick muscular walls allowing the diameter to vary greatly. They may have tiny diameters ($\sim 5\,\mu\mathrm{m}$) with vessel walls consisting of a single layer of cells that allow easy transfer of nutrients and oxygen to nearby tissues. Moreover, the cardiovascular system needs to respond to increased metabolic needs, such as exercise, which is achieved by increased (heart) pumping frequency and power, increased exchange of dissolved oxygen, or by increase of vessels' diameter (and thereby increasing their inductance). Although the cardiovascular system is the first organ system to form in the embryo, it changes and evolves in response to hemodynamic and genetic influences. This continues throughout a persons lifetime also in response to disease and aging, with the result that no two systems are the same.

In other words, the cardiovascular system is complex, and at first it may seem naive to try to represent it through mathematical modeling, particularly in cases with ambition of adopting such models in clinical scenarios. In this context however, it is important to acknowledge that many of the challenges that a modeler faces in attempts to construct models for clinical application are also faced by clinicians practicing current guidelines. Typically, the diagnosis of cardiovascular disease involves a synthesis of subjective patient symptoms and clinical examinations, such as blood tests and clinical imaging (ultrasound, CCTA etc.). This is further combined with epidemiology, clinical experience and probability assessment, which guide further examinations and treatments [2]. Furthermore, recommendations for decision making and treatment planning are commonly based on binary cut offs[2], a strategy that has both benefits and drawbacks. While it offers ease of interpretation and can facilitate efficient decision making it might also suppress important patient and case variabilities and therefore introduce diagnostic inaccuracies. As such, the current paradigm of evidence based medicine is to a large extent based on population based studies, that have proven favorable outcomes for the population as a whole (and in terms of costs), but not necessarily for the individual patient [2].

Cardiovascular diseases are the leading causes of deaths in the world [3, 4], primarily driven by deaths caused by coronary artery disease (CAD) and stroke. Cardiovascular diseases thus represent a massive public health problem, also in terms of cost [5]. This in turn has motivated research towards the development of models of the cardiovascular system which, despite its challenges, has led to increased knowledge of its related physiology and pathology [6–11]. These models vary

[2]For instance, a stenosis (narrowing) of a coronary artery that cause a reduction of flow of more than 20 % measured by Fractional Flow Reserve normally recommends revascularization by intervention.

in complexity from simple electrical analogue circuit models, that represent the cardiovascular system with a handful of parameters [6], to complex multi-scale models that couple the cardiac electro-physiology system affecting the contractility of muscle tissues, with the hemodynamics (pressure and flow) of the heart [11], and of arterial network models that include thousands of arterial vessels [10]. As such, the research community has come a long way in the design of realistic and detailed models that continue to shed light on the interplay between mechanical properties of the vessel and cardiac walls, morphology, anatomy and hemodynamics, and their relation to cardiovascular diseases. Despite this, the impact and use of such models in clinical practice is modest [2].

The development of models that are able to describe the properties of the cardiovascular system is challenging. In application of such models in clinical practice however, a perhaps greater challenge is faced when such models are intended to predict the behavior or properties of a particular individual. This process is performed by using clinical records and measurements (*e.g.* blood tests, blood pressure, ultrasound, CCTA etc.) to parametrize the model. However, clinical measurements are uncertain and may not contain the correct spatial or temporal resolution, may not directly measure the correct quantities or may be performed in different hemodynamic conditions (*i.e.* normally at rest and in sitting or supine position), necessary to uniquely parametrize the model. Thus, in the same way as assumptions have to be made during the model design (*i.e.* the choice of governing equations that represent the physics of blood flow and the mechanical behavior of the vessel wall, the level of detail of the arterial networks etc.), assumptions related to the input parameters of the model (*i.e.* the viscosity of blood, the stiffness of the vessel walls etc.) will also have to be made. As a result, the model errors can be separated into those resulting from the model framework, and those caused by uncertainties of model input-parameters. As illustrated in Figure 1.1, the errors related to the model framework generally decreases with the complexity of the model as the ability to capture the physics of the system is improved. However, along with the increased complexity, the model will normally require an increase in the number of input-parameters. If these parameters are unknown and have large uncertainties, the increased complexity of the model might result in larger overall error due to increased uncertainty in predictions.

Despite the above mentioned challenges, cardiovascular models may provide additional information and predict unmeasured patient-specific properties and quantities. For example, models can predict quantities that would normally require invasive measurements, and thus serve as useful tools for clinicians in a new paradigm of patient-specific medicine. However, cardiovascular models will inevitably have limitations in terms of the model complexity (*i.e.* how well the physics is modeled)

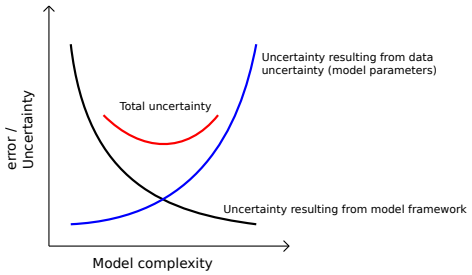

Figure 1.1: Illustration of the total uncertainty of a model prediction, which is the sum of uncertainties related to the model framework and of uncertainties related to input data (measurements etc). Figure was reprinted from [12].

and in terms of the uncertainties in the predicted quantities. Hence, in order to be useful it is important to be aware of these limitations and the primary sources of errors.

In this thesis we have focused on the development of methods and models for the prediction of pressure and flow in the cardiovascular system, with particular emphasis put on pressure losses over coronary stenoses. Moreover, great attention has been put on the development of simplified models that are still able to represent the most important features of the physical system, and where the effect of the simplifications are quantified by comparison with corresponding, more detailed models. For instance, in Paper 1, a method to optimize the number of arterial segments included in one-dimensional blood flow models, while preserving key features of flow and pressure waveforms, was presented. Further, in Papers 2-4 a reduced-order model for prediction of the severity of coronary artery disease, was presented. The latter model was developed as part of an interdisciplinary project with engineers at NTNU and clinicians at St. Olavs hospital, with the aim of developing a non-invasive diagnostic tool for coronary artery disease. The model combines 1D axi-symmetric theory of blood flow, experimental relations and machine learning (neural networks). Throughout papers 2-4 special focus was given to minimize the errors between the reduced-order model and a corresponding, more complex model which builds on the 3D incompressible Navier-Stokes equations.

The simplifications and assumptions introduced by model reduction results in a reduction in the number of model parameters and/or simplified pre- and post-processing, and reduced computational costs. These benefits, however, have to

be counter-balanced with the model errors introduced by the simplifications and assumptions. Another benefit of the reduced computational time and simplified pre- and post-processing is that this facilitates the applications of uncertainty quantification (UQ) and sensitivity analysis (SA). UQ and SA are crucial methods for determining errors related to input-uncertainty (*i.e.* uncertainties in outlet boundary conditions and model parameters). The latter was given special attention in papers 2 and 3.

The thesis consists of a collection of papers and is divided into two parts. The first part is an introductory section and consists of Chapters 1-5. A brief introduction to aspects of the cardiovascular system and of the coronary circulation which are relevant for this thesis is given in Chapter 2. Chapter 3 includes a brief description of the methods used in this thesis, including physics based computational models, a brief overview of machine learning and artificial neural networks, and methods for uncertainty quantification and sensitivity analysis. In Chapter 4 a summary of the appended papers is given, accompanied with the main conclusion drawn from the thesis and directions for further work in Chapter 5. The second part of the thesis includes Chapters 6-9 which consists of the appended papers.

Chapter 2

Background

This chapter gives a brief introduction to the components of the cardiovascular system which are relevant for this thesis. Special attention is given to coronary physiology and pathology. For a more detailed introduction the reader is referred to [1], which is also the primary source for this chapter.

The cardiovascular system consist of the heart, arteries, veins and the circulating blood. The blood is transported in two separate circuits, namely the pulmonary and systemic circuits. An overview of the cardiovascular system is shown schematically in Figure 2.1(a), and the heart, its chambers, valves and main connections to the systemic and pulmonary circulation is shown in Figure 2.1(b). The pulmonary circuit carries deoxygenated blood from the right ventricle via the pulmonary arteries, to the lungs and returns with oxygenated blood to the left atrium via the pulmonary veins. The systemic circulation transports oxygenated blood throughout the body via the systemic arterial tree, and brings deoxygenated blood from the tissues back to the heart via the systemic veins.

2.1 The heart and the cardiac cycle

The cardiac cycle is commonly separated into two phases, systole and diastole. The systole (of the systemic circulation) is initiated by the polarization of the left ventricle which at this time has filled up its chamber with oxygenated blood from the left atrium via the mitral valve. The polarization quickly results in the contraction of muscle fibers which increases the pressure in the left ventricle. This causes a gradient between the pressure in the left ventricle and the left atrium and closure of the mitral valve. The second valve of the ventricle, namely the aortic valve, is

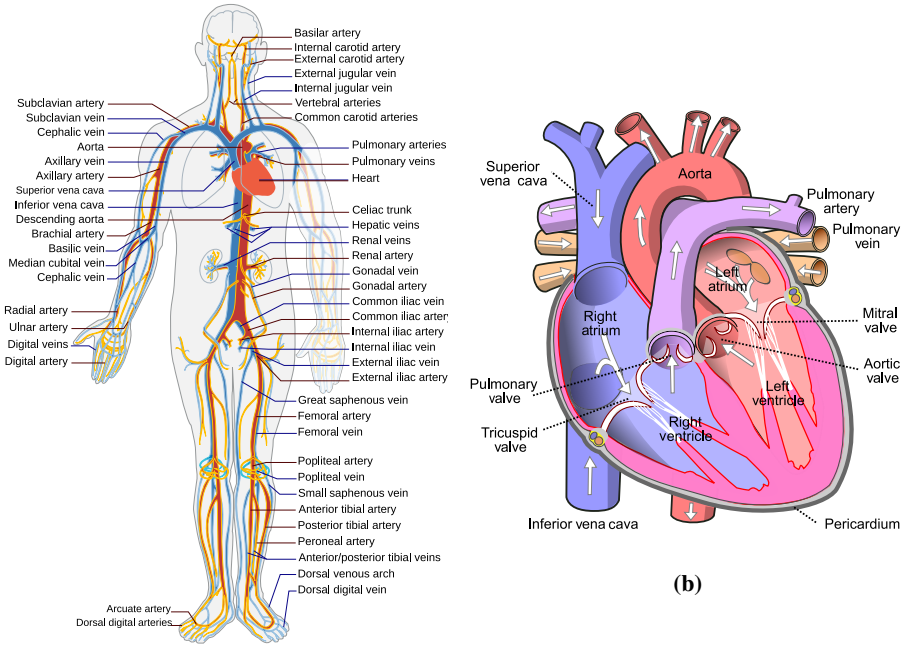

Figure 2.1: (a) Schematic of the cardiovascular system. The heart, largest arteries (red) and veins (blue) are shown. Drawn by Mariana Ruiz Villarreal [13] (b) Diagram of the chambers and valves of the heart [14]. Used with permission CC BY 4.0.

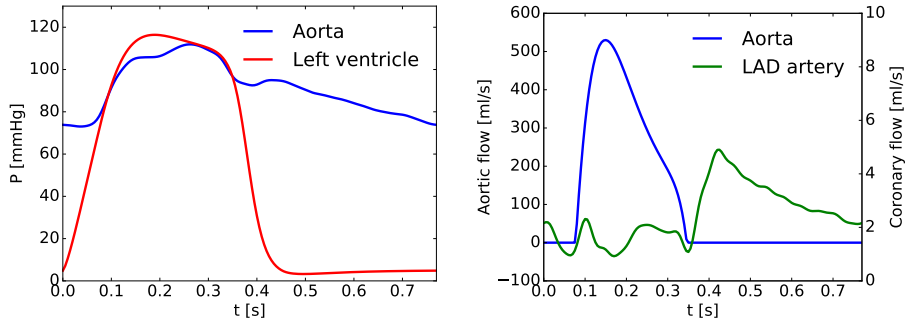

Figure 2.2: Pressure in the aorta and left ventricle (left) and flow in the aorta and the Left anterior descending artery (right) during a cardiac cycle.

closed at this time. The fixed volume and contraction of the muscle fibers causes a rapid increase in ventricular pressure, as shown in the left part of Figure 2.2. When the pressure rises above the aortic pressure, the aortic valve opens, and blood is ejected from the ventricle. The pressure in the ventricle and aorta continue to rise, and the ejection of blood shortly after reaches its maximum flow. A substantial proportion of the ejected volume of blood is stored in the aorta and larger conduit arteries as they expand elastically, until the aortic pressure reaches its maximum value, slightly after maximum flow is reached. Towards the end of systole, the left ventricle starts to relax resulting in falling pressures in the left ventricle and aorta. Once the pressure in the ventricle falls below the aortic pressure, the aortic valve closes which marks the onset of diastole. The pressure in the ventricle continues to fall quickly as the muscles relax, until it falls below the pressure in the left atrium, and diastolic filling of the ventricle commence. The aortic pressure, on the other hand, drops slowly as the elastic energy stored in the distended aorta is gradually converted to kinetic energy, as blood flows continuously throughout the arterial tree and into the capillaries.

2.2 Coronary physiology and pathology

An average human heart weighs approximately $275\,\mathrm{g}$, and in order to keep up with the metabolic demands it needs to circulate approximately five liters of blood every minute, which accumulates to 200 million liters and three billion heart beats in the lifespan of a person [1].

The coronary arteries provide the heart muscles with the fuel it needs to restlessly provide the rest of the body with blood and oxygen supply. The coronary arteries consist of two networks, the left and right coronary arteries respectively. Both networks start in the coronary sinus, a slight bulge in the aorta immediately distal

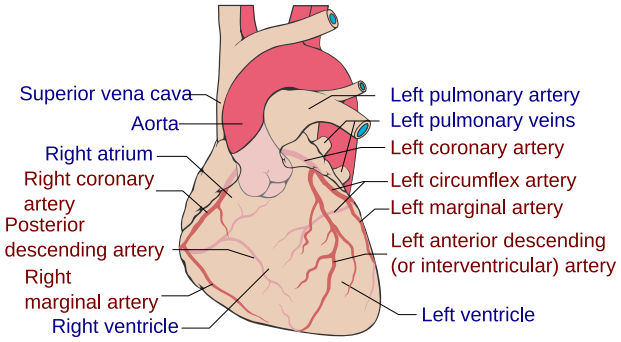

Figure 2.3: The anatomy of the coronary circulation system. Modified from the work of Patrick J. Lynch, medical illustrator derivative work: Fred the Oyster adaption and further labeling: Mikael Häggström - with permission CC BY-SA 3.0.

of the aortic valve. The anatomy of the largest coronary arteries is shown in Figure 2.3. A peculiarity of coronary artery blood flow is characterized by a dominant diastolic flow (see right part of Figure 2.2). During systole, the contracting ventricle pushes on the arteries and impedes flow, despite an open aortic valve. Once the ventricle relaxes however, a substantial pressure gradient from the aorta to the coronary capillaries causes diastolic flow. Thus the elastic storage of blood in the aorta, and the high, slowly decaying diastolic pressure, is critical for the coronary circulation.

The increased metabolic needs caused by intense exercise result in an up to five-fold increase in cardiac output. This is achieved by both increasing the output of each cardiac cycle (stroke volume) and by increased heart rate up to 200 beats per minute. The increased pumping power and frequency also increase the metabolic needs of the cardiac muscles. During increased heart rates the lengths of the two phases of the heart cycle changes disproportionate; the systolic part decreases a bit, from $\sim 0.3\,\mathrm{s}$ to $\sim 0.2\,\mathrm{s}$, while the diastolic phase shortens dramatically from $\sim 0.6\,\mathrm{s}$ to $\sim 0.15\,\mathrm{s}$. This is unfavorable, given the diastolic dominant flow of coronary arteries. Moreover, while most other tissues can increase their uptake of the dissolved oxygen from the blood during exercise, the uptake of oxygen in the myocardial tissues are near maximum levels during rest (~ 70 % vs ~ 20 % in most other tissues). Despite this, the healthy coronary circulation still manages to meet the metabolic needs of the cardiac muscle during exercise, achieved by an increase of coronary blood perfusion by 4-6 times from its resting value. This increase in flow from rest to exercise is commonly denoted coronary flow reserve, and is caused by vasodilation (increase of radius) of the small coronary arteries (arterioles), which allows the blood to flow more easily into the coronary circulation.

2.2.1 Coronary artery disease

Coronary artery disease is caused by atherosclerosis, which is the buildup of fat, esters and other components (plaque) inside the arterial wall, and which is separated from the inner lumen (blood flow) by a fibrous cap [15]. As the diseased state evolves, the plaque volume grows and primarily causes an expansion of the arterial wall area, until it eventually reaches a limit and starts to grow inwards [16], causing a partial obstruction of the lumen (a stenosis), and an impediment of flow/oxygen supply to the tissues (ischemia). Depending on many factors, both local and global, the state may remain partially occluded and give rise to symptoms of exercise induced chest pain and stable angina (stable/chronic CAD), the fibrous cap may rupture exposing the plaque to the inner lumen and blood with successive thrombus formation, causing partial or complete occlusion and unstable angina or myocardial infarction (acute/unstable CAD), or it might remain silent until an unstable event is triggered (asymptomatic CAD).

Stable CAD (chronic coronary syndrome) and acute myocardial infarction are the main manifestations of symptomatic CAD. The differentiation between stable and acute CAD is made based on the severity and timing of the symptoms and on biomarkers related to signs of new myocardial injury (increased troponin levels and ECG changes is typical of acute disease) [17]. This thesis relates to the diagnosis of stable coronary artery thesis, and will hence be given the attention from here on.

Initial diagnosis of stable CAD is based on symptoms (primarily angina), blood tests and traditional risk factors including age, gender, smoking, diabetes, hypertension, cholesterol levels and family history of premature CAD. If initial diagnosis indicates CAD, further tests are needed to quantify the severity of the disease and to decide intervention/treatment. Ultimately a decision of whether the patient should receive a procedure for revascularization or should be treated with medical therapy alone has to be made.

Historically, the invasive diagnosis and treatment of CAD patients have been centered at regional hospitals with Invasive Coronary Angiography (ICA) labs and expert interventionalists. ICA is an x-ray procedure with intracoronary contrast injection that allows for high resolution 2D projections of the coronary arteries. In conventional ICA, the decision for revascularization is left to the operator's discretion assisted by quantification of the degree of narrowing caused by the stenosis. If the degree of narrowing is substantial (*i.e.* larger than 50 %) it is considered significant, and revascularization is normally performed.

The field of cardiology is changing towards increased use of Coronary Computed Tomography Angiography (CCTA), which is noninvasive and offered at most local

hospitals. CCTA uses X-rays in combination with an intravenous injection of an iodine-based contrast agent into the blood. During a CCTA procedure, the heart is imaged from several views (slices), which may be viewed individually or combined to generate a 3D reconstruction of the heart. As in conventional ICA, CCTA allows for the quantification of the anatomical obstruction caused by a stenosis. If a significant stenosis is found on CCTA, the patient is referred to ICA. The use of CCTA received a class 1 recommendation in the 2019 Guidelines for Chronic Coronary Syndromes by the European Society of Cardiology [18].

Revascularization in stable CAD patients is performed to relieve symptoms, restore perfusion and to "stabilize" the plaques as to avoid future events. However, the anatomical obstruction of a stenosis does not directly relate to flow limitation and ischemia [19]. The coronary flow reserve ensures that the heart is supplied with a sufficient amount of blood/oxygen when it is needed (*e.g.* exercise). The presence of an epicardial atheresclorotic lesion introduces an epicardial resistance to flow, which may or may not compromise this reserve. Current guidelines for diagnosis and decision for treatment of stable CAD thus recommend to estimate the extent of reduction in this reserve [18].

2.2.2 Fractional Flow Reserve

Fractional Flow Reserve (FFR) measures the ratio of flow across a stenosis relative to a hypothetical case without stenosis. FFR is currently the gold standard for diagnosis of intermediate stenoses in patients with stable CAD [18]. In the clinic, FFR is measured during invasive coronary angiography by insertion of a catheter with a pressure sensor, and is calculated as the ratio between the cardiac cycled averaged pressure distal and proximal to the stenosis

$$\mathrm{FFR} = \frac{P_d}{P_p},$$

where P_p is normally measured at the ostium(*i.e.* where the coronary tree branches off the aorta). The measurements are performed during hyperemia (maximum coronary flow), which is achieved pharmacologically by administration of a drug that dilates the peripheral coronary arteries. If FFR is below 0.8 the stenosis is considered hemodynamically significant, and it is generally recommended to intervene by percutaneous coronary intervention. If FFR is above 0.8 optimal medical therapy alone is recommended. FFR guided revascularization improves patient outcome and reduces medical costs, both compared to angiography-guided revascularization and medical therapy alone [20, 21]. Despite the European Society of Cardiology's recommendation to use FFR to guide revascularization in chronic CAD patients [18], FFR remains underused due to associated costs, its invasive nature, and the need for trained interventionalists [22].

2.2.3 Noninvasive prediction of FFR

The underuse of invasive FFR in clinical practice has motivated research towards noninvasive prediction of FFR. Noninvasive FFR prediction combines clinical imaging with mathematical models as depicted in Figure 2.4. Different imaging modalities may be used, but CCTA is, perhaps, the most common modality. In the CCTA images, different tissues have different attenuation, and the injected contrast agent in the blood makes the coronary artery lumen particularly visible. By performing imaging processing techniques, the coronary arteries can be isolated (*i.e.* segmented), and a 3D model that represents the patient specific coronary artery anatomy is generated. Based on the anatomical model, assumptions related to the coronary physiology are used to set up a mathematical model including boundary conditions at the inlet and outlets, which form a physiological model. The physiological model typically includes equations that are impossible to solve analytically, and instead computational fluid dynamics (CFD) is used to solve the problem. Once the problem is solved, the pressure and flow in the coronary arteries can be extracted and are further used to predict FFR non-invasively.

Most early attempts of non-invasive FFR prediction relied on solving the incompressible 3D Navier-Stokes equations in segmented coronary arteries [23–25]. This approach requires minimal assumptions related to the physical behavior of blood flow. However, clinical applicability requires fast and accurate predictions, which limits the applicability of full 3D models that typically require tedious preprocessing and significant computational costs.

Recent research aiming to improve clinical applicability of noninvasive FFR prediction, has focused on developing simpler and faster models based on reduced order physics such as 1D blood flow or lumped parameter models [26–29]. More recently machine-learning approaches [30–34] have also been presented.

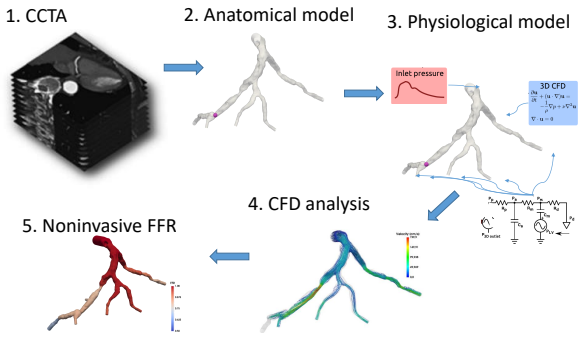

Figure 2.4: Overview of a typical noninvasive FFR prediction pipeline.

Chapter 3

Methods

Physical principles have long been applied to study physiology, and advancements in mathematical and computational models have led to continued growth over the past few decades. This has culminated in the application of physics based computational models in the clinic, such as for diagnosis of CAD [35]. More recently, artificial intelligence and machine learning techniques have gained popularity, and their application may result in a paradigm shift in cardiovascular medicine [36].

This chapter introduces the most important concepts related to mathematical modeling of the cardiovascular system relevant for this thesis. Moreover, a brief description of machine learning and artificial neural networks, which are relevant for Paper 4 are also given. Finally, a brief description of the methods used to quantify the uncertainty related to model inputs and perform sensitivity analysis is included.

3.1 Physics-based models of the cardiovascular system

Computational models of the arterial network and coronary circulation are designed to predict pressure and flow in the arteries. Important steps in the model design include specifying the properties of the fluid (blood) alongside the equations that govern the flow of the blood.

Blood mainly consists of blood plasma and blood cells (red blood cells, white blood cells and platelets). While plasma shows a linear relation between shear rate and shear stress, and is thus considered a Newtonian fluid, it is well known that (whole) blood behaves as a non-Newtonian fluid. At low shear rates (below 50 s^{-1}) red blood cells group together and form large cellular aggregates (rouleaux) which causes a disproportionate increase in the viscosity [37]. How-

ever at higher shear rates whole blood shows a near linear relationship between shear rate and shear stress, and may thus be approximated as Newtonian [38]. The compressibility of blood is low, and the shear rates of the large conduit- and normal coronary-arteries are typically greater than $500\,s^{-1}$ near the vessel wall. Blood is thus commonly modeled as an incompressible Newtonian fluid [23, 24, 39]. These assumptions were also adopted in this thesis.

Computational models of the cardiovascular system that are based on physical descriptions that govern the flow of blood are commonly separated into three-dimensional (3D), one-dimensional (1D) and lumped models (0D).

3.1.1 3D models

For an incompressible Newtonian fluid, the Navier-Stokes equations written in compact form, are:

$$\frac{\partial \mathbf{u}}{\partial t} + \mathbf{u} \cdot \nabla \mathbf{u} = -\frac{1}{\rho}\nabla p + \nu \nabla^2 \mathbf{u}\,, \tag{3.1}$$

where ρ is the blood density and ν is the kinematic viscosity, given by $\nu = \mu/\rho$, with blood viscosity μ. Furthermore, t is time, p is the pressure and $\mathbf{u}$ is a vector of velocity components (u_x, u_y and u_z in Cartesian coordinates). Eq. (3.1) represents three equations for the balance of momentum in the x, y and z direction (Cartesian coordinates). The left hand side represents acceleration, transient and spatial respectively. The first term on the right hand side represents pressure forces, and the second term represents viscous forces. Further conservation of mass is given by:

$$\nabla \cdot \mathbf{u} = 0\,. \tag{3.2}$$

The Navier-Stokes equations together with the conservation of mass govern the behavior of blood flow velocity and pressure in arbitrary domains.

3.1.2 1D models

Most arteries have a nearly cylindrical cross-section, and the flow is primarily directed along the long axis of the artery. By the assumption that flow is unidirectional (axial velocity components dominate over radial components) the 1D equations for blood flow may be derived:

$$\frac{\partial A}{\partial P}\frac{\partial P}{\partial t} + \frac{\partial Q}{\partial x} = 0\,, \tag{3.3a}$$

$$\frac{\partial Q}{\partial t} + \frac{\partial Q^2/A}{\partial x} = -\frac{A}{\rho}\frac{\partial P}{\partial x} + \frac{f}{\rho}\,, \tag{3.3b}$$

In the (above) 1D formulation the problem is stated for the integrated variables P and Q which represent the cross-sectional averaged pressure and volumetric flow respectively. Furthermore, f is the frictional term, and is given by $-2\left(\zeta+2\right)\mu\pi U$, where A is the cross-sectional area and U is the cross-sectional averaged velocity in the axial direction. The above formulation assumes a constant velocity profile shape given by:

$$u(x,\xi,t) = U(x,t)\frac{\zeta+2}{\zeta}\left[1-\left(\frac{\xi}{r}\right)^{\zeta}\right]\,, \tag{3.4}$$

where $r(x,t)$ is the lumen radius, ξ is the radial coordinate and ζ is a velocity profile shape-factor. Eq. (3.3a) and (3.3b) represent the conservation of mass and momentum in elastic arteries. In order to close the system, a relation between the pressure and area is needed. With the assumptions of thin-walled elastic vessels, a pressure-area relation can be derived from Laplace's Law:

$$P = P_{\mathrm{d}} + \frac{\beta}{A_{\mathrm{d}}}\left(\sqrt{A}-\sqrt{A_{\mathrm{d}}}\right)\,, \tag{3.5}$$

where P_{d} and A_{d} are reference values for the pressure and area, and β is a material parameter related to the stiffness of the artery. One-dimensional models of blood flow have been used extensively to study the propagation of pressure and flow waves throughout the arterial tree [8, 10, 39], and more recently, in the venous circulation [9].

With assumptions of steady flow and a fixed cross-sectional area, the momentum-balance given by Eq. (3.3b) simplifies to an algebraic relation:

$$\Delta P_{\mathrm{1D}} = a\cdot Q + b\cdot Q^2\,, \tag{3.6}$$

where

$$a = \int_0^l \frac{2\left(\zeta+2\right)\pi\mu}{A\left(x\right)^2}\mathrm{d}x\,, \quad b = \frac{\rho}{2}\left(\frac{1}{A_{\mathrm{out}}^2}-\frac{1}{A_{\mathrm{in}}^2}\right)\,. \tag{3.7}$$

Here, ΔP represents the pressure loss from the inlet to the outlet of a 1D-arterial segment with length l. Further, $A(x)$ is the the spatially varying cross-sectional

area, and A_{in} and A_{out} are the cross-sectional areas at the inlet and outlet respectively. The first term in Eq. (3.6) represents viscous related pressure losses, while the second (quadratic) term is related to spatial acceleration of the velocity. The quadratic term given by Eq. (3.7) represents an idealized case, for which pressure (related to this term) is fully recovered if the inlet and outlet of the segment has equal areas. As a consequence it is not adequate to describe pressure losses across stenoses. However, experimental studies indicate that the pressure loss across a stenosis may be adequately described by a second order polynomial, by modifying the coefficients, a and b [40].

3.1.3 0D models

In zero-dimensional models, the entire or part of the arterial circulation is lumped into a few properties that explain the gross behavior of the system. For instance, the pressure at the aorta is about $100\,\text{mmHg}$, while the pressure on the venous side is approximately $5\,\text{mmHg}$. This drop in pressure is primarily caused by the frictional forces that impose the flow in the millions of arteries that make up the arterial network. As such, a lumped model that describes the relation between volumetric flow and pressure in the arterial tree is given by Ohm's law:

$$Q = \frac{P - P_{\text{out}}}{R}\,, \tag{3.8}$$

where Q and P are the aortic flow and pressure respectively, P_{out} is the venous pressure and R is the systemic resistance.

According to Eq. (3.8), the pressure and flow is in phase. As illustrated by the aortic flow and pressure in Figure 2.2 however, this is not the case. The peak in pressure occur slightly after the peak in flow, and importantly, flow is non-zero only in the period when the aortic valve is open. The pressure on the other hand slowly decays after the closure of the aortic valve. One of the first attempts to model the most important characteristics of pressure and flow waveforms was made by Otto Frank when he introduced the classical Windkessel model in 1899 [41]. He added a capacitor in parallel to a resistance element, and analogous to the way a capacitor can store electrical energy, the capacitor represents the compliance of the aorta and large arteries, and their ability to store part of the ejected blood volume in systole. The stored volume is released as flow to the smaller arteries and capillaries throughout diastole.

A noteworthy extension to the classical Windkessel model was presented in [42] where a resistance element representing the characteristic impedance of the aorta was added. Furthermore, many variations and extensions have been proposed [43], also those with particular emphasis on the coronary circulation as in [44]. The

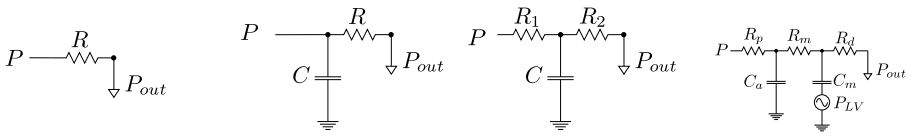

Figure 3.1: Overview of common 0D models of the cardiovascular system. From left: a resistance model, the classical Windkessel model, the three element Windkessel model, and a coronary model.

resistance model, the classical Windkessel model, the three element Windkessel model, and a coronary model is shown schematically in Figure 3.1.

3.1.4 Boundary conditions

3D models of the arterial system are commonly used to study detailed flow phenomena, and 1D theory is commonly used to study wave propagation phenomena in distributed models including large networks of arteries. However, the governing equations given by Eq. (3.1) and Eq. (3.3) are only valid in the computational domain, and appropriate boundary conditions have to be set in order to solve the problems. In this regard, three different types of boundary conditions typically exist in such models: inlet boundary conditions, outlet boundary conditions, and interface boundary condition. For the inlet boundary condition, measurements often allow one to prescribe either flow or pressure, while the no-slip condition is normally applied at the interface between the fluid and the vessel walls. Outlet boundary conditions, however are often more tricky.

In patient specific models of the arterial system or coronary circulation the computational domain is often extracted from clinical imaging for which only a subset of arteries are visible. Moreover, given the near endless number of small arteries and capillaries in the human body, the arterial network has to be truncated at a certain level. Since reliable measurements of flow or pressure at all terminal sites are practically impossible to obtain, outflow boundary conditions are commonly set through morphological relations, or simpler models representing the peripheral circulation. Indeed the above-mentioned family of 0D models have been the preferred choice for describing the peripheral circulation.

3.2 Machine learning

The first work considered as artificial intelligence and machine learning was published in 1943 by McCulloh and Pitts [45]. Inspired by the human nervous system they presented the theory of an artificial neuron and proved that any computable function could be represented by some network of connected neurons. Later, in

1950 Alan Turing published the seminal paper "Computing Machinery and Intelligence", where visions for the future of artificial intelligence and machine learning was put forth [46]. He amongst other asks "*Instead of trying to produce a programme to simulate the adult mind, why not rather try to produce one which simulates the child's?*" In order to evolve to a state comparable to an adult brain, it would have to learn.

In simple words, artificial intelligence is a science which occupation is to build intelligent programs and machines that can creatively solve problems. Machine learning is a sub-category of artificial intelligence, and refers to the methods and algorithms that provide the ability to learn from data or improve from experience, without being specifically programmed to accomplish a specific task.

Machine learning is commonly separated into different types of learning. In supervised learning, the algorithms are designed to find relationships between a set of input and output pairs. In unsupervised learning, the algorithms are designed to find relationships in inputs, without knowing a desired output (*e.g.* clustering of data). In reinforcement learning the desired output is not specifically given, but the algorithms learn beneficial behavior based on stimuli (*i.e.* punishment or reward).

This section is not intended to give an introduction to artificial intelligence and machine learning, but rather give insights into the landscape of artificial intelligence and the position of the specific algorithms used in this thesis. Below follows a bit more detailed description of artificial neural networks, which were applied in supervised learning in paper 4. For a more thorough introduction the reader is referred to [47, 48], which are the main sources for this section. Moreover, parts of the content of this chapter is published as Jupyter notebooks at the authors private GitHub repo [49].

3.2.1 Artificial Neural Networks

The artificial neuron proposed by McCulloh and Pitts [45] was characterized by an "on" or "off" behavior and is commonly referred to as a perceptron. Neural networks made up of perceptrons limits the possibility to train networks efficiently, as we will see later. Perceptrons do however conveniently introduce the basic concepts of artificial neurons and neural networks.

Figure 3.2 shows a perceptron with two input signals x_1 and x_2, both of which can have a zero signal intensity or a signal intensity equal to one. The signals are related to weights ω_1 and ω_2, which indicate the importance of the signals. Further, θ is the activation threshold of the neuron, and y is the output which can be either one or zero according to:

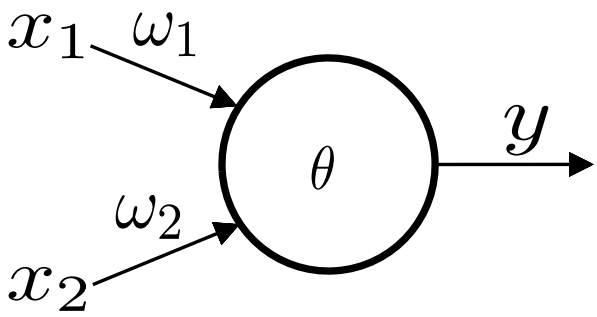

Figure 3.2: A perceptron neuron with two input signals, $x_1 \in \{0, 1\}$ and $x_2 \in \{0, 1\}$ with corresponding weights ω_1 and ω_2. The neuron has an activation threshold θ and an output $y \in \{0, 1\}$

$$y = \begin{cases} 1 & \text{if } \sum_i \omega_i x_i \geq \theta \,, \\ 0 & \text{if } \sum_i \omega_i x_i < \theta \,. \end{cases} \tag{3.9}$$

Hence, if the sum of the signal intensities multiplied by the weights of the signals exceeds the activation threshold, the neuron is activated and "fires".

This simple one-neuron two-input network represent the basic concepts of artificial neural networks. Moreover, this network can also represent an "and"-function (*e.g.* $\omega_1 = \omega_2 = 1 \,, \theta = 1.5$) and an "or"-function (*e.g.* $\omega_1 = \omega_2 = 1.5 \,, \theta = 1$). The reader may verify this.

Normally, the activation threshold is represented as a bias $b = -\theta$, such that Eq. (3.9) is rewritten:

$$y = \begin{cases} 1 & \text{if } \sum_i \omega_i x_i + b \geq 0 \,, \\ 0 & \text{if } \sum_i \omega_i x_i + b < 0 \,. \end{cases} \tag{3.10}$$

This convention is of little conceptual importance, but it has some mathematical benefits, and will thus be used from here on.

Fully connected feed forward neural networks

The previous example shows a simple construction of a neural network. The power of neural networks, however, is greatly improved when neurons are connected in layers. This section looks at fully connected feed forward neural networks, with multiple layers, and shows that they can be represented in terms of a series of matrix multiplications. In this context:

- **feed forward** information is propagated in one direction only (from input to

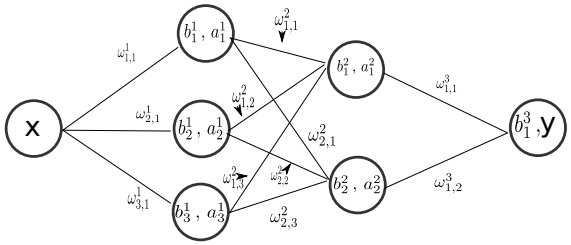

Figure 3.3: A fully connected feed forward neural network with one input and output neuron and two hidden layers with three and two neurons respectively.

output)

- **fully connected** means that all neurons in a layer l is connected to all neurons in the previous $(l-1)$ and next $(l+1)$ layer.

Also of note is that there is no direct passage of information other than via neighbouring layers in fully connected feed forwar neural networks.

Figure 3.3 shows a neural network with one input neuron, two hidden layers with three and two neurons respectively, and one output layer with one neuron. The figure depicts the input and output (activations), all weights connecting the neurons, biases and activations of each neuron. The following naming convention is used:

- $\omega_{j,k}^l$ is the **weight** from the k^{th} neuron in the $(l-1^{\text{th}})$ layer to the j^{th} neuron in the l^{th} layer
- b_j^l is the **bias** of the j^{th} neuron in the l^{th} layer
- a_j^l is the **activation** of the j^{th} neuron in the l^{th} layer

With this naming convention the activation of neuron a_j^l is given by:

$$a_j^l = \sigma\left(\sum_k \omega_{j,k}^l a_k^{l-1} + b_j^l\right) , \tag{3.11}$$

where σ is an activation function. In the case of using perceptron neurons the output of a_j^l would be:

$$\text{output} = \begin{cases} 1 & \text{if } \left(\sum_k \omega_{j,k}^l a_k^{l-1} + b_j^l\right) \geq 0 \\ 0 & \text{if } \left(\sum_k \omega_{j,k}^l a_k^{l-1} + b_j^l\right) < 0 \end{cases} , \tag{3.12}$$

but we note that σ can be any function. Further, the activation of a layer l, a^l can be represented in a **vectorized form**:

$$a^l = \sigma\left(\omega^l a^{l-1} + b^l\right) . \tag{3.13}$$

With this, the activation of the different layers in the example above can be computed as:

$$a^1 = \sigma\left(\begin{bmatrix}\omega_{11}^1\\ \omega_{21}^1\\ \omega_{31}^1\end{bmatrix} \cdot \begin{bmatrix}x\end{bmatrix} + \begin{bmatrix}b_1^1\\ b_2^1\\ b_3^1\end{bmatrix}\right) , \tag{3.14}$$

$$a^2 = \sigma\left(\begin{bmatrix}\omega_{11}^2 & \omega_{12}^2 & \omega_{13}^2\\ \omega_{21}^2 & \omega_{22}^2 & \omega_{23}^2\end{bmatrix} \cdot \begin{bmatrix}a_1^1\\ a_2^1\\ a_3^1\end{bmatrix} + \begin{bmatrix}b_1^2\\ b_2^2\end{bmatrix}\right) , \tag{3.15}$$

$$y = \sigma\left(\begin{bmatrix}\omega_{13}^3 & \omega_{23}^3\end{bmatrix} \cdot \begin{bmatrix}a_1^2\\ a_2^2\end{bmatrix} + \begin{bmatrix}b_1^3\end{bmatrix}\right) . \tag{3.16}$$

Training of neural networks Neural networks are universal function approximators, meaning that they can in theory describe any functional relation from input to output, provided the correct network architecture. In practice, however, this is seldom achieved, since application of neural networks (other than for education purposes) involves real data, from measurements and observations that come with a level of noise. Hence the problem involves finding the weights and biases of the network, such that the output y predicts the true (labeled) quantity $\hat{y}$ as good as possible. This task may be formalized by minimization of a cost function, C, for example the mean squared error between the predicted and true quantities:

$$C = \frac{1}{N}\sum_{i=1}^{N}\left(y_i - \hat{y}_i\right)^2 , \tag{3.17}$$

where N is the number of observations. A reasonable strategy to achieve this, is to define small changes in the weights, $\Delta\omega$, and biases, Δb, that ensures a small negative change in the cost function, $\Delta C < 0$. It turns out that that this is achieved by choosing:

$$\Delta\omega_i = -\lambda\frac{\partial C}{\partial \omega_i} , \tag{3.18a}$$

$$\Delta b_i = -\lambda\frac{\partial C}{\partial b_i} , \tag{3.18b}$$

provided that $\Delta\omega$ and Δb are sufficiently small. The latter may be controlled by adjusting the learning rate, λ. Eq. (3.18) is known as the gradient descent update

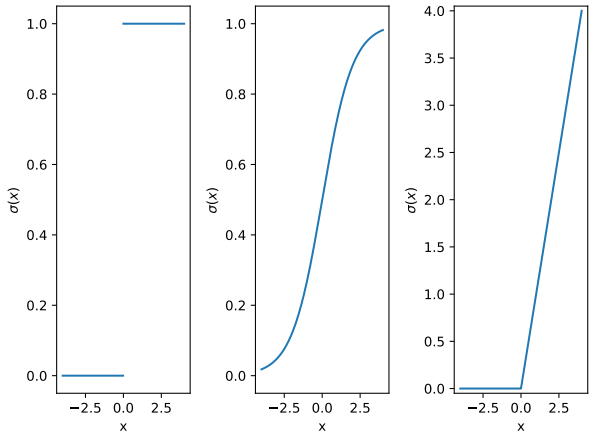

Figure 3.4: The original perceptron activation function (left), the sigmoid (middle) and the rectified linear unit, ReLU (right).

rule, and involves the calculation of the partial derivative of the cost function with respect to (all!) the weights and biases in the network. This also reveals the limitation of the perceptron neuron ($\sigma\,(x)$), since its derivative is zero everywhere except at $x = 0$, where its derivative is not defined. The gradient descent algorithm (and its variations) require continuous differentiable activation functions. The perceptron along with common activation functions, the Sigmoid and the rectified linear unit (ReLU) are shown in Figure 3.4.

The gradient descent algorithm provides a method to iteratively update weights and biases such that the network output, y, approaches the true quantity, y (*i.e.* it provides a method for training the neural network). However, the algorithm requires the calculation of partial derivatives with respect to all the weights and biases in the network. This process can be very time consuming in large networks if performed weight by weight or layer by layer. Instead, this is achieved by application of the backpropagation algorithm, where errors are propagated from the output layer, throughout the network, and all the way to the first layer of the network. These errors are used to estimate the partial derivatives of the weights and biases of a layer, and calculations of errors and gradients are reused when estimating the gradients of the next layer.

Generalization of neural networks Neural networks are extremely powerful, given their universal ability to find relations from input to output. However, this ability is considered dangerous because of the possibility to find noisy relationships in the training data that does not generalize to unseen data (*i.e.* input-output relations

that were not used during training). This is known as over-fitting and can typically occur if complex networks are trained on sparse data.

Overfitting can be avoided by reducing the complexity of the network (fewer layers, and neurons in each layer), however, this may lead to under-fitting, which is characterized by a network that is unable to find adequate relationships from input to output. Other methods that can improve generalization include the application of a validation set and regularization:

Validation set A validation set is a certain fraction of the training set that is not used to estimate gradients and update weights and biases, but is used to test the network after each epoch. If the loss on the actual training data continues to go towards zero but the validation loss increases (a sign of over-fitting), the training is stopped (**early stopping**).

Regularization Large weights are associated with high sensitivity to certain signals, and is often indicative of over-fitting. Regularization of neural networks is performed by adding a term to the cost function that penalizes large weights, such as the L_1 or L_2 norm of all the weights of the network.

Even with the application of these and other procedures, over-fitting may occur. Hence, it is considered mandatory to always leave part of the data (a test set) aside, which is only used to test the final network.

3.3 Uncertainty Quantification and Sensitivity Analysis

The patient-specific modeling paradigm attempts to enhance clinically measured data by predicting unmeasured physiological states through model simulations based on available data and validated modeling principles. As clinical data always has some uncertainty and unmeasured parameters may be known to vary significantly, we must characterize the uncertainty of model predictions in addition to verifying that a computational model solves the idealized mathematical model to an adequate level of accuracy. Towards this end we employ UQ&SA to assess the uncertainty present in patient-specific model predictions as well as to identify inputs that prevent greater certainty in model predictions.

First we briefly summarize notation. UQ&SA typically analyzes a model prediction y as a function M of inputs $\mathbf{z}$, $y = M(\mathbf{z})$, where lower case letters denote the relationship of a deterministic case where $\mathbf{z}$ is known. Uncertain inputs are denoted $\mathbf{Z}$ as they are random variables and thus $Y = M(\mathbf{Z})$ is also a random variable.

We employ the nonintrusive UQ&SA methods of Monte Carlo and Polynomial

chaos to characterize the distribution of Y given the distribution of $\mathbf{Z}$. This is achieved by evaluating M at many samples drawn from the distribution of $\mathbf{Z}$, i.e. $y = M(\mathbf{z})$ at each sample point in $\left\{\mathbf{z}^{(s)}\right\}_{s=1}^{N_\mathrm{s}}$. Eck et al. [50] present several methods and concepts of UQ&SA within the context of cardiovascular modeling, and we refer the reader to this work for more details regarding the methods of UQ&SA used here.

The uncertainty of Y is fundamentally due to the uncertainty of $\mathbf{Z}$ propagated through the model M. Thus it is critical to employ a distribution of $\mathbf{Z}$ that reflects the conditions the UQ&SA is intended to analyze. To assess performance of a patient specific model the input distribution must reflect the actual uncertainties present in clinical procedures and population variation. However, UQ&SA may also be employed to analyze a model's range of behavior and to identify parameters relevant for estimation from measured values of y. In this case the distribution of $\mathbf{Z}$ should reflect the range of plausible values for the inputs. Typically, only a range of values is considered and no prior knowledge is available to prioritize certain regions, thus a uniform distribution is appropriate to investigate the model's dependence on the parameters.

Once the approximate distribution of Y is available from the UQ&SA procedure various measures of the uncertainty of Y are available such as the expected value, $\mathbb{E}[Y]$ and variance $\mathbb{V}[Y]$. These quantities are of primary interest when assessing model performance, however, SA augments this by assessing the portion of uncertainty due to particular inputs, allowing prioritization of efforts to reduce uncertainty. In this context, Sobol sensitivity indices, first-order (S_i) and total ($S_{\mathrm{T},i}$), are widely employed [51], and defined as

$$S_i = \frac{\mathbb{V}\left[\mathbb{E}\left[Y \mid Z_i\right]\right]}{\mathbb{V}\left[Y\right]}, \tag{3.19a}$$

$$S_{\mathrm{T},i} = 1 - \frac{\mathbb{V}\left[\mathbb{E}\left[Y \mid \mathbf{Z}_{\neg i}\right]\right]}{\mathbb{V}\left[Y\right]}, \tag{3.19b}$$

where the vector, $\mathbf{Z}_{\neg i}$, contains all elements of $\mathbf{Z}$ except Z_i. These indices partition the total $\mathbb{V}[Y]$ into portions attributable to specific combinations of inputs. The first order indices S_i quantify the variance due to Z_i alone, i.e. independent of the values of the other inputs. The total sensitivity index, $S_{\mathrm{T},i}$, includes effects caused by the interaction with other parameters and represents the reduction in variance expected to be achieved by fixing Z_i at a particular value.

Larger values of S_i suggest that Z_i strongly affects Y and thus may be a prime target for improved measurement or optimization in the context of parameter esti-

mation. In the case where $S_{\mathrm{T},i}$ and thus also S_i are small, Z_i has little influence on Y and should not be prioritized for improved measurement and may not be estimated accurately in an inverse problem context.

Chapter 4

Summary of appended papers

Paper 1 (Chapter 6)

Optimization of topological complexity for one-dimensional arterial blood flow models *F.E. Fossan, J. Mariscal-Harana, J. Alastruey, L.R. Hellevik*
Published in *Journal of the Royal Society Interface*, 2018.

In this paper we present a framework to optimize/reduce the number of arterial segments included in one-dimensional arterial blood flow models, while preserving key features of flow and pressure waveforms. The removed 1D segments were represented by 0D Windkessel models. The framework was tested on a patient specific model of the coronary circulation and on a model containing 96 of the largest arteries, including the aorta and its main segments, the upper and lower limbs in addition to the main cerebral arteries. We showed that the aortic pressure waveform could be modeled by a network that includes a minimal description of the upper and lower limbs and no cerebral network, without significant effect on pressure waveforms. Further, we found that discrepancies in carotid and middle cerebral artery flow waveforms that are introduced by describing the arterial system in a minimalistic manner are small compared with errors related to uncertainties in blood flow measurements obtained by ultrasound.

Paper 2 (Chapter 7)

Uncertainty Quantification and Sensitivity Analysis for Computational FFR Estimation in Stable Coronary Artery Disease *F.E. Fossan, J. Sturdy, L.O. Müller, A. Strand, A. Bråten, A. Jørgensen, R. Wiseth, L.R. Hellevik*

Published in *Cardiovascular Engineering and Technology*, 2018.

In this paper we present a novel reduced-order model for prediction of FFR in stable coronary artery disease. The predictions were compared against invasively measured FFR and against predictions obtained by a more comprehensive 3D model. An extensive sensitivity analysis on the parameters related to the construction of the reduced-order model was conducted and used to decide parameters for optimization. Further, methods of uncertainty quantification and sensitivity analysis was applied, which demonstrated that the factors that have the biggest influence on predicted FFR are related to the uncertain effects of pharmacologically induced vasodilation and the uncertainty in segmented geometry. The UQ and SA was performed individually for each patient, where it was shown that the uncertainty and also the ranking of the most influential parameters changes with the absolute value of FFR.

Paper 3 (Chapter 8) Impact of baseline coronary flow and its distribution on fractional flow reserve prediction *L.O. Müller, F.E. Fossan, A. Bråten, A. Jørgensen, R. Wiseth, L.R. Hellevik*
Published in *International Journal for Numerical Methods in Biomedical Engineering*, 2019.

In this paper we evaluated the impact of assumptions necessary to assign outlet boundary conditions in non-invasive FFR-prediction. Specifically, we implemented several methods available in the literature to estimate and distribute baseline coronary flow. We found that the estimation and distribution of baseline coronary flow had a significant impact on diagnostic performance. However, none of the proposed methods resulted in a significant improvement of prediction error standard deviation. Finally, we showed that intrinsic uncertainties related to stenosis geometry and the effect of hyperemic inducing drugs have to be addressed in order to improve FFR prediction accuracy.

Paper 4 (Chapter 9) Machine learning augmented reduced order model for FFR-prediction *F.E. Fossan, L.O. Müller, J. Sturdy, A. Bråten, A. Jørgensen, R. Wiseth, L.R. Hellevik*
Submitted to *Computet Methods in Applied Mechanics and Engineering*, 2020.

In this paper we analyzed the effect of incorporating prior physics-based knowledge in the learning process for prediction of pressure and FFR in coronary arteries. Fully connected feed forward neural networks were trained to predict pressure

losses obtained by solution of the 3D incompressible Navier-Stokes equations in segmented coronary arteries. The prior information was included by training NNs to 1) predict the discrepancy between the reduced order model and 3D pressure loss rather than pressure directly and 2) incorporated in the learning process by including the ROM pressure loss as an input-feature. The physics informed NNs were compared with a corresponding purely data-driven NN for three different training sets with increasing amount of data. Both approaches for incorporation of prior physics-based knowledge significantly improved prediction of pressure losses relative to the purely data-driven approach, especially for lower amounts of training data.

4.1 Statement of authorship

In Chapter 6 Fredrik E. Fossan designed the study, implemented all methods, performed all simulations, pre- and post-processing of data and drafted the manuscript. In Chapter 7 Fredrik E. Fossan contributed to the design of the study, implemented methods, and performed simulations, pre- and post-processing of data and drafted the manuscript. In Chapter 8 Fredrik E. Fossan contributed to the design of the study, performed simulations, pre- and post-processing of data and contributed in the writing of the manuscript. In Chapter 9 Fredrik E. Fossan contributed to the design of the study, performed simulations, pre- and post-processing of data and drafted the manuscript. In all papers coauthors contributed to the design of the studies, through revisions, in data-collection and in invaluable discussions of results, as well as focusing and inspiring the research.

Chapter 5

Conclusions and directions for further work

5.1 Main conclusions

In this thesis we have focused on the development of reduced-order models for blood flow in the arterial system and for the diagnosis of coronary artery disease.

We found that to capture important features of the aortic pressure waveform, such as timing and shape of reflected waves, pressure augmentation and pulse pressure, a model with all aortic segments, but close to minimal description of the head and lower and upper limb arteries is sufficient. To capture the gross features of the middle cerebral artery waveforms we found that the inclusion of an intact representation of aortic segments was more important than description of nearby vasculature. Further, errors in the middle cerebral and carotid flow waveforms that are introduced by describing the arterial system in a minimalistic manner are small compared with errors related to uncertainties in blood flow measurements obtained by ultrasound.

Furthermore, we have developed a novel reduced-order model for prediction of Fractional Flow Reserve which was validated against a corresponding, more complex 3D model. We demonstrated how global sensitivity analysis can be used as a part of model validation and assist in the process of parameter estimation. Moreover, the accuracy of the reduced-order model was augmented by application of neural networks for the prediction of pressure loss in coronary segments. We found that the prediction accuracy of the neural networks and the generalization of

the predictions were significantly improved by incorporating prior physics in the learning process. Furthermore, the incorporation of the physics-informed neural networks into a coronary network model led to FFR predictions with an error standard deviation of 0.02 with respect to the 3D model, which is comparable with the standard deviation of repeated FFR measurements. With model errors reduced to this level, uncertainties in input data dominate the total error/uncertainty, making the error introduced by the model reduction negligible.

The simplifications introduced by the model reduction reduced the computational time for FFR prediction, from the order of hours/days (3D model) to fractions of a second. The reduced computational costs enabled exploration of effects of boundary conditions and application of uncertainty quantification and sensitivity analysis.

We characterized the diagnostic accuracy of the reduced-order model for classification of ischemia, with invasive FFR used as gold standard. The model obtained an accurcay of 89 %, sensitivity of 79 % and specificity of 93 % in an unblided study of a population of 63 patients. Moreover, we found that the estimation and distribution of baseline coronary flow had a significant impact on diagnostic performance. Several methods available in the literature were implemented. We observed that none of the proposed methods for estimation and distribution of baseline flow resulted in a significant improvement of prediction error standard deviation. The latter revealed two things: 1) the implemented methods involve measurements and assumptions that result in significant uncertainty and 2) even imposition of the correct baseline flow would still lead to high uncertainty in predicted FFR, due to uncertainties related to stenosis geometry and the effect of hyperemic inducing drugs. As such, uncertainties related to stenosis geometry and the effect of hyperemic inducing drugs have to be addressed in order to improve FFR prediction accuracy.

5.2 Future work

This thesis was conducted as part of a project "Model based, noninvasive diagnosis of coronary artery disease with 3D ultrasound and CT". The presented results for diagnostic accuracy were based on a study where the model-developers were not blinded to the invasively measured FFR. Hence, a blinded study is needed to test the robustness of these results. Moreover, part of the project has involved the development of (trans-thoracic) ultrasound technology for direct non-invasive measurement of flow in the coronary arteries. This technology has been developed alongside the development of the non-invasive FFR-pipeline. Future studies will assess if the incorporation of measurements (*i.e.* to improve definition of boundary conditions) can improve prediction accuracy of FFR.

Findings in paper 2 and paper 3 show that, even with perfect knowledge of the flow in baseline conditions (rest), there would still be substantial residual uncertainty related to the effect of stenosis geometry and the effect of hyperemic inducing drugs. Thus, efforts should be focused towards improving modeling of the vasodilating effects of drugs, and optimizing the process of geometry segmentation. One approach to improve the former would be to perform ultrasound measurements also during hyperemia. Unfortunately, this would require the use of drugs. However, the study by Zreik et al. indicate that CCTA images of the myocardium provide information about the perfusion of the coronaries in hyperemia [30]. They used machine learning to determine from CCTA-imaged myocardium texture whether a stenosis was functionally significant or not, as classified in terms of FFR. This indicates that abnormal myocardial tissue (classified as such by an unsupervised machine learning algorithm) provide useful information. A similar approach might supply information that could be used to improve modeling aspects of FFR, such as the distribution of flow and the effect of adenosine.

Most clinical CT-scanners offer spatial resolution of approximately 0.5 mm [52]. This limit in spatial resolution introduces a layer of uncertainty in the modelling pipeline since features smaller than this are not resolved. However, studies indicate that the vessel enhancement (*i.e.* the approximate intensity of blood in Houndsfield units) and heart rate during CCTA-acquisition effect the diagnostic performance of FFR predictions [53]. This suggests that optimization of CT-protocols could improve prediction accuracy. Moreover, technological advancement has led to greatly improved CCTA-image quality during the past decades. This is likely to continue in the years to come, and will thus help to reduce uncertainty related to the definition of vessels' geometry [52].

The improvements in CCTA quality mean that it is now possible to extract more information related to the atheresclorotic disease. In particular, it is possible to extract information related to the composition of the plaque [54]. It is well known that certain plaque features, such as positive remodeling (the plaque expands outwards) and low attenuation (indicative of lipid rich plaque) are associated with acute coronary syndrome [55]. Moreover, recent studies also suggest a relation between such plaque characteristics with ischemia and FFR [56]. The authors of [56] propose that the presence of large necrotic cores and low attenuation plaque may be associated with the inability of the vessel to dilate. An alternative hypothesis is one that relates the plaque characteristics to the health of the downstream vasculature. In any case, further studies are needed to improve the understanding between plaque characteristics, anatomical obstruction and hemodynamcis. Advancements could lead to improved modeling of FFR, and more importantly, contribute to the debate on what should guide treatment and intervention.

Bibliography

[1] J. R. Levick, An Introduction to Cardiovascular Physiology., Hodder Arnold, UK, 2010.

[2] W. Huberts, S. G. H. Heinen, N. Zonnebeld, et al., What is needed to make cardiovascular models suitable for clinical decision support? A viewpoint paper, Journal of Computational Science 24 (2018) 68–84. doi:10.1016/j.jocs.2017.07.006.
URL http://www.sciencedirect.com/science/article/pii/S1877750317307901

[3] W. H. Organization, Top 10 causes of death (2018).
URL http://www.who.int/news-room/fact-sheets/detail/the-top-10-causes-of-death

[4] W. H. Organization, Disease burden and mortality estimates (2016).
URL https://www.who.int/healthinfo/global_burden_disease/estimates/en/

[5] J. Leal, R. Luengo-Fernández, A. Gray, S. Petersen, M. Rayner, Economic burden of cardiovascular diseases in the enlarged European Union, European Heart Journal 27 (13) (2006) 1610–1619, publisher: Oxford Academic. doi:10.1093/eurheartj/ehi733.
URL https://academic.oup.com/eurheartj/article/27/13/1610/636758

[6] M. F. O'Rourke, Pressure and flow waves in systemic arteries and the anatomical design of the arterial system., Journal of Applied Physiology 23 (2) (1967) 139–149.
URL http://jap.physiology.org/content/23/2/139

[7] M. S. Olufsen, A. Nadim, L. A. Lipsitz, Dynamics of cerebral blood flow regulation explained using a lumped parameter model, American Journal of Physiology-Regulatory, Integrative and Comparative Physiology 282 (2) (2002) R611–R622, publisher: American Physiological Society. doi:10.1152/ajpregu.00285.2001.
URL https://journals.physiology.org/doi/full/10.1152/ajpregu.00285.2001

[8] P. Reymond, F. Merenda, F. Perren, D. Rüfenacht, N. Stergiopulos, Validation of a one-dimensional model of the systemic arterial tree, American Journal of Physiology - Heart and Circulatory Physiology 297 (1) (2009) H208–H222. doi:10.1152/ajpheart.00037.2009.
URL http://ajpheart.physiology.org/content/297/1/H208

[9] L. O. Müller, E. F. Toro, A global multiscale mathematical model for the human circulation with emphasis on the venous system, International Journal for Numerical Methods in Biomedical Engineering 30 (7) (2014) 681–725. doi:10.1002/cnm.2622.

[10] P. J. Blanco, S. M. Watanabe, M. A. R. F. Passos, P. A. Lemos, R. A. Feijóo, An anatomically detailed arterial network model for one-dimensional computational hemodynamics, IEEE Transactions on Biomedical Engineering 62 (2) (2015) 736–753. doi:10.1109/TBME.2014.2364522.

[11] A. Quarteroni, T. Lassila, S. Rossi, R. Ruiz-Baier, Integrated Heart—Coupling multiscale and multiphysics models for the simulation of the cardiac function, Computer Methods in Applied Mechanics and Engineering 314 (2017) 345–407. doi:10.1016/j.cma.2016.05.031.
URL http://www.sciencedirect.com/science/article/pii/S0045782516304662

[12] W. Huberts, W. P. Donders, T. Delhaas, F. N. v. d. Vosse, Applicability of the polynomial chaos expansion method for personalization of a cardiovascular pulse wave propagation model, International Journal for Numerical Methods in Biomedical Engineering 30 (12) (2014) 1679–1704, _eprint: https://onlinelibrary.wiley.com/doi/pdf/10.1002/cnm.2695. doi:10.1002/cnm.2695.
URL https://onlinelibrary.wiley.com/doi/abs/10.1002/cnm.2695

[13] M. R. Villarreal, Simplified diagram of the human Circulatory system in anterior view (May 2009).
URL https://commons.wikimedia.org/wiki/User:LadyofHats

[14] Wapcaplet, Diagram of the human heart, created by Wapcaplet in Sodipodi. Cropped by Yaddah to remove white space (this cropping is not the same as Wapcaplet's original crop). (2006-06-02, 07:02).
URL https://no.m.wikipedia.org/wiki/Fil:Diagram_of_the_human_heart_(cropped).svg

[15] M. J. Davies, The pathophysiology of acute coronary syndromes, Heart 83 (3) (2000) 361–366, publisher: BMJ Publishing Group Ltd Section: Education in Heart. doi:10.1136/heart.83.3.361.
URL https://heart.bmj.com/content/83/3/361

[16] S. Glagov, E. Weisenberg, C. K. Zarins, R. Stankunavicius, G. J. Kolettis, Compensatory Enlargement of Human Atherosclerotic Coronary Arteries, New England Journal of Medicine 316 (22) (1987) 1371–1375, publisher: Massachusetts Medical Society _eprint: https://doi.org/10.1056/NEJM198705283162204. doi:10.1056/NEJM198705283162204.
URL https://doi.org/10.1056/NEJM198705283162204

[17] B. Ibanez, S. James, S. Agewall, et al., 2017 ESC Guidelines for the management of acute myocardial infarction in patients presenting with ST-segment elevationThe Task Force for the management of acute myocardial infarction in patients presenting with ST-segment elevation of the European Society of Cardiology (ESC), European Heart Journal 39 (2) (2018) 119–177, publisher: Oxford Academic. doi:10.1093/eurheartj/ehx393.
URL https://academic.oup.com/eurheartj/article/39/2/119/4095042

[18] J. Knuuti, W. Wijns, A. Saraste, et al., 2019 ESC Guidelines for the diagnosis and management of chronic coronary syndromesThe Task Force for the diagnosis and management of chronic coronary syndromes of the European Society of Cardiology (ESC), European Heart Journal 41 (3) (2020) 407–477, publisher: Oxford Academic. doi:10.1093/eurheartj/ehz425.
URL https://academic.oup.com/eurheartj/article/41/3/407/5556137

[19] J. Knuuti, H. Ballo, L. E. Juarez-Orozco, et al., The performance of non-invasive tests to rule-in and rule-out significant coronary artery stenosis in patients with stable angina: a meta-analysis focused on post-test disease probability, European Heart Journal 39 (35) (2018) 3322–3330. doi:10.1093/eurheartj/ehy267.

[20] P. A. Tonino, B. De Bruyne, N. H. Pijls, et al., Fractional Flow Reserve versus Angiography for Guiding Percutaneous Coronary Intervention, New England Journal of Medicine 360 (3) (2009) 213–224, publisher: Massachusetts Medical Society _eprint: https://doi.org/10.1056/NEJMoa0807611. doi:10.1056/NEJMoa0807611.
URL https://doi.org/10.1056/NEJMoa0807611

[21] B. De Bruyne, N. H. Pijls, B. Kalesan, et al., Fractional Flow Reserve–Guided PCI versus Medical Therapy in Stable Coronary Disease, New England Journal of Medicine 367 (11) (2012) 991–1001, publisher: Massachusetts Medical Society _eprint: https://doi.org/10.1056/NEJMoa1205361. doi:10.1056/NEJMoa1205361.
URL https://doi.org/10.1056/NEJMoa1205361

[22] B. Hannawi, W. W. Lam, S. Wang, G. A. Younis, Current use of fractional flow reserve: a nationwide survey, Texas Heart Institute Journal 41 (6) (2014) 579–584. doi:10.14503/THIJ-13-3917.

[23] C. A. Taylor, T. A. Fonte, J. K. Min, Computational Fluid Dynamics Applied to Cardiac Computed Tomography for Noninvasive Quantification of Fractional Flow Reserve, Journal of the American College of Cardiology 61 (22) (2013) 2233–2241. doi:10.1016/j.jacc.2012.11.083.
URL http://linkinghub.elsevier.com/retrieve/pii/S0735109713013041

[24] P. D. Morris, D. Ryan, A. C. Morton, et al., Virtual Fractional Flow Reserve From Coronary Angiography: Modeling the Significance of Coronary Lesions, JACC: Cardiovascular Interventions 6 (2) (2013) 149–157. doi:10.1016/j.jcin.2012.08.024.
URL http://linkinghub.elsevier.com/retrieve/pii/S1936879812011673

[25] S. Tu, E. Barbato, Z. Köszegi, et al., Fractional Flow Reserve Calculation From 3-Dimensional Quantitative Coronary Angiography and TIMI Frame Count, JACC: Cardiovascular Interventions 7 (7) (2014) 768–777. doi:10.1016/j.jcin.2014.03.004.
URL http://linkinghub.elsevier.com/retrieve/pii/S1936879814007912

[26] L. Itu, P. Sharma, V. Mihalef, et al., A patient-specific reduced-order model for coronary circulation (2012) 832–835ISSN: 1945-8452. doi:10.1109/ISBI.2012.6235677.

[27] P. J. Blanco, C. A. Bulant, L. O. Müller, et al., Comparison of 1d and 3d Models for the Estimation of Fractional Flow Reserve, Scientific Reports 8 (1). doi:10.1038/s41598-018-35344-0.
URL http://www.nature.com/articles/s41598-018-35344-0

[28] E. Boileau, S. Pant, C. Roobottom, et al., Estimating the accuracy of a reduced-order model for the calculation of fractional flow reserve (FFR), International Journal for Numerical Methods in Biomedical Engineering 34 (1) (2018) e2908. doi:10.1002/cnm.2908.
URL http://doi.wiley.com/10.1002/cnm.2908

[29] F. E. Fossan, J. Sturdy, L. O. Müller, et al., Uncertainty Quantification and Sensitivity Analysis for Computational FFR Estimation in Stable Coronary Artery Disease, Cardiovascular Engineering and Technologydoi:10.1007/s13239-018-00388-w.
URL http://link.springer.com/10.1007/s13239-018-00388-w

[30] M. Zreik, N. Lessmann, R. W. van Hamersvelt, et al., Deep learning analysis of the myocardium in coronary CT angiography for identification of patients with functionally significant coronary artery stenosis, Medical Image Analysis 44 (2018) 72–85. doi:10.1016/j.media.2017.11.008.

[31] H. Hae, S.-J. Kang, W.-J. Kim, et al., Machine learning assessment of myocardial ischemia using angiography: Development and retrospective validation, PLOS Medicine 15 (11) (2018) e1002693. doi:10.1371/journal.pmed.1002693.
URL https://journals.plos.org/plosmedicine/article?id=10.1371/journal.pmed.1002693

[32] D. Dey, S. Gaur, K. A. Ovrehus, et al., Integrated prediction of lesion-specific ischaemia from quantitative coronary CT angiography using machine learning: a multicentre study, European Radiology 28 (6) (2018) 2655–2664. doi:10.1007/s00330-017-5223-z.
URL https://doi.org/10.1007/s00330-017-5223-z

[33] K. K. Kumamaru, S. Fujimoto, Y. Otsuka, et al., Diagnostic accuracy of 3D deep-learning-based fully automated estimation of patient-level minimum fractional flow reserve from coronary computed tomography angiography, European Heart Journal Cardiovascular Imagingdoi:10.1093/ehjci/jez160.

[34] L. Itu, S. Rapaka, T. Passerini, et al., A machine-learning approach for computation of fractional flow reserve from coronary computed

tomography, Journal of Applied Physiology 121 (1) (2016) 42–52. doi:10.1152/japplphysiol.00752.2015.
URL http://jap.physiology.org/lookup/doi/10.1152/japplphysiol.00752.2015

[35] B. L. Nørgaard, C. J. Terkelsen, O. N. Mathiassen, E. L. Grove, et al., Coronary CT Angiographic and Flow Reserve-Guided Management of Patients With Stable Ischemic Heart Disease, Journal of the American College of Cardiology 72 (18) (2018) 2123–2134. doi:10.1016/j.jacc.2018.07.043.
URL http://www.onlinejacc.org/content/72/18/2123

[36] C. Krittanawong, H. Zhang, Z. Wang, M. Aydar, T. Kitai, Artificial Intelligence in Precision Cardiovascular Medicine, Journal of the American College of Cardiology 69 (21) (2017) 2657–2664. doi:10.1016/j.jacc.2017.03.571.
URL http://www.sciencedirect.com/science/article/pii/S0735109717368456

[37] J. Stuart, M. W. Kenny, Blood rheology., Journal of Clinical Pathology 33 (5) (1980) 417–429, tex.eprint: https://jcp.bmj.com/content/33/5/417.full.pdf tex.publisher: BMJ Publishing Group. doi:10.1136/jcp.33.5.417.
URL https://jcp.bmj.com/content/33/5/417

[38] A. Arzani, Accounting for residence-time in blood rheology models: do we really need non-newtonian blood flow modelling in large arteries?, Journal of The Royal Society Interface 15 (146) (2018) 20180486. arXiv:https://royalsocietypublishing.org/doi/pdf/10.1098/rsif.2018.0486, doi:10.1098/rsif.2018.0486.
URL https://royalsocietypublishing.org/doi/abs/10.1098/rsif.2018.0486

[39] E. Boileau, P. Nithiarasu, P. J. Blanco, et al., A benchmark study of numerical schemes for one-dimensional arterial blood flow modelling, International Journal for Numerical Methods in Biomedical Engineering 31 (10). doi:10.1002/cnm.2732.

[40] B. D. Seeley, D. F. Young, Effect of geometry on pressure losses across models of arterial stenoses, Journal of Biomechanics 9 (7) (1976) 439–448. doi:10.1016/0021-9290(76)90086-5.
URL http://www.sciencedirect.com/science/article/pii/0021929076900865

[41] O. Frank, Die grundform des arteriellen pulses: Mathematische Analyse. Erste Abhandlung, Zeitschrift für Biologie. Offprint, 1899.
URL https://books.google.no/books?id=_Hi_mgEACAAJ

[42] N. Westerhof, Analog studies of human systemic arterial hemodynamics, Dissertations available from ProQuest (1968) 1–242.
URL http://repository.upenn.edu/dissertations/AAI6905676

[43] M. S. Olufsen, Structured tree outflow condition for blood flow in larger systemic arteries, American Journal of Physiology - Heart and Circulatory Physiology 276 (1) (1999) H257–H268.
URL http://ajpheart.physiology.org/content/276/1/H257

[44] S. Mantero, R. Pietrabissa, R. Fumero, The coronary bed and its role in the cardiovascular system: a review and an introductory single-branch model, Journal of Biomedical Engineering 14 (2) (1992) 109–116. doi:10.1016/0141-5425(92)90015-D.
URL http://linkinghub.elsevier.com/retrieve/pii/014154259290015D

[45] W. S. McCulloch, W. Pitts, A logical calculus of the ideas immanent in nervous activity, The bulletin of mathematical biophysics 5 (4) (1943) 115–133. doi:10.1007/BF02478259.
URL https://doi.org/10.1007/BF02478259

[46] A. M. Turing, I.—COMPUTING MACHINERY AND INTELLIGENCE, Mind LIX (236) (1950) 433–460, publisher: Oxford Academic. doi:10.1093/mind/LIX.236.433.
URL https://academic.oup.com/mind/article/LIX/236/433/986238

[47] S. Russel, P. Norvig, Artificial Intelligence a Modern Approach, Pearson, 2016.

[48] M. A. Nielsen, Neural Networks and Deep LearningPublisher: Determination Press.
URL http://neuralnetworksanddeeplearning.com

[49] N. L. Bjørdalsbakke, F. E. Fossan, Machine learning and artificial intelligence for application in cardiovascular biomechanics (2019).
URL https://github.com/Fredf10/CardiovascularML

[50] V. G. Eck, W. P. Donders, J. Sturdy, et al., A Guide to Uncertainty Quantification and Sensitivity Analysis for Cardiovascular Applications, International Journal for Numerical Methods in Biomedical Engineering (2015) n/a–n/aBibtex: eck_guide_2015 bibtex[copyright=Copyright © 2015 John Wiley & Sons, Ltd.]. doi:10.1002/cnm.2755.

[51] A. Saltelli, Global Sensitivity Analysis : The Primer, John Wiley,, Chichester, England, 2008, bibtex: saltelli_global_2008.

[52] P. Ngam, C. Ong, P. Chai, et al., Computed tomography coronary angiography – past, present and future, Singapore Medical Journal 61 (3) (2020) 109–115. doi:10.11622/smedj.2020028.
URL http://www.smj.org.sg/article/computed-tomography-coronary-angiography-%E2%80%93-past-present-and-future

[53] P. P. Xu, J. H. Li, F. Zhou, et al., The influence of image quality on diagnostic performance of a machine learning–based fractional flow reserve derived from coronary CT angiography, European Radiology 30 (5) (2020) 2525–2534. doi:10.1007/s00330-019-06571-4.
URL https://doi.org/10.1007/s00330-019-06571-4

[54] J. Taron, S. Lee, J. Aluru, U. Hoffmann, M. T. Lu, A review of serial coronary computed tomography angiography (CTA) to assess plaque progression and therapeutic effect of anti-atherosclerotic drugs, The International Journal of Cardiovascular Imagingdoi:10.1007/s10554-020-01793-w.
URL https://doi.org/10.1007/s10554-020-01793-w

[55] S. Motoyama, M. Sarai, H. Harigaya, et al., Computed Tomographic Angiography Characteristics of Atherosclerotic Plaques Subsequently Resulting in Acute Coronary Syndrome, Journal of the American College of Cardiology 54 (1) (2009) 49–57. doi:10.1016/j.jacc.2009.02.068.
URL http://www.sciencedirect.com/science/article/pii/S0735109709012182

[56] A. Ahmadi, G. W. Stone, J. Leipsic, et al., Association of Coronary Stenosis and Plaque Morphology With Fractional Flow Reserve and Outcomes, JAMA Cardiology 1 (3) (2016) 350–357, publisher: American Medical Association. doi:10.1001/jamacardio.2016.0263.
URL https://jamanetwork.com/journals/jamacardiology/fullarticle/2515769

Part II

Research Papers

Chapter 6

Optimization of topological complexity for one-dimensional arterial blood flow models

The content of this chapter was published in
Journal of the Royal Society Interface, 2018.

Optimization of topological complexity for one-dimensional arterial blood flow models

F.E. Fossan, J. Mariscal-Harana, J. Alastruey, L.R. Hellevik

INTERFACE

rsif.royalsocietypublishing.org

Research

Cite this article: Fossan FE, Mariscal-Harana J, Alastruey J, Hellevik LR. 2018 Optimization of topological complexity for one-dimensional arterial blood flow models. *J. R. Soc. Interface* **15**: 20180546.
http://dx.doi.org/10.1098/rsif.2018.0546

Received: 17 July 2018
Accepted: 19 November 2018

Subject Category:
Life Sciences–Physics interface

Subject Areas:
biomechanics, biomedical engineering

Keywords:
one-dimensional blood flow, model reduction, model optimization, haemodynamics, pulse wave analysis, computational instantaneous wave-free ratio

Author for correspondence:
Jordi Alastruey
e-mail: jordi.alastruey-arimon@kcl.ac.uk

Electronic supplementary material is available online at https://dx.doi.org/10.6084/m9.figshare.c.4324052.

THE ROYAL SOCIETY PUBLISHING

Optimization of topological complexity for one-dimensional arterial blood flow models

Fredrik E. Fossan[1], Jorge Mariscal-Harana[2], Jordi Alastruey[2,3] and Leif R. Hellevik[1]

[1]Norwegian University of Science and Technology, Trondheim, Norway
[2]Department of Biomedical Engineering, King's College, London, UK
[3]Institute of Personalized Medicine, Sechenov University, Moscow, Russia

FEF, 0000-0003-0006-5165; JA, 0000-0003-3742-5259

As computational models of the cardiovascular system are applied in modern personalized medicine, maximizing certainty of model input becomes crucial. A model with a high number of arterial segments results in a more realistic description of the system, but also requires a high number of parameters with associated uncertainties. In this paper, we present a method to optimize/reduce the number of arterial segments included in one-dimensional blood flow models, while preserving key features of flow and pressure waveforms. We quantify the preservation of key flow features for the optimal network with respect to the baseline networks (a 96-artery and a patient-specific coronary network) by various metrics and quantities like average relative error, pulse pressure and augmentation pressure. Furthermore, various physiological and pathological states are considered. For the aortic root and larger systemic artery pressure waveforms a network with minimal description of lower and upper limb arteries and no cerebral arteries, sufficiently captures important features such as pressure augmentation and pulse pressure. Discrepancies in carotid and middle cerebral artery flow waveforms that are introduced by describing the arterial system in a minimalistic manner are small compared with errors related to uncertainties in blood flow measurements obtained by ultrasound.

1. Introduction

Computational models of the cardiovascular system are commonly separated into three-dimensional (3D), one-dimensional (1D) and lumped models (0D). One of the first attempts to model pressure and flow waveforms was through the classical 0D Windkessel (WK) model [1]. A noteworthy extension to this was presented in [2] where a resistance element representing the characteristic impedance was added, and many variations and extensions have been proposed [3]. The most important drawback of the family of 0D models is inherent in the assumption of infinite wave velocity and that spatially distributed parameters are modelled as single point parameters.

Through the years distributed models with various degrees of detail have been suggested. In [4,5], the systemic circulation was modelled as two asymmetric parallel branches, one supplying the head and upper limbs, and one supplying the rest of the body. In [6], a model consisting of the 33 largest systemic arteries was tested using an *in vitro* experiment. In [7], the arterial network was expanded to include 55 arterial 1D segments. In [8], a complete description of the systemic arterial tree containing the largest arteries of the head and upper and lower body was validated using *in vivo* measurements. The study also includes a detailed overview of 1D models up until 2009, highlighting their variation in detail and complexity. More recently, in [9], a model accounting for pulse wave

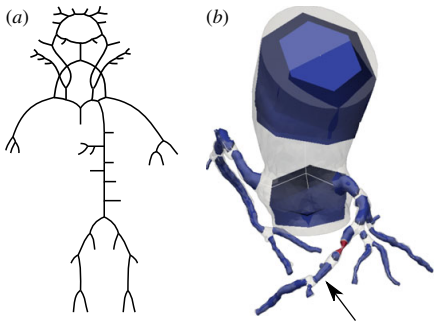

Figure 1. Two baseline models were used in this work: a model containing 96 arterial segments in which parameters and topology were adapted from [9] (*a*), and a patient-specific coronary network (*b*). The arrow indicates the location of invasive pressure measurements, and the section coloured in red is a significant stenosis.

propagation in all regions of the circulation including approximately 400 arteries and 350 veins was presented. Yet others have modelled the arterial system in a very high level of detail including more than 2000 arteries [10,11].

We have come a long way in creating realistic and detailed descriptions of the entire arterial tree and circulatory system. However, given the near endless number of small arteries and capillaries in the human body, the network has to be truncated at a certain level. Since reliable measurements of flow or pressure at all terminal sites are practically impossible to obtain, outflow boundary conditions are commonly set through simpler models representing the peripheral circulation. Indeed the above-mentioned family of 0D WK models have been the preferred choice for providing boundary conditions at terminal branches.

There is little consensus in the scientific community on the level of detail of the computational domain. Furthermore, few studies have focused on the errors and limitations associated with truncating the arterial network at given sites. In [8], they state that a detailed description of the cerebral circulation is required in order to attain accurate and physiological flow predictions in the common carotid artery. In [12], they found that the arterial tree could be truncated after the first generation of bifurcations without significantly altering pressure and flow waveforms, if matched three-element WK outflow models were used. In [13], they presented a method for lumping 1D arterial segments into three-element WK models and applied their method on a network of 55 arteries (excluding the circle of Willis).

Here, we present a sound mathematical framework that enables us to find the necessary arteries to include for a given clinical application. The framework involves finding the model with the fewest number of arteries that is still able to produce pressure and flow waveforms below a certain error threshold compared with a corresponding detailed (baseline) model (figure 1). This approach reduces the number of uncertain input parameters, while still assuring that the simplifications do not limit the model predictions. We illustrate the framework for different clinically relevant quantities of interest: central aortic and larger systemic artery pressure waveforms, common carotid and middle cerebral artery flow waveforms and coronary pressure waveforms. We note that our framework is intended to be used in an early stage as a tool for model selection that aims at minimizing total uncertainty.

2. Material and methods

2.1. Framework for balancing topological complexity with model error

Here, we present a framework for reducing the number of vessel segments still assuring wanted features of pressure and/or flow to be within acceptable agreement with the corresponding full model:

— Define a baseline model.
— Locate the quantity of interest appropriate for the problem (e.g. aortic pressure and/or carotid flow).
— Define a threshold for pressure and/or flow (e.g. RMS-error, pulse or mean pressure).
— Create reduced models by applying the methods described in §2.4.1 or §2.4.2, and solve the 1D networks.
— Find the network with the fewest number of arteries subject to the constraint of the threshold.

2.2. Arterial baseline models

We applied our new methodology on two arterial models, both illustrated in figure 1.

2.2.1. Systemic arterial network

The first baseline model considered includes 96 of the largest systemic arteries, in which parameters and geometry were adapted from Mynard *et al.* [9]. They compared model-derived pressure/flow waveforms with published *in vivo* waveforms from healthy adults, validating the model's capability of providing realistic waveforms throughout the arterial tree.

2.2.2. Coronary network

The second baseline model considered in this work was based on a series of invasive and non-invasive measurements of a patient (sex: female, age: 58, height: 162 cm, weight: 78 kg) with positive findings of stable coronary artery disease after clinical inspection and coronary computed tomography angiography (CCTA) examination. The data were collected as part of an ongoing clinical trial at St Olavs Hospital, Trondheim, Norway [14]. Cardiac output (CO) was measured by transthoracic Doppler echocardiography using a GE Vivid E95 scanner (GE Vingmed Ultrasound, Horten, Norway). The patient was further referred to invasive angiography, and a Verrata Plus (Philips Volcano, San Diego, USA) pressure wire was used to obtain pressure tracings at the coronary ostium and distal of an epicardial stenosis. Proximal, P_p and distal, P_d pressure tracings are shown in figure 8. The last 30% of the cardiac cycle is highlighted and was used to compute the instantaneous wave-free ratio (iFR), which is a drug-free index of the significance of the stenosis [15]. Measurement of fractional flow reserve (FFR) [15], obtained during drug-induced hyperaemia (maximum coronary flow) was also available. The coronary geometry was segmented using the open-source software ITK-SNAP [16], the surface was then meshed using the open-source library Vascular Modeling ToolKit [17]. 1D domains were extracted from the 3D volume mesh by computing equivalent axisymetric cross-sectional areas along centrelines. Stenotic regions were automatically detected using a Gaussian filter-based approach [18].

2.3. Numerical formulation

2.3.1. One-dimensional flow solver

The solutions of pressure and flow waveforms presented here were obtained using the 1D flow solver STARFiSh [19]. The hyperbolic

partial differential equations for blood flow in compliant vessels are written in terms of pressure and flow variables (P, Q):

$$\frac{\partial A}{\partial P}\frac{\partial P}{\partial t}+\frac{\partial Q}{\partial x}=0 \tag{2.1a}$$

and

$$\frac{\partial Q}{\partial t}+\frac{\partial Q^2/A}{\partial x}=-\frac{A}{\rho}\frac{\partial P}{\partial x}+\frac{f}{\rho}, \tag{2.1b}$$

and solved using the explicit MacCormack scheme [20]. Here, t is the time, x is the axial coordinate, f is the frictional term and is given by $-2(\zeta+2)\mu\pi U$, where ρ is the density (1060 kg m^{-3}), μ is the viscosity of blood (3.5 mPa s), A is the cross-sectional area and U is the cross-sectional averaged velocity. The following velocity profile was prescribed:

$$u(x,\xi,t)=U(x,t)\frac{\zeta+2}{\zeta}\left[1-\left(\frac{\xi}{r}\right)^{\zeta}\right], \tag{2.2}$$

where $r(x,t)$ is the lumen radius, ξ is the radial coordinate and $\zeta=9$ is the polynomial order. At arterial connections compatibility of propagating characteristic variables were enforced [7] in addition to conservation of mass and a coupling equation for the pressure, i.e.:

$$\sum_{i=1}^{N} Q_i=0 \tag{2.3a}$$

and

$$P_1+\frac{\rho}{2}U_1^2=P_i+\frac{\rho}{2}U_i^2+\Delta P \quad i=2,\ldots,N, \tag{2.3b}$$

where N is the number of vessels in the connection, and ΔP is an additional pressure loss which was set equal to zero for normal connections. At arterial stenoses, the flow regime is 3D and the 1D assumptions no longer hold. Stenotic regions were thus removed and treated as junctions with $N=2$, however, now with an additional experimental-based pressure loss term given by Liang *et al.* [21]:

$$\Delta P=K_{\text{visc}}Q+K_{\text{exp}}Q|Q|, \tag{2.4}$$

where the viscous, K_{visc} and expansion, K_{exp} coefficients were calculated based on geometrical features, as described in [21].

The pressure–area relation assumes thin-walled elastic vessels and can be derived from Laplace's Law:

$$P=P_{\text{dia}}+\frac{\beta}{A_{\text{d}}}(\sqrt{A}-\sqrt{A_{\text{d}}}),\quad \beta(x)=\frac{4}{3}\sqrt{\pi}Eh, \tag{2.5}$$

where P_{dia} is the diastolic pressure with corresponding cross-sectional area A_{d}, E is the elastic modulus and h is the thickness of the vessel wall. The stiffness parameters E h are related to the pulse wave velocity c and have been obtained using the relation [22]:

$$c_{\text{d}}^2=\frac{2}{3\rho}\frac{Eh}{r_{\text{d}}}=\frac{2}{3\rho}[k_1\exp(k_2 r_d)+k_3], \tag{2.6}$$

where r_{d} is the radius at diastolic pressure, and the values for k_1, k_2 and k_3 were set to 3×10^6 g s^{-2} cm^{-1}, -9 cm^{-1} and 33.7×10^4 g s^{-2} cm^{-1} for systemic arteries and 20×10^6 g s^{-2} cm^{-1}, -22.5 cm^{-1} and 86.5×10^4 g s^{-2} cm^{-1} for coronary arteries, respectively [9].

2.3.2. Boundary conditions

For the 96-artery model, inflow boundary conditions (prescribed flow rate Q) and outflow boundary conditions (three-element Windkessel models, WK3) and all other parameters were adapted from Mynard & Smolich [9]. For the coronary network, the proximal pressure tracing was prescribed at the aortic root. In contrast to systemic arteries, coronary arteries experience increased impedance during systole due to the contraction and increased pressure in the left ventricle. To account for this effect, a lumped parameter WK model WK$_{\text{cor}}$ was used at coronary outlets [23]. A schematic of the model is shown in figure 9 in appendix A.1 and the *a priori* computed left ventricle pressure waveform is shown in figure 8. The left ventricle pressure waveform was obtained by coupling a varying elastance (VE) heart model to a WK3 model [24], and further by parameter optimization to minimize the discrepancy between P_{p} and P_{ao}, where P_{ao} is the aortic pressure resulting from the VE-WK3 model. The total arterial resistance, R_{tot} was estimated from CO, mean arterial pressure, $\bar{P}_{\text{p}}$ and outflow WK pressure, $P_{\text{out,WK}}$ (5 mmHg) according to Ohm's Law. Total arterial compliance was estimated from the VE-WK3 model. About 4.5% of CO was assumed to supply coronary arteries and used to estimate total coronary resistance and compliance, and was further distributed among coronary outlets according to Murray's Law [25]. Simulation of a hyperaemic state is necessary for FFR calculations. Hyperaemia was modelled by reducing the resting resistance of the coronary outlets by a factor α. The value of α was based on the work of Uren *et al.* [26] who studied myocardial blood flow and resistance in relation to the severity of coronary stenosis, and was set to 3 for 'healthy' outlets, and to 1.25 for outlets distal of the coronary stenosis. For details see appendix A.2.1.

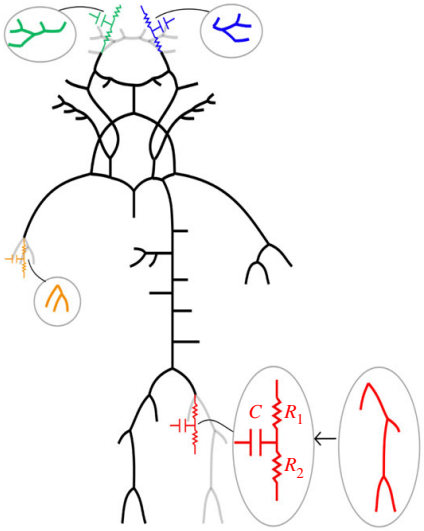

Figure 2. An example of a reduced network that has been obtained from the baseline model in figure 1 by lumping 1D model segments into WK3 models. Lumped 1D model segments are shown in colour.

2.4. Network reduction

Network reduction involves lumping distributed 1D segments into 0D parameter models, specifically WK models, intended to represent the same physical problem. Each WK model represents all arteries situated distal of the point of interest with resistance elements and capacitors in series and parallel, as visualized in figure 2.

2.4.1. Method 1, algebraic estimation of lumped parameters

Here, we present a method for network reduction which was adapted from Epstein *et al.* [13]. The method was described and applied on a baseline network only including bifurcations. In this work, we have used a different way of estimating the lumped resistance and compliance that can also be applied on networks containing loops and anastomosis. We have also expanded the procedure to account for arterial stenoses.

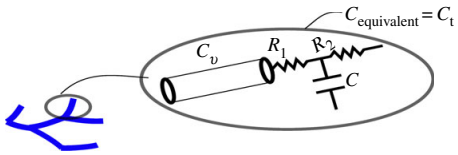

Figure 3. Illustration of an arterial 1D model segment coupled to a WK3 model that may be lumped into an equivalent compliance C_t according to equation (2.10). (Online version in colour.)

2.4.1.1. Estimation of lumped resistance

The linearized version of equations (2.1*a*) and (2.1*b*) can be written in terms of the steady-state variables $\bar{P}$, $\bar{Q}$ and $\bar{A}$:

$$\bar{Q}_{\text{in}} = \bar{Q}_{\text{out}} \tag{2.7a}$$

and

$$\bar{P}_{\text{in}} = \bar{P}_{\text{out}} + \int_0^l \frac{2(\zeta+2)\pi\mu}{\bar{A}^2}\,\mathrm{d}x, \tag{2.7b}$$

where l is the length of the segment, and the subscripts 'in' and 'out' denote variables at the inlet and outlet of the segment, respectively. Equations (2.7*a*) and (2.7*b*) may then be combined with equations (2.3*a*)–(2.3*b*) and equation (2.5) to form a system of nonlinear algebraic equations. The system was solved iteratively by employing Picard linearization. $\bar{P}$ and $\bar{Q}$ is in such an estimate of the time average of $P(t)$ and $Q(t)$, and once solved for, resistance may be estimated anywhere in the network using Ohm's Law:

$$R = \frac{\bar{P} - P_{\text{out,WK}}}{\bar{Q}}. \tag{2.8}$$

2.4.1.2. Estimation of lumped compliance

We can estimate the compliance (C_v) of a vessel by integrating over the length of the 1D model segment [13]:

$$C_v = \frac{K_1}{\rho}, \quad K_1 = \int_0^l \frac{\bar{A}}{\bar{c}^2}\,\mathrm{d}x. \tag{2.9}$$

Furthermore, we estimated the compliance C_t of a terminal vessel (figure 3) coupled with a WK3 with proximal resistance, R_1, compliance, C and peripheral resistance, R_2 [13]:

$$C_t = \frac{C_v R_2 + C_v R_1 + C R_2 + C_v R_v}{R_2 + R_1 + R_v}. \tag{2.10}$$

Lumped compliance of terminal vessels coupled to WK_{cor} models (see figure 9 in appendix A.2.1.) with compliances C_a and C_m were estimated according to:

$$C_t = C_v + C_a + C_m. \tag{2.11}$$

The total compliance contribution of vessels distal of a point of truncation was then obtained using equation (2.9) for non-terminal vessels and equation (2.10) or equation (2.11) as appropriate for terminal vessels, together with summation rules for compliances/capacitors in series and parallel. See appendix A.2.1. for details.

2.4.1.3. Lumping vessels distal of a site of truncation

With the lumped resistance, (equation (2.8)) and compliance (equations (2.9)–(2.11)), as defined above we may replace all vessels distal of a point of interest with a WK model. Systemic arteries were replaced by WK3 models in which R_1 was set equal to the characteristic impedance, Z_c:

$$Z_c = \frac{\rho\bar{c}}{\bar{A}}. \tag{2.12}$$

Lumped coronary arteries were replaced by WK_{cor} models and the lumped resistance and compliance were divided among the resistance and compliance parameters of the WK_{cor} model as described in appendix A.2.1.

2.4.2. Method 2, optimization of lumped parameters

Method 1 is based solely on the topology and properties of the baseline model. This means that we can use the method without solving the baseline model. However, the parameters in the WK models that replace the removed vessels are not necessarily the ones that correspond with the least discrepancy between the baseline and reduced networks. This motivates another method which is based on parameter optimization. Since the WK models are lumped models with governing ordinary differential equations (ODEs), we suggest a procedure that treats every truncated site independently. The optimization is thus performed by taking the flow from the 1D solution of the baseline model as given inflow to the WK models, then solving for the unknown pressure. Furthermore, we seek to minimize the error between the pressure obtained by solving the ODE with the corresponding 1D baseline solution. In the following, we explain the procedure for the WK3 model, though it can be easily expanded to other lumped parameter outflow models. Either one, two or all three of R_1, C and R_2 were allowed to vary to minimize the error. If only one of R_1 and R_2 was optimized, the total resistance $R_1 + R_2$ was found from $(P_{\text{avg}} - P_{\text{out,WK}})/Q_{\text{avg}}$, where P_{avg} and Q_{avg} are the time-averaged pressure and flow from the 1D baseline solutions. The method may be summarized in the following steps:

(1) Calculate the flow and pressure waveforms of the 1D baseline model.
(2) Locate the sites where WK3 models will replace distal vessels.
(3) Calculate values of $R_1 + R_2$ from P_{avg}, Q_{avg}, and C using Method 1 (§2.4.1).
(4) Use the flow from the 1D baseline model as given inflow of the WK3 ODE, with parameters R_1, C and R_2.
(5) Choose parameters to be optimized and use parameters from point 3 otherwise and as initial guess.
(6) Solve the WK3 ODE for the unknown pressure, P_{WK3}.
(7) Find the parameters that minimize the discrepancy between P_{WK3} and the corresponding pressure waveform from the solution of the 1D baseline model. We used the average relative error, calculated by equation (2.13*a*) as the measure of discrepancy.

Based on a parameter correlation and identifiability analysis, we chose to optimize on the subset of parameters ($[\theta_1, \theta_2] = [R_1/R_2, C]$), where $R_1 + R_2$ was kept constant. See appendix A.3.2. for details.

2.5. Error metrics

The following error metrics were used to compare pressure and flow waveforms obtained from the baseline (B) and reduced (R) models:

$$\epsilon_{P,\text{avg}} = \frac{1}{N_t}\sum_{i=1}^{N_t}\left|\frac{P_i^{\text{R}} - P_i^{\text{B}}}{P_i^{\text{B}}}\right|, \quad \epsilon_{Q,\text{avg}} = \frac{1}{N_t}\sum_{i=1}^{N_t}\left|\frac{Q_i^{\text{R}} - Q_i^{\text{B}}}{\max_j(Q_j^{\text{B}})}\right|, \tag{2.13a}$$

$$\epsilon_{P,\text{sys}} = \frac{|P_{\text{sys}}^{\text{B}} - P_{\text{sys}}^{\text{R}}|}{P_{\text{sys}}^{\text{B}}}, \quad \epsilon_{P,\text{dia}} = \frac{|P_{\text{dia}}^{\text{B}} - P_{\text{dia}}^{\text{R}}|}{P_{\text{dia}}^{\text{B}}}, \tag{2.13b}$$

$$\epsilon_{PP} = \frac{|PP^{\text{B}} - PP^{\text{R}}|}{PP^{\text{B}}}, \tag{2.13c}$$

$$\epsilon_{P,\text{aug}} = \frac{|\{P_{\text{sys}}^{\text{B}} - P_{\text{infl}}^{\text{B}}\} - \{P_{\text{sys}}^{\text{R}} - P_{\text{infl}}^{\text{R}}\}|}{PP^{\text{B}}} \tag{2.13d}$$

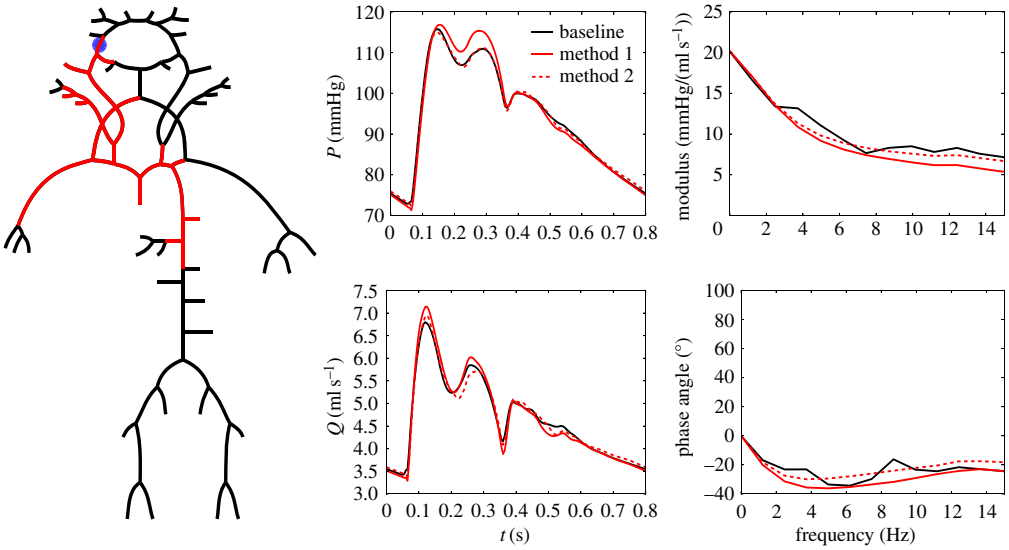

Figure 4. Comparison of Method 1 and Method 2 for network reduction. Baseline model in black and reduced models in red together with pressure and flow waveforms at the inlet of the right internal carotid artery. Impedance modulus and phase angle are also shown.

and

$$\epsilon_{\mathrm{iFR}} = |\mathrm{iFR}_B - \mathrm{iFR}_R|, \tag{2.13e}$$

where N_t is the number of time points in a cardiac cycle, i represents a certain time point with corresponding baseline, P_i^{B} and reduced, P_i^{R} pressure and flow (Q_i^{B}, Q_i^{R}), respectively. $\epsilon_{Q,\mathrm{avg}}$ was normalized by the maximum flow of the baseline model over one cardiac cycle, $\max_j(Q_j^{\mathrm{B}})$, to avoid division by numbers close to zero. The maximum (P_{sys}) and minimum pressure (P_{dia}) was used to calculate the systolic ($\epsilon_{P,\mathrm{sys}}$), and diastolic ($\epsilon_{P,\mathrm{dia}}$) error, respectively. The pulse pressure, PP is defined as $P_{\mathrm{sys}} - P_{\mathrm{dia}}$. ϵ_{PP} is the error in pulse pressure and $\epsilon_{P,\mathrm{aug}}$ is the error in augmentation pressure, both normalized by the pulse pressure. $P_{\mathrm{infl}}^{\mathrm{B}}$ is the pressure at the inflection point in early systole [27]. ϵ_{iFR} is the difference between predicted iFR from baseline and reduced model.

2.6. Application to different physiological and pathological states

The parameters for the baseline 96-artery model were based on data from healthy, young adults [9]. In this part of the study, however, we re-parametrized a series of optimal networks to represent (1) normal ageing, (2) a pathological state of aortic coarctation and (3) states of different heart rate, ejection time and stroke volume. We note that no information from the baseline model was used to re-parametrize the reduced models.

2.6.1. Normal ageing

Normal ageing was simulated by increasing total arterial resistance by a factor of 1.1, and decreasing total arterial compliance by a factor of 2. Arterial stiffening is most marked in the proximal aorta and its major branches—brachiocephalic, carotid, subclavian [28]. The stiffness parameter β for these arterial segments was increased by a factor of 2.5, whereas it was increased by a factor of 1.5 for all other segments. Finally, the compliance of the WK3 models were modified so that the total arterial compliance (sum of WK3 compliance of terminal segments and integrated 1D compliance) was decreased by a factor of 2. The total arterial resistance was modified by increasing the peripheral resistance in all outflow WK3 models. See appendix A.5 for details.

2.6.2. Aortic coarctation

Aortic coarctation was simulated by introducing a 1 cm long, 50% diameter stenosis in the thoracic aorta. This corresponds to segment Id 18 in the electronic supplementary material.

2.6.3. Heart rate, ejection time and stroke volume

Heart rate, ejection time and stroke volume were modified according to the study by Weissler *et al.* [29]. They studied relationships between left ventricular ejection time, ET, stroke volume, SV and heart rate, HR, in normal individuals. We modified the original aortic inflow curve for the 96-artery model to represent the two extreme cases in terms of HR in their study (HR: 56 bpm, ET: 0.315 s, SV: 106 ml and HR: 120 bpm, ET: 0.2 s, SV: 44 ml). For the latter, total arterial resistance was increased by a factor of 1.67 and compliance halved (effecting the distributed parameters as described for normal ageing), in order to obtain physiological pressure waveforms.

3. Results

3.1. Comparison of Method 1 and Method 2 for network reduction

Figure 4 shows the 96-artery model (black) reduced to a 25-artery model (red). Solution of pressure and flow waveforms at the inlet of the right internal carotid artery, obtained from the baseline model and both methods for network reduction, are also shown. Method 1 overestimated internal carotid pressure in mid systole (ϵ_{PP} was 6.2% for Method 1 and 0.2% for Method 2). Furthermore, Method 2 captured the overall shape of pressure and flow waveforms better than Method 1. Average errors, $\epsilon_{P,\mathrm{avg}}$ between full and reduced models were 1.45% for Method 1 and 0.57% for Method 2. Similarly, $\epsilon_{Q,\mathrm{avg}}$ was 1.47% and 1.16%, respectively. Figure 4 also shows the impedance modulus and angle for the site of interest, calculated in the frequency domain as explained in [30].

Table 1. Summary of results from applying the framework outlined in §2.1, on the 96-artery baseline model. For cases where there are more than one quantity of interest, the final error was calculated as the average of the error for the individual quantities. Ref. denotes the reference case, and the threshold used for the optimization is given in brackets. The errors are also shown for states of normal ageing, aortic coarctation (coarc.) and for the two aortic inflow curves as defined in §2.6. All errors are in percentage. The associated figure numbers are referenced below the error, where available.

quantity of interest	no. of arteries	error-metric	ref.	ageing	coarc.	inflow 1	inflow 2
aortic and brachial pressure	29	$\epsilon_{P,\mathrm{sys}} + \epsilon_{P,\mathrm{dia}}$	0.25 (0.3) 5	2.26 5	0.37 —	0.14 —	1.58 —
aortic and brachial pressure	15	$\epsilon_{P,\mathrm{sys}} + \epsilon_{P,\mathrm{dia}}$	0.92 (1.0) 5	1.0 5	0.27 —	1.13 —	1.3 —
aortic pressure	31	$\epsilon_{PP} + \epsilon_{P,\mathrm{aug}}$	0.68 (0.7) 5	0.97 5	1.91 —	0.41 —	1.27 —
aortic and brachial and carotid and femoral pressure	31	$\epsilon_{P,\mathrm{avg}}$	0.33 (0.4) 13	0.47 13	0.24 15	0.41 16	0.85 16
carotid flow	25	$\epsilon_{Q,\mathrm{avg}}$	0.87 (0.9) 6	1.53 14	1.09 —	0.81 17	2.97 17
carotid flow	5	$\epsilon_{Q,\mathrm{avg}}$	3.35 (3.4) 6	5.2 14	— —	2.93 17	6.3 17
r. middle cerebral flow	38	$\epsilon_{Q,\mathrm{avg}}$	0.59 (0.6) 6	1.13 14	0.66 —	0.66 17	2.88 17
r. middle cerebral flow	15	$\epsilon_{Q,\mathrm{avg}}$	1.58 (1.6) 6	2.64 14	— —	1.72 17	4.38 17

3.2. Framework for optimizing topological complexity

A summary of the quantities of interest, error metrics and values for the network reduction framework applied on the 96-artery model is given in table 1. Here, error metrics are also presented for the cases where parameters were altered to simulate different physiological and pathological states (see §2.6). References to associated figures are also given. In particular, a threshold based on $\epsilon_{P,\mathrm{sys}} + \epsilon_{P,\mathrm{dia}}$ at the aorta and brachial artery was used in the top two examples in figure 5. The waveforms for the baseline model and optimal reduced networks are shown in solid lines, and the dashed lines represent the case when the models were altered to represent normal ageing. In the last example, a threshold based on augmentation and pulse pressure was used ($\epsilon_{P,\mathrm{aug}} + \epsilon_{PP} < 0.7\%$). Furthermore, in order to ensure that interaction between different regions in the network and that pressure propagation are correctly captured throughout the larger systemic arteries, a threshold based on pressure waveforms at four locations was used in figure 13 in appendix A.5. Here, the average $\epsilon_{P,\mathrm{avg}}$ for the aortic root, common carotid, brachial and femoral artery pressure waveforms was required to be less than 0.4%. Additionally, results are shown for $\epsilon_{Q,\mathrm{avg}}$ less than 0.9 and 3.4% for the right common carotid artery and $\epsilon_{Q,\mathrm{avg}}$ less than 0.6 and 1.6% for the middle cerebral artery in figure 6. Method 2 (§2.4.2) was used to reduce the networks in all these cases.

In the top part of figure 7, ϵ_{iFR} was set to 0.033, which is the standard deviation of repeated iFR measurements, according to the study by Johnson *et al.* [15]. The results are visualized through the distal pressure waveform, P_{d}. All side branches except those distal of the measured location can be replaced by lumped $\mathrm{WK}_{\mathrm{cor}}$ models with no visible effect and with $\epsilon_{\mathrm{iFR}} < 0.000012$. If the threshold is increased to 0.04 the network can be reduced to its most simplistic realization, as visualized in the bottom part of the figure. The predicted velocity and the *in vivo* pressure waveforms are also shown. iFR was measured to 0.40, whereas the predicted value was 0.42 for the baseline network, and 0.42 and 0.38 for the reduced networks, respectively. For FFR, the measured value was 0.52, whereas the predicted value was 0.48 for the baseline network and both of the reduced networks. Method 1 (§2.4.1) was used to reduce the coronary networks.

4. Discussion

In this study, we have presented a novel approach which optimizes the number of arterial segments for 1D blood flow models. We have illustrated the framework on a 96-artery and a coronary baseline model, and two methods for network reduction have been incorporated: a purely algebraic method (Method 1, §2.4.1) and a novel method based on optimization (Method 2, §2.4.2).

4.1. Comparison of methods for network reduction

A major difference in the waveforms obtained from Method 1 and Method 2 may be seen in the systolic part of the cycle, where the pressure obtained using Method 1 was over-predicted. This was observed as a general distinction between the two methods, and is exemplified in figure 4. However, the diastolic phase is very similar, indicating that the discrepancy is not a result of differences in the values of compliance in the WK3 models. The diastolic decay of pressure can be approximated by an exponential function, with an exponent given by the product of the peripheral resistance (R_2) and the compliance (C) [31]. Thus changes in the compliance directly effect the diastolic

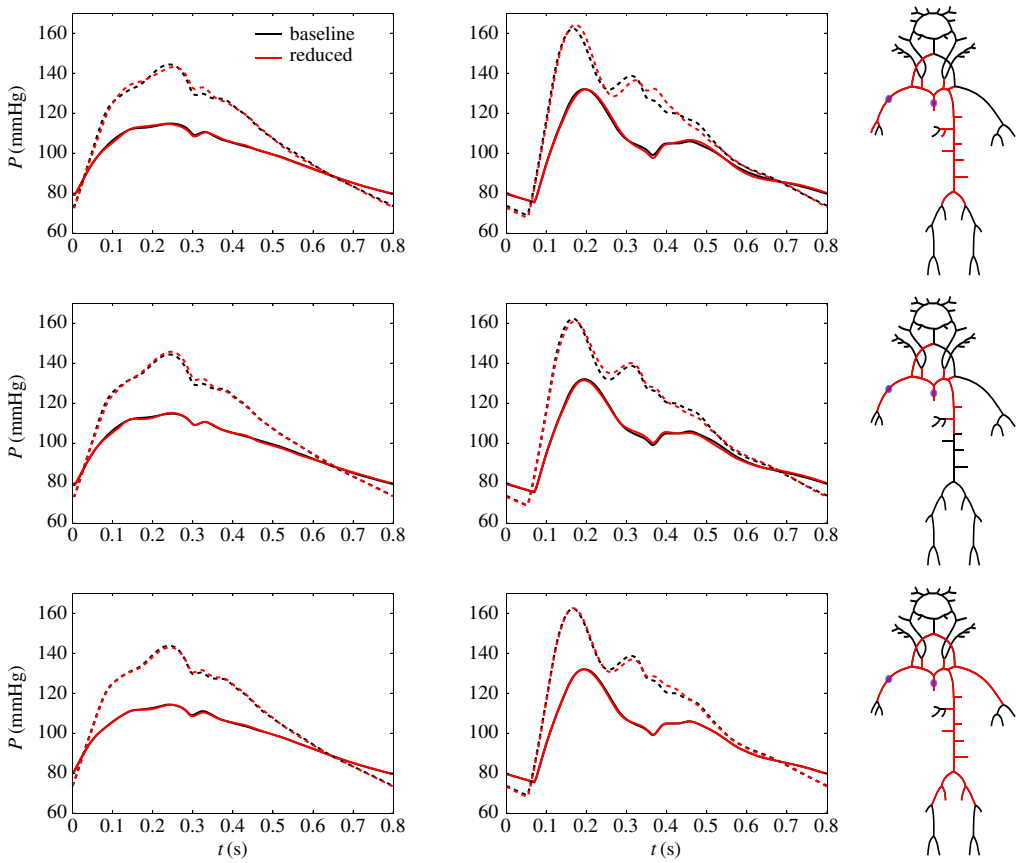

Figure 5. Optimal networks and corresponding waveforms (solid lines) obtained from the 96-artery baseline model with pressure at midpoint of ascending aorta (left) and right brachial artery (middle) set as quantities of interest. In the top and middle rows, an averaged (of the two quantities of interest) error threshold of $\epsilon_{P,\mathrm{sys}} + \epsilon_{P,\mathrm{dia}}$ less than 0.3% (top row) and 1.0% (middle row) was used. In the last case, an error threshold of $\epsilon_{P,\mathrm{aug}} + \epsilon_{PP}$ less than 0.7% was used for the aorta. Dashed waveforms correspond to simulations of normal ageing as described in §2.6.

shape, whereas changes in R_1 only have secondary effect. On the other hand, R_1 has a direct effect on the systolic part of the cycle. Inspection of the values used for the proximal resistance in the WK3 models revealed that Z_c (Method 1) was in general higher than $R_{1,\mathrm{opt}}$ (Method 2) for the larger systemic arteries. The addition of the characteristic impedance to the original two-element WK model was based on frequency analysis of modulus and phase of the input impedance along the aorta. By including the characteristic impedance, the input impedance modulus of the modified WK matched *in vivo* measurements at high frequencies [2,31]. We also observed (not shown here) better matching of the modulus at the aorta for high frequencies, between baseline and reduced models obtained with Method 1 than with Method 2; however, the same is not true for this more distal location (internal carotid). Impedance phase, on the other hand, was captured better by Method 2 for some frequencies (particularly between 5 and 7 Hz), as can also be seen in the phase of the first minima of the flow waveform (≈ 6 Hz). Minimization of high-frequency oscillations has also been an incentive for using matched ($R_1 = Z_c$) WKs as outflow BC's in 1D blood flow models [12]. However, the price to pay is an overprediction of pressure in systole.

4.2. Optimization of topological complexity

4.2.1. Central and larger systemic artery pressure waveforms

Pressure measured with a cuff and sphygmomanometer in the brachial artery is used routinely and accepted as an important predictor of future cardiovascular risk. However, studies indicate that central blood pressure (CBP) relates more strongly to cardiovascular events [32]. Systolic and pulse pressures are amplified as the pulse wave propagates through the larger systemic arteries. This amplification may vary significantly among subjects [32], making it difficult to map measurements of pressure at more peripheral sites directly to CBP.

Although it is still unclear if routine measurement/estimation of CBP will provide significantly improved risk stratification [33], the 1D nonlinear equations for blood flow can be used to investigate pulse wave amplification [8,34,35]. In previous studies, the topology of the 1D model was chosen *ad hoc*. Our novel framework provides a mathematical approach to determine the optimal topology to study pulse wave amplification from the aortic root to the brachial artery.

The results presented in the first two rows of figure 5 indicate that inclusion of detailed descriptions of upper and

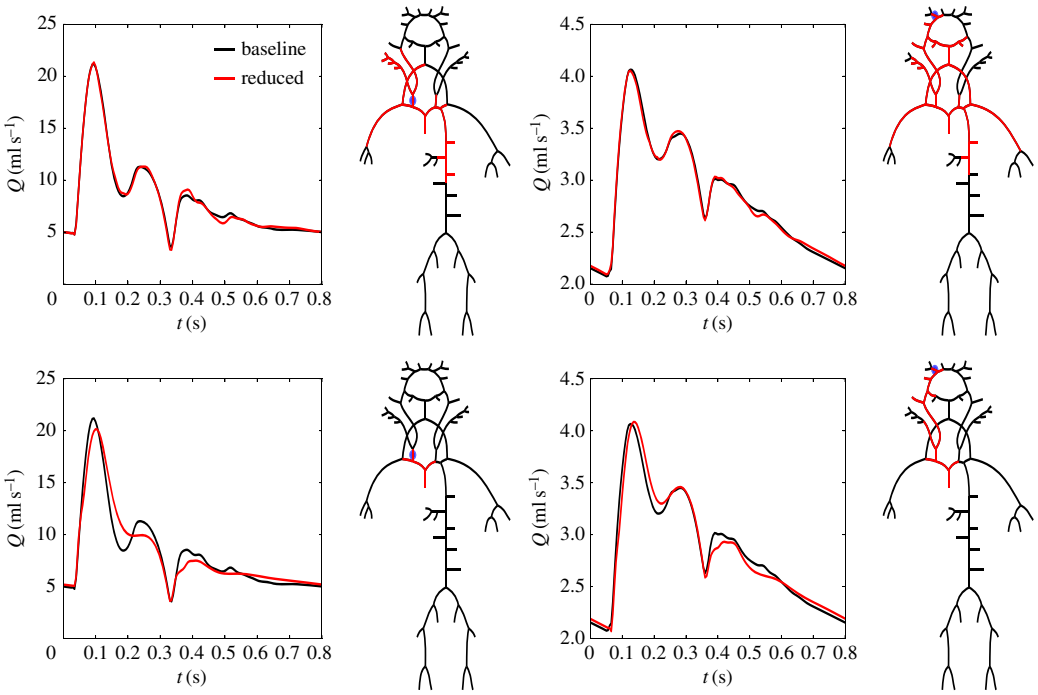

Figure 6. Optimal networks obtained from the 96-artery baseline model with the flow at the distal end of the right carotid artery set as quantity of interest (left panel) and with 0.9 and 3.4% average error thresholds, respectively. The right panel show results when the flow at the proximal end of the right middle cerebral artery was set as quantity of interest and with 0.6 and 1.6% average error thresholds, respectively.

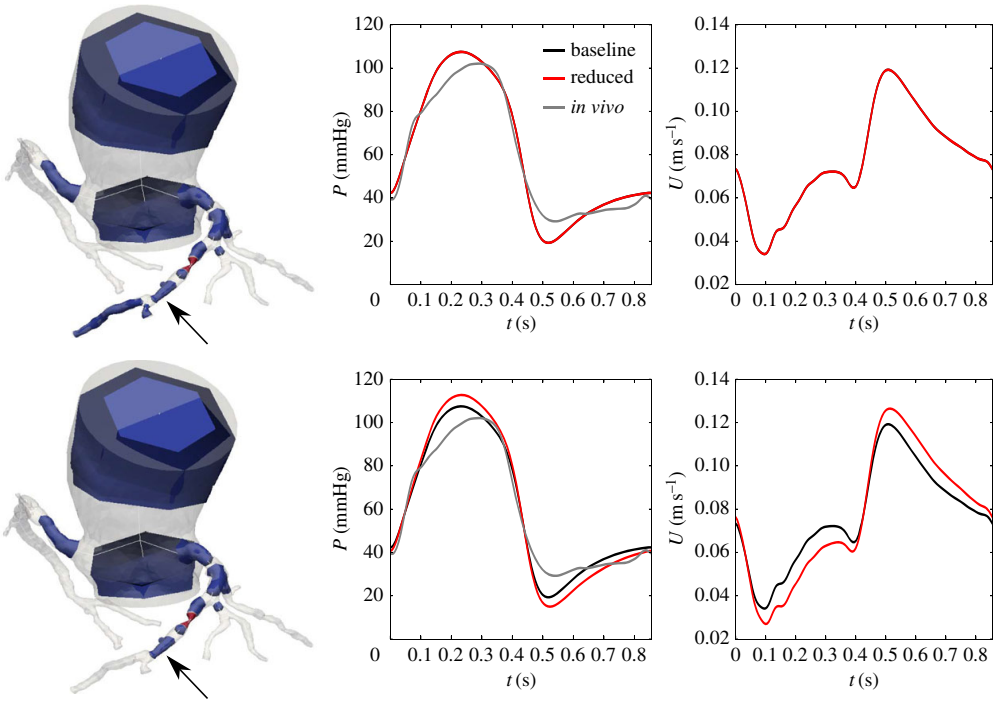

Figure 7. Optimal networks obtained from the coronary network with difference in iFR set as quantity of interest, with $\epsilon_{iFR} < 0.00012$ (top) and $\epsilon_{iFR} < 0.04$ (bottom). Results are visualized through the distal pressure waveform. *In vivo* pressure waveform and predicted velocity waveforms are also shown. The arrow indicates the location of the waveforms, and the red section a significant stenosis.

lower limbs are not needed in order to study pulse wave amplification from the aortic root to the brachial artery. Moreover, the entire cerebral circulation can be replaced by WK3 models with negligible effects on aortic and brachial pressure waveforms. This is reasonable since these are relatively small and stiff arteries for which the behaviour is well captured by WK3 models [3]; however, it is important to note that the proximal part of the aorta, which accounts for about 50% of total systemic compliance, needs to be kept in the reduced 1D model.

Both pulse pressure and augmentation pressure, and their relation (augmentation index) is associated with cardiovascular risk [36]. Even though the aortic pressure waveforms obtained by the reduced models in the top two examples in figure 5 captured the pulse pressure very well, some subtle deviations are visible in the systolic part of the waveforms. This could have an effect on the calculated augmentation pressure, and thus also on evaluations of cardiovascular risk. In the last example in figure 5, an error threshold of $\epsilon_{PP} + \epsilon_{P,\mathrm{aug}}$ of 0.7% at the aorta, was used, and results indicate that this 31-artery model captures the most important features of wave propagation for central aortic pressure. A similar model was found when a combined threshold of average $\epsilon_{P,\mathrm{avg}}$ of 0.4% was set for four arterial sites; midpoint of ascending aorta, right common carotid artery, right brachial artery and left femoral artery, as illustrated in figure 13 in appendix A.5. This network was also able to capture waveform features with good qualitative and quantitative precision when the model was re-parametrized to model different physiological and pathological states.

4.2.2. Carotid and cerebral circulation

In the study by Reymond *et al.* they compared carotid flow predictions with and without description of the cerebral circulation and stated that a detailed description was necessary in order to produce physiological correct waveforms. Our results, on the other hand, indicate that the entire cerebral circulation can be appropriately lumped into WK3 models effecting only the diastolic part of the flow waveforms and with $\epsilon_{Q,\mathrm{avg}} < 0.9\%$, as shown in figure 6. Furthermore, by increasing the threshold to 3.4% the network is reduced to a very simplistic model including only five arterial segments. Though the overall features are represented in this five-artery model, the arterial tree is truncated close to the carotid artery and will thus be more influenced by the WK3 models. High-frequency details are not described well by the three-element WK [31], which in this case is visible through the smoothing of the second and third peaks of the flow waveform. Such errors were magnified when the model was transformed to represent normal ageing, as visualized in figure 14.

Figure 6 also shows results with flow rate at the inlet of the right middle cerebral artery set as the quantity of interest. This site is located more distal than the other quantities of interest studied in this work, and as can be seen in the case where a threshold of $\epsilon_{Q,\mathrm{avg}} < 0.6\%$ was considered, the circle of Willis can be 'broken' and represented by WK3 models without altering the flow waveform significantly. Furthermore, the arterial tree can be truncated in close proximity to the middle cerebral artery without introducing significant constraints on the solution, more so than was the case for the right common carotid artery. This is attributed to the fact that the flow in this region is more dominated by frictional forces resulting in pressure and flow waveforms that are of similar shape and phase and can be more readily described by the WK3 model. Moreover, by increasing the threshold to $\epsilon_{Q,\mathrm{avg}} < 1.6\%$ more of the larger systemic arteries may also be lumped, resulting in very simplistic descriptions of the arterial network that were still able to capture the main features of the flow waveform in the middle cerebral artery. For this model, however, errors were magnified when parameters were altered to represent different physiological states, indicating that having a reasonably complete description of the larger arteries is more important than including the nearby system of 1D model arteries.

Blood flow can be measured non-invasively by ultrasound in both the carotid and middle cerebral arteries; however, there are many sources of uncertainty and standard errors of measurements are normally higher than 10% [37]. In comparison, the modelling errors introduced by applying network reduction to obtain simpler descriptions of the arterial system were smaller.

4.2.3. Coronary pressure waveforms

Figure 7 shows the results from applying our methodology on the patient-specific coronary network. The model can be reduced to its most simplistic realization while still keeping the error for the predicted iFR on a level which is comparable with the standard deviation of repeated iFR measurements. The differences in predictions of FFR between baseline and reduced models were even smaller, and in fact smaller than the significant figures used in clinical decision-making. This is attributed to the fact that, unlike iFR, FFR is a cardiac cycle averaged quantity. Our approach for network reduction maintained the correct resistance throughout the domain, and thus also average flow and pressure distributions. The limited resolution of CCTA imaging contributes a layer of uncertainty since only features larger than approximately 1.0 mm can be resolved [38]. However, our results indicate that one should not necessarily strive to segment arteries down to this limit.

5. Concluding remarks

Our results have shown that to capture important features of the aortic pressure waveform, such as timing and shape of reflected waves, pressure augmentation and pulse pressure, a model with all aortic segments, but close to minimal description of the head and lower and upper limb arteries is sufficient. Furthermore, a detailed description of the cerebral circulation is not needed in order to capture physiologically correct waveforms in the common carotid and middle cerebral arteries. Even though our framework for network reduction was performed on a single set of parameters representing a normal physiological state, waveform features were also captured with good qualitative and quantitative precision when the models were re-parametrized to simulate different physiological and pathological states.

Our approach is targeted at computational models of the cardiovascular system, however, it should also be useful for the design of *in vitro* haemodynamic experiments. Such physical models are attractive tools for fundamental research on pulse wave propagation [30,39], and also play a key role in

validating computational models [6]. Through further work, one could also imagine the relevance of our approach in the design of multi-scale models of the cardiovascular system, e.g. hybrid 3D–1D–0D models.

Ethics. All procedures performed in studies involving human participants were in accordance with the ethical standards of the institutional and/or national research committee and with 1964 Helsinki declaration and its later amendments or comparable ethical standards. Informed consent was obtained from all individual participants included in the study.

Data accessibility. The analyses performed in this study were based on the open-source 1D flow solver, STARFiSh (https://www.ntnu.no/starfish). Code and data to reproduce the analyses will be available at https://github.com/Biomechanics-NTNU, shortly. Until then, the files are hosted at the temporary repo https://github.com/Fredf10/starfish_networkReduction_tmp. Raw data in the format produced by STARFiSh, with a size of approximately 130 GB are available upon request.

Authors' contributions. F.-E.F. designed the study, implemented all code, performed all simulations, pre- and post-processing of data and drafted the manuscript. J.M.-H. helped with the development of methods and revisions of the manuscript. J.A. conceived of and coordinated the study and helped with revisions of the manuscript. L.R.H. conceived of and coordinated the study and helped with revisions of the manuscript. All authors gave final approval for publication.

Competing interests. We declare we have no competing interests.

Funding. This work was supported by the British Heart Foundation [PG/15/104/31913 and PG/17/50/32903] and the Wellcome EPSRC Centre for Medical Engineering at King's College London [WT 203148/Z/16/Z]. The views expressed are those of the authors and not necessarily those of the British Heart Foundation, Wellcome Trust or EPSRC.

Acknowledgements. We acknowledge Anders Tjellaug Bråten and Arve Jørgensen who were in charge of collecting and preparing the clinical data used in this study.

Appendix A. Material and methods

A.1. *In vivo* data: measurement and post-processing

Proximal P_p and distal (of a coronary stenosis) P_d pressure tracings were available from a patient with positive findings of coronary artery disease. Pressure tracings were obtained by insertion of a Volcano pressure wire during invasive angiography. P_p and P_d together with a computed (see §A.2.1) left ventricle pressure waveform (grey) are shown in figure 8. CO was measured using transthoracic Doppler echocardiography.

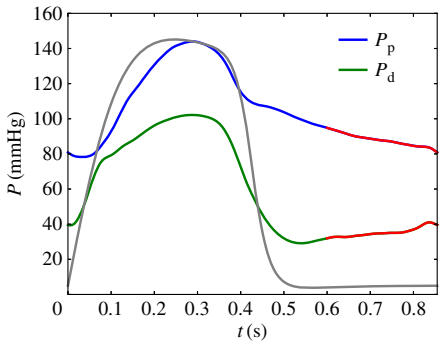

Figure 8. Proximal P_p and distal P_d pressure waveforms obtained during invasive angiography, together with a computed left ventricle pressure waveform in grey. The last 30% of the cardiac cycle is highlighted in red and was used to compute the instantaneous wave-free ratio, iFR, a drug-free index of the significance of the stenosis.

A.2. Numerical formulation

A.2.1. Boundary conditions

The arterial 1D model segments were terminated with WK3 models (systemic arteries) and WK_{cor} models (coronary arteries). In the latter, the influence from the left ventricle pressure, P_{LV} results in a higher coronary impedance in systole. A patient-specific P_{LV} was obtained by coupling a varying elastance (VE) heart model with elastance $E(t)$, volume V and intersect volume V_0:

$$P_{LV} = E(t)(V - V_0), \tag{A 1}$$

with an aortic pressure P_{ao} described by a WK3 model as in [24]. The discrepancy between P_{ao} and P_p was then minimized through parameter estimation. The resulting left ventricle pressure is shown if figure 8. The WK3 and WK_{cor} models, and their coupling with the 1D domain are depicted in figure 9. In the baseline 96-artery model, which only includes systemic arteries, parameters for the outflow WK3 models were adapted from [9]. For the coronary network model, the total arterial resistance and total coronary resistance were estimated by:

$$R_{tot} = \frac{\bar{P}_p - P_{out,WK}}{CO} \quad \text{and} \quad R_{tot,cor} = \frac{\bar{P}_p - P_{out,WK}}{\lambda \times CO}, \tag{A 2}$$

where λ is the fraction of CO supplying coronary arteries, assumed to be 4.5%. The total arterial compliance, C_{tot} was estimated from the VE-WK3 model and total coronary compliance calculated as $C_{tot,cor} = \lambda C_{tot}$. $R_{tot,cor}$ and $C_{tot,cor}$ were further distributed to coronary outlets using Murray's Law [25]. The total resistance for outlet j, $R_{tot,cor,\,j}$ was then divided among R_p, R_m R_d, with fractions 0.01, 0.84, 0.15, respectively, and $C_{tot,cor,j}$ between C_a and C_m with fractions 0.025 and 0.975, respectively.

The estimated coronary resistance given by equation (A 2) assumes zero resistance in the 1D domain. We therefore used the methods described in §2.4.1.1 to estimate mean flow values, and updated $R_{tot,\,cor}$ until total coronary flow reached the target flow of 4.5% of CO.

A.3. Network reduction

A.3.1. Method 1, algebraic estimation of lumped parameters

In figure 10, we have separated the circle of Willis from the rest of the 96-artery model to illustrate how network reduction was performed. Here, the network was truncated at two sites. On the left side of the figure, arrows indicate the direction of the calculated mean flow rate $\bar{Q}$ as described in §2.4.1.1, and defines which arterial segments are distal of a site of truncation.

Once this is known the lumped compliance contribution of these vessels may be calculated. We can estimate the compliance (C_v) of a vessel by integrating over the length of the 1D model segment [13]:

$$C_v = \frac{K_1}{\rho} \quad \text{and} \quad K_1 = \int_0^l \frac{A}{c^2}\,\mathrm{d}x, \tag{A 3}$$

where A and c are evaluated at $\bar{P}$. Furthermore, we can estimate the compliance C_t of a terminal vessel (figure 3)

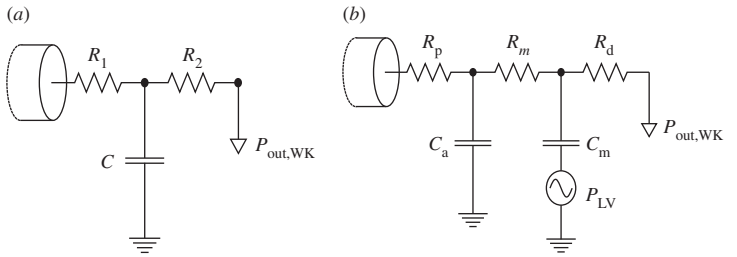

Figure 9. Schematic of the two lumped parameter models used in this work, WK3 model (*a*) and WK_{cor} (*b*). R_1, R_2, R_p, R_m and R_d are resistance parameters, C, C_a and C_m are compliance parameters and P_{LV} and $P_{out,WK}$ are left ventricle and outflow windkessel pressures, respectively.

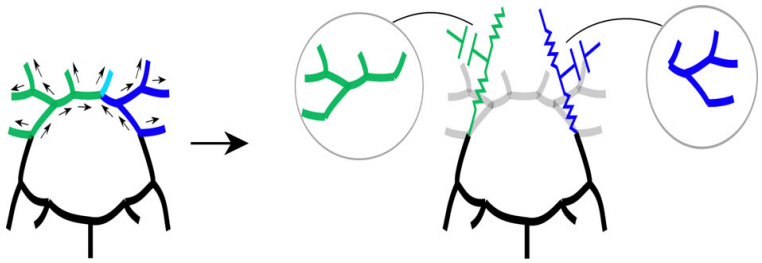

Figure 10. Arrows indicate the direction (not magnitude) of $\bar{Q}$, and also which arteries are lumped into WK3 models for two selected sites of truncation: the left and right internal carotid arteries.

coupled with a WK3 with proximal resistance, R_1, compliance, C and peripheral resistance, R_2 [13]:

$$C_t = \frac{C_v R_2 + C_v R_1 + C R_2 + C_v R_v}{R_2 + R_1 + R_v}. \tag{A 4}$$

Lumped compliance of terminal vessels coupled to WK_{cor} models with compliances C_a and C_m were estimated according to:

$$C_t = C_v + C_a + C_m. \tag{A 5}$$

The compliance contribution of non-terminal vessels was estimated with C_v alone. In order to find the total compliance contribution of the vessels distal of a site of truncation, we use the rules for adding capacitors/compliances in series and parallel. The equivalent compliance ($C_{eq,b}$) of two daughter vessels in a bifurcation and the equivalent compliance ($C_{eq,a}$) of one of the mother vessels and the daughter vessel in an anastomosis is given by (figure 11):

$$C_{eq,b} = C_{d,1} + C_{d,2} \tag{A 6a}$$

and

$$C_{eq,a} = C_{m,1} + \frac{1}{2} C_d, \tag{A 6b}$$

where $C_{d,1}$ and $C_{d,2}$ are the lumped compliances of the two daughter vessels in the bifurcation, C_d is the lumped compliance of the daughter vessel in the anastomosis and $C_{m,1}$ is the lumped compliance of one of the mother vessels in the anastomosis. The compliance contribution of the daughter vessel in an anastomosis is thus split equally between the two mothers.

With the lumped compliance, and estimate of total resistance at a site of truncation as described in §2.4.1.1, the distal arteries may be lumped into *WK* models, as illustrated in figure 12.

A.3.2. Method 2, optimization of lumped parameters

A.3.2.1. Parameter sensitivity, correlation and identifiability

We wanted to assure that the parameters were identifiable, and did so by checking if any of the parameters were highly correlated. The sensitivity of the model output, y to the model parameters, θ can be calculated by the sensitivity matrix [40]:

$$\boldsymbol{S} = \frac{\partial y}{\partial \theta} = \begin{bmatrix} \frac{\partial y}{\partial \theta_1(t_1)} & \cdots & \frac{\partial y}{\partial \theta_m(t_1)} \\ \frac{\partial y}{\partial \theta_1(t_2)} & \cdots & \frac{\partial y}{\partial \theta_m(t_2)} \\ \vdots & \vdots & \vdots \\ \frac{\partial y}{\partial \theta_1(t_n)} & \cdots & \frac{\partial y}{\partial \theta_m(t_n)} \end{bmatrix}, \tag{A 7}$$

in which m is at most 3, $[\theta_1, \theta_2, \theta_3] = [R_1, C, R_2]$, in our case, y is the solution of the WK3 ODE, P_{WK3} and n is the number of time points in one period. The sensitivity matrix, S, was calculated using forward differences. From the sensitivity matrix, we may calculate the model Hessian $\boldsymbol{H} = \boldsymbol{C}^{-1} = \sigma^{-2}\boldsymbol{S}^{\mathrm{T}}\boldsymbol{S}$, where σ is the variance and $\boldsymbol{C}$ is the covariance matrix. The correlation matrix can be calculated as [40]:

$$c_{i,j} = \frac{C_{i,j}}{\sqrt{C_{i,i} C_{j,j}}}. \tag{A 8}$$

If $|c_{i,j}| = 1$, $i \neq j$ then parameters θ_i and θ_j are perfectly correlated. In other words altering θ_i or θ_j has the same effect on y, and hence both of them cannot be identified in the same optimization process. In this work, we have treated two parameters as pairwise correlated if $|c_{i,j}| > 0.86$, and with this criterion we found that in most optimization cases either two or more of R_1, C, R_2 were pairwise correlated. By keeping $R_1 + R_2$ constant and only allowing the relative distribution R_1/R_2 to vary, the subset of parameters, ($[\theta_1, \theta_2] = [R_1/R_2, C]$) was not highly correlated for any of the optimization cases. We therefore used $[R_1/R_2, C]$ as the set of parameters to be

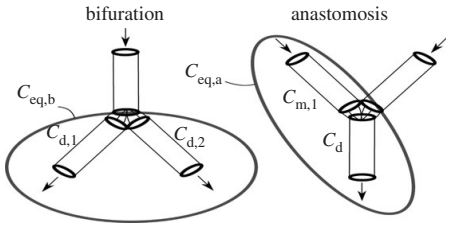

Figure 11. Compliance contribution from vessels in bifurcations and anastomosis used in equation (A6*a*) and equation (A6*b*). Arrows indicate the direction of flow.

optimized in Method 2. Furthermore, if the optimum value of R_1 was less than 0, R_1 was set equal to the characteristic impedance, and only C was optimized.

A.4. Computational aspects

A.4.1. Creation of reduced networks

There are approximately 4.7 million unique networks that can be reduced from the 96-artery baseline model shown in figure 1. Solving all of them was infeasible, however, through some initial tests we managed to reduce the number of possible combinations down to approximately 30000. This was done by replacing branches of vessels that had little effect on the

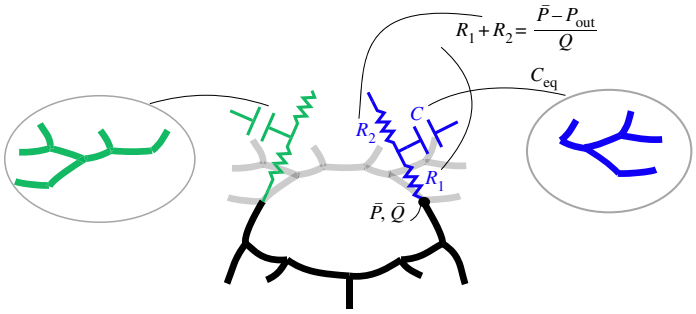

Figure 12. Illustration of vessels distal of points of truncation lumped into WK3 models.

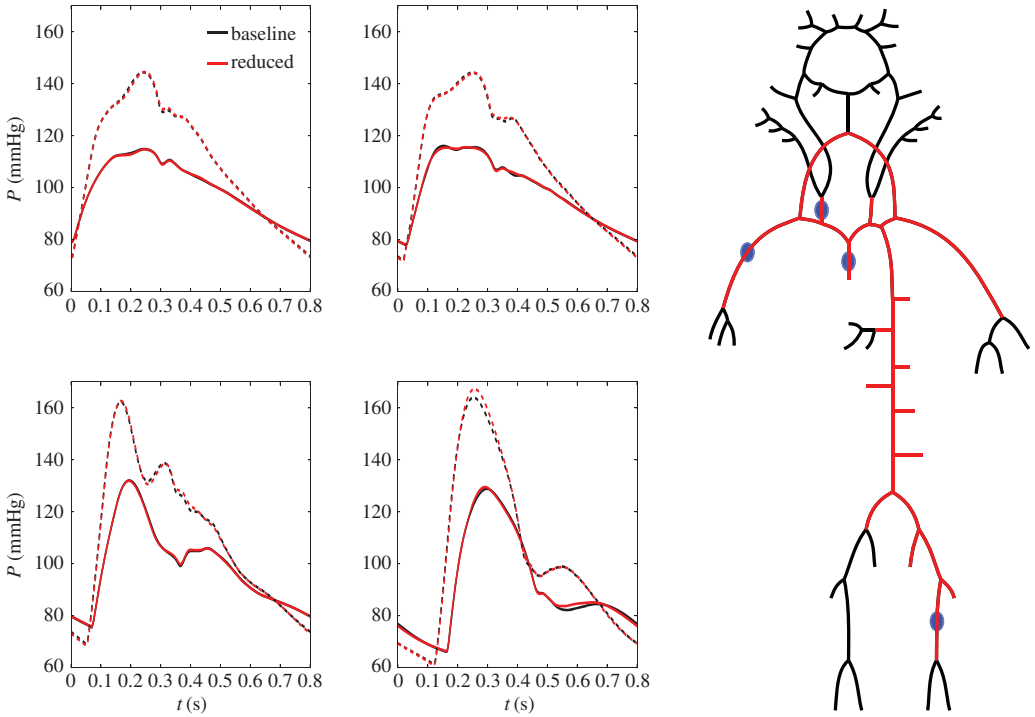

Figure 13. Optimal network obtained from the 96-artery baseline model with pressure at midpoint of ascending aorta (top left), right common carotid artery (top middle), right brachial artery (bottom left) and left femoral artery (middle bottom) set as quantities of interest. The average deviation at these four locations was used as threshold, and set to 0.4% average error. Dashed waveforms represent the case when baseline and reduced networks were re-parametrized to simulate normal ageing (see §2.6).

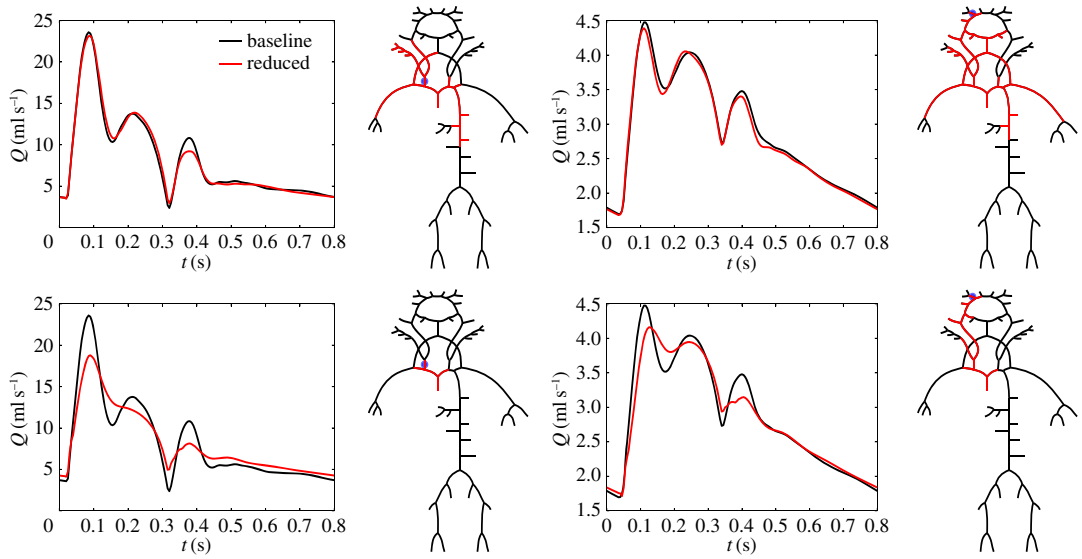

Figure 14. Optimal reduced networks for flow at the distal end of the right carotid artery (left panel) and proximal end of the right middle cerebral artery (right panel). The networks are the same as shown in figure 6; however, parameters were altered in order to represent normal ageing as described in §2.6.

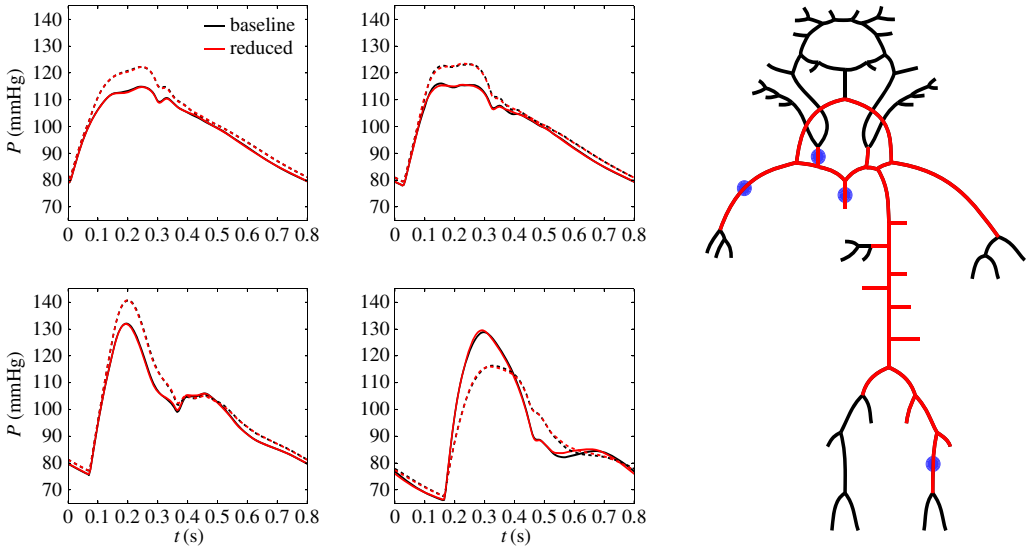

Figure 15. Optimal reduced network for ascending aorta (top left), right common carotid artery (top middle), right brachial artery (bottom left) and left femoral artery (middle bottom). The network is the same as shown in figure 13; however, a pathological state of aortic coarctation (dashed lines) as described in §2.6 is also shown.

pressure and flow waveforms in the arteries of interest ($\epsilon_{Q,avg} < 0.3$ and $\epsilon_{P,avg} < 0.1$).

A.5. Application to different physiological and pathological states

As described in §2.6, total arterial resistance and compliance was altered to represent different physiological states. Here, we describe the details on how this was performed. Departing from the parameters obtained from performing network reduction, total arterial compliance, C_{tot} was calculated as the sum of compliance contribution of 1D segments, $C_{tot,1D}$ and WK3 compliance of terminal vessels, $C_{tot,0D}$ according to

$$C_{tot} = C_{tot,1D} + C_{tot,0D} = \sum_{k=1}^{N_v} C_{v,k} + \sum_{k=1}^{N_t} C_k, \qquad (A\,9)$$

where k is the summation index, N_v is the number of 1D-segments, with compliance $C_{v,k}$ (see equation (A 3)) and N_t is the number of terminal vessels with WK3 compliance, C_k. As mentioned in §2.6, total arterial resistance was modified by altering the peripheral resistance, R_2 in all outflow WK3 models. However, since part of the resistance contribution is due to resistance in the 1D domain, we used the estimated

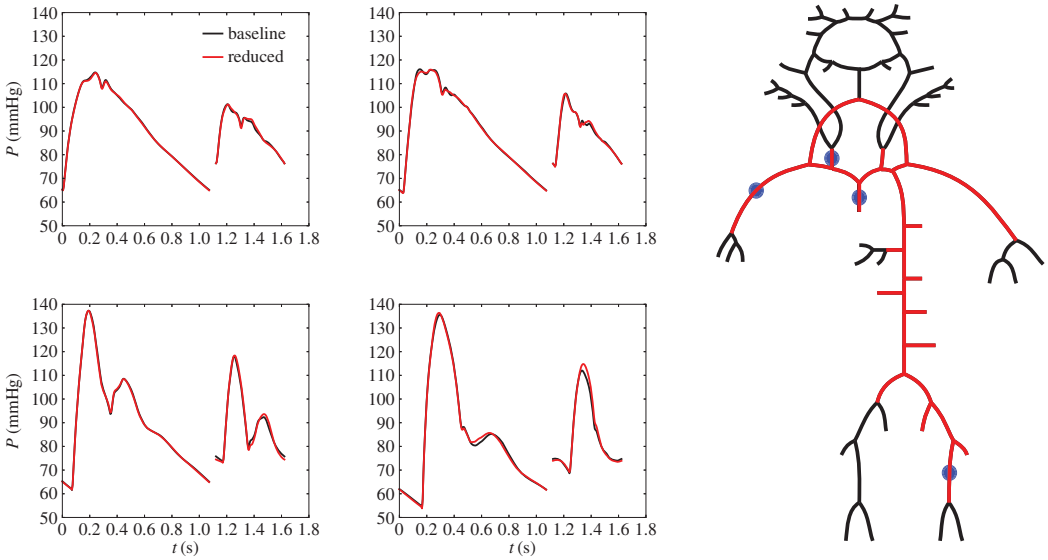

Figure 16. Optimal reduced network for ascending aorta (top left), right common carotid artery (top middle), right brachial artery (bottom left) and left femoral artery (middle bottom). The network is the same as shown in figure 13; however, results are shown for two different inlet waveforms as described in §2.6.

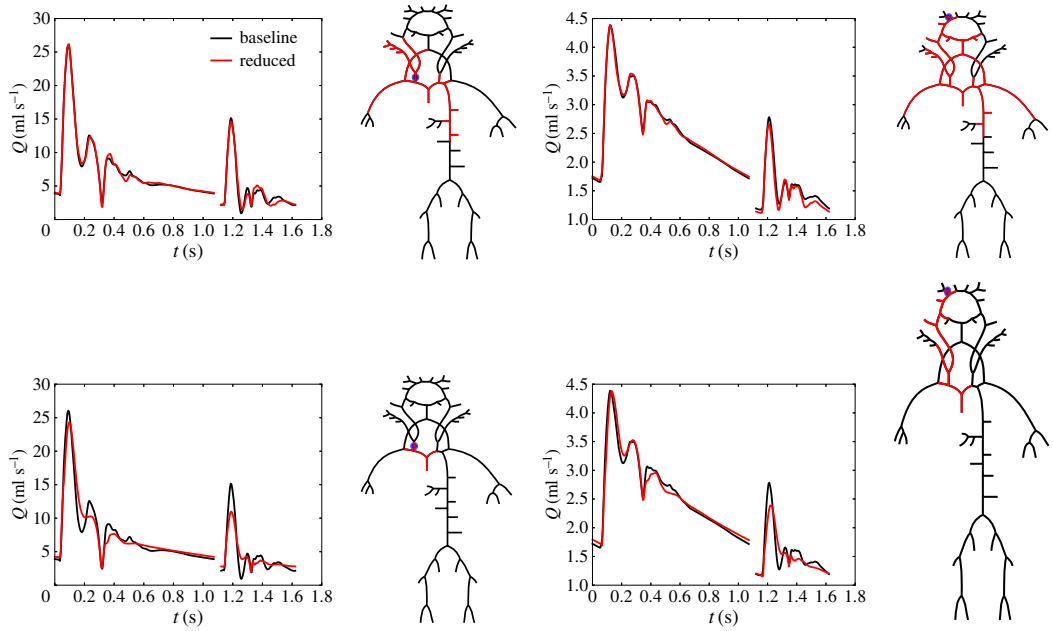

Figure 17. Optimal reduced networks for flow at the distal end of the right carotid artery (left panel) and proximal end of the right middle cerebral artery (right panel). The networks are the same as shown in figure 6; however, results are shown for two different inlet waveforms as described in §2.6.

mean value at the aortic root, $\bar{P}_{\text{inlet}}$ (see §2.4.1) as a surrogate measure of the total arterial resistance. Next, we defined a target inlet pressure, $\bar{P}_{\text{inlet,target}}$ and updated the peripheral resistance, R_2 in all outflow WK3 models according to the expression

$$R_{2,k}^{m+1} + R_{1,k} = \frac{\bar{P}_{\text{inlet,target}}}{(\bar{P}_{\text{inlet}})^m}(R_{2,k}^{m} + R_{1,k}), \qquad \text{(A 10)}$$

where k denotes the relevant outflow segment and m is an iteration index. For the case when normal ageing was simulated, $\bar{P}_{\text{inlet,target}}$ was set to 110 mmHg (i.e. total arterial resistance was increased with a factor of 1.1 since $(\bar{P}_{\text{inlet}})^0$ was 100 mmHg). For inflow case 2, it was necessary to increase total arterial resistance to produce physiological pressure waveforms. Here, $\bar{P}_{\text{inlet,target}}$ was set to 90 mmHg (i.e. total arterial resistance was increased by a factor of 1.67 since $(\bar{P}_{\text{inlet}})^0$ was 54 mmHg). Four iterations were sufficient

to reach $\bar{P}_{\text{inlet,target}}$. In order to decrease total arterial compliance by a factor of 2, we defined a target compliance $C_{\text{tot, target}} = C_{\text{tot}}/2$, and increased the stiffness parameter of proximal arteries by a factor of 2.5 and all others by a factor of 1.5. The following segment Ids were considered as proximal segments; 1, 2, 3, 4, 5, 14, 15, 18, 19, 27, 28 (see the electronic supplementary material). Next, we estimated the compliance contribution of 1D segments after this modification, $C_{\text{tot,1D,mod}}$, and calculated the target WK3 compliance, $C_{\text{tot,0D,target}}$ according to

$$C_{\text{tot,0D,target}} = C_{\text{tot,target}} - C_{\text{tot,1D,mod}}. \tag{A 11}$$

Finally, we updated the individual WK3 compliances according to

$$C_{k,\text{mod}} = C_k \frac{C_{\text{tot,0D,target}}}{C_{\text{tot,0D}}}, \tag{A 12}$$

where $C_{k,\text{mod}}$ is the modified WK3 compliance for terminal segment k.

Appendix B. Results

B.1. Framework for optimizing topological complexity

In order to ensure that interaction between different regions in the network and that pressure propagation was correctly captured throughout the larger systemic arteries, a threshold based on pressure waveforms at four locations was used in figure 13. Here, the average $\epsilon_{P,\text{avg}}$ for the aortic root, right common carotid, right brachial and left femoral artery pressure waveforms was required to be less than 0.4%.

B.2. Application to different physiological and pathological states

Figures 14–17 show the results from the second part of our study, where we re-parametrized a series of optimal networks to represent (1) normal ageing, (2) a pathological state of aortic coarctation and (3) states of different heart rate, ejection time and stroke volume, as described in §2.6. Corresponding error metrics are given in table 1.

References

1. Frank O. 1899 Die grundform des arteriellen pulses: Mathematische Analyse. Erste Abhandlung, Zeitschrift für Biologie.
2. Westerhof N. 1968 Analog studies of human systemic arterial hemodynamics. Dissertations available from ProQuest 1–242.
3. Olufsen MS, Nadim A. 2004 On deriving lumped models for blood flow and pressure in the systemic arteries. *Math. Biosci. Eng.* **1**, 61–80. (doi:10.3934/mbe.2004.1.61)
4. O'Rourke MF. 1967 Pressure and flow waves in systemic arteries and the anatomical design of the arterial system. *J. Appl. Physiol.* **23**, 139–149. (doi:10.1152/jappl.1967.23.2.139)
5. Burattini R, Campbell KB. 1989 Modified asymmetric T-tube model to infer arterial wave reflection at the aortic root. *IEEE Trans. Biomed. Eng.* **36**, 805–814. (doi:10.1109/10.30806)
6. Alastruey J, Khir AW, Matthys KS, Segers P, Sherwin SJ, Verdonck PR, Parker KH, Peiró J. 2011 Pulse wave propagation in a model human arterial network: assessment of 1-D visco-elastic simulations against *in vitro* measurements. *J. Biomech.* **44**, 2250–2258. (doi:10.1016/j.jbiomech.2011.05.041)
7. Sherwin SJ, Franke V, Peiró J, Parker K. 2003 One-dimensional modelling of a vascular network in space–time variables. *J. Eng. Math.* **47**, 217–250. (doi:10.1023/B:ENGI.0000007979.32871.e2)
8. Reymond P, Merenda F, Perren F, Ruifenacht D, Stergiopulos N. 2009 Validation of a one-dimensional model of the systemic arterial tree. *Am. J. Physiol. Heart Circ. Physiol.* **297**, H208–H222. (doi:10.1152/ajpheart.00037.2009)
9. Mynard JP, Smolich JJ. 2015 One-dimensional haemodynamic modeling and wave dynamics in the entire adult circulation. *Ann. Biomed. Eng.* **43**, 1443–1460. (doi:10.1007/s10439-015-1313-8)
10. Blanco PJ, Watanabe SM, Passos MARF, Lemos PA, Feijóo RA. 2015 An anatomically detailed arterial network model for one-dimensional computational hemodynamics. *IEEE Trans. Biomed. Eng.* **62**, 736–753. (doi:10.1109/TBME.2014.2364522)
11. Perdikaris P, Grinberg L, Karniadakis GE. 2015 An effective fractal-tree closure model for simulating blood flow in large arterial networks. *Ann. Biomed. Eng.* **43**, 1432–1442. (doi:10.1007/s10439-014-1221-3)
12. Alastruey J, Parker KH, Peiro J, Sherwin SJ. 2008 Lumped parameter outflow models for 1-D blood flow simulations: effect on pulse waves and parameter estimation. *Commun. Comput. Phys.* **4**, 317–336.
13. Epstein S, Willemet M, Chowienczyk PJ, Alastruey J. 2015 Reducing the number of parameters in 1D arterial blood flow modeling: less is more for patient-specific simulations. *Am. J. Physiol. Heart Cir. Physiol.* **309**, H222–234. (doi:10.1152/ajpheart.00857.2014)
14. Bråten AT, Wiseth R. 2017 Diagnostic accuracy of CT-FFR compared to invasive coronar angiography with fractional flow reserve. See https://clinicaltrials.gov/ct2/show/NCT03045601.
15. Johnson NP *et al.* 2016 Continuum of vasodilator stress from rest to contrast medium to adenosine hyperemia for fractional flow reserve assessment. *JACC Cardiovasc. Interv.* **9**, 757–767. (doi:10.1016/j.jcin.2015.12.273)
16. Yushkevich PA, Piven J, Hazlett HC, Smith RG, Ho S, Gee JC, Gerig G. 2006 User-guided 3D active contour segmentation of anatomical structures: significantly improved efficiency and reliability. *NeuroImage* **31**, 1116–1128. (doi:10.1016/j.neuroimage.2006.01.015)
17. The Vascular Modeling Toolkit. www.vmtk.org, (accessed 27 October 2017).
18. Shahzad R, Kirişli H, Metz C, Tang H, Schaap M, van Vliet L, Niessen W, van Walsum T. 2013 Automatic segmentation, detection and quantification of coronary artery stenoses on CTA. *Int. J. Cardiovas. Imaging* **29**, 1847–1859. (doi:10.1007/s10554-013-0271-1)
19. Hellevik LR *et al.* 2013 STARFiSh: STochastic ARterial Flow Simulations. http://www.ntnu.no/starfish/
20. Hirsch C. 1989 *Numerical computation of internal and external flows, volume 1: fundamentals of numerical discretization*. Brussels, Belgium: Wiley.
21. Liang F, Fukasaku K, Liu H, Takagi S. 2011 A computational model study of the influence of the anatomy of the circle of Willis on cerebral hyperperfusion following carotid artery surgery. *Biomed. Eng. Online* **10**, 84. (doi:10.1186/1475-925X-10-84)
22. Olufsen MS. 1999 Structured tree outflow condition for blood flow in larger systemic arteries. *Am. J. Physiol. Heart Cir. Physiol.* **276**, H257–H268. (doi:10.1152/ajpheart.1999.276.1.h257)
23. Mantero S, Pietrabissa R, Fumero R. 1992 The coronary bed and its role in the cardiovascular system: a review and an introductory single-branch model. *J. Biomed. Eng.* **14**, 109–116. (doi:10.1016/0141-5425(92)90015-D)
24. Stergiopulos N, Meister JJ, Westerhof N. 1996 Determinants of stroke volume and systolic and diastolic aortic pressure. *Am. J. Physiol.* **270**, H2050–H2059. (doi:10.1152/ajpheart.1996.270.6.H2050)
25. Murray CD. 1926 The physiological principle of minimum work: I. The vascular system and the cost of blood volume. *Proc. Natl Acad. Sci. USA* **12**, 207–214. (doi:10.1073/pnas.12.3.207)
26. Uren NG, Melin JA, De Bruyne B, Wijns W, Baudhuin T, Camici PG. 1994 Relation between myocardial blood flow and the severity of coronary-artery

stenosis. *N Engl. J. Med.* **330**, 1782–1788. (doi:10.1056/NEJM199406233302503)

27. Murgo JP, Westerhof N, Giolma JP, Altobelli SA. 1980 Aortic input impedance in normal man: relationship to pressure wave forms. *Circulation* **62**, 105–116. (doi:10.1161/01.cir.62.1.105)
28. O'Rourke MF. 2007 Arterial aging: pathophysiological principles. *Vasc. Med.* **12**, 329–341. (doi:10.1177/1358863X07083392)
29. Weissler AM, Peeler RG, Roehll WH. 1961 Relationships between left ventricular ejection time, stroke volume, and heart rate in normal individuals and patients with cardiovascular disease. *Am. Heart J.* **62**, 367–378. (doi:10.1016/0002-8703(61)90403-3)
30. Segers P, Dubois F, De Wachter D, Verdonck P. 1998 Role and relevancy of a cardiovascular simulator. *J Cardiovas. Eng.* **3**, 48–56.
31. Westerhof N, Lankhaar J-W, Westerhof BE. 2009 The arterial Windkessel. *Med. Biol. Eng. Comput.* **47**, 131–141. (doi:10.1007/s11517-008-0359-2)
32. McEniery CM, McDonnell B Yasmin B, Munnery M, Wallace SM, Rowe CV, Cockcroft JR, Wilkinson IB. 2008 Anglo-Cardiff collaborative trial investigators, central pressure: variability and impact of cardiovascular risk factors: the Anglo-Cardiff collaborative Trial II. *Hypertension (Dallas, Tex.: 1979)* **51**, 1476–1482. (doi:10.1161/HYPERTENSIONAHA.107.105445)
33. Mitchell GF. 2015 Central pressure should not be used in clinical practice. *Artery Res.* **9**, 8–13. (doi:10.1016/j.artres.2014.11.002)
34. Huberts W, Bode AS, Kroon W, Planken RN, Tordoir JHM, van deVosse FN, Bosboom EMH. 2012 A pulse wave propagation model to support decision-making in vascular access planning in the clinic. *Med. Eng. Phys.* **34**, 233–248. (doi:10.1016/j.medengphy.2011.07.015)
35. Karamanoglu M, Gallagher DE, Avolio AP, O'Rourke MF. 1995 Pressure wave propagation in a multibranched model of the human upper limb. *Am. J. Phys. Heart Cir. Phys.* **269**, H1363–H1369. (doi:10.1152/ajpheart.1995.269.4.h1363)
36. Nürnberger J, Keflioglu-Scheiber A, OpazoSaez AM, Wenzel RR, Philipp T, Schäfers RF. 2002 Augmentation index is associated with cardiovascular risk. *J. Hypertens.* **20**, 2407–2414. (doi:10.1097/00004872-200212000-00020)
37. Gill RW. 1985 Measurement of blood flow by ultrasound: accuracy and sources of error. *Ultrasound Med. Biol.* **11**, 625–641. (doi:10.1016/0301-5629(85)90035-3)
38. Kumamaru KK, Hoppel BE, Mather RT, Rybicki FJ. 2010 CT angiography: current technology and clinical use. *Radiol. Clin. North Am.* **48**, 213–235. (doi:10.1016/j.rcl.2010.02.006)
39. Pahlevan NM, Gharib M. 2014 A wave dynamics criterion for optimization of mammalian cardiovascular system. *J. Biomech.* **47**, 1727–1732. (doi:10.1016/j.jbiomech.2014.02.014)
40. Olufsen MS, Ottesen JT. 2013 A practical approach to parameter estimation applied to model predicting heart rate regulation. *J. Math. Biol.* **67**, 39–68. (doi:10.1007/s00285-012-0535-8)

Chapter 7

Uncertainty Quantification and Sensitivity Analysis for Computational FFR Estimation in Stable Coronary Artery Disease

The content of this chapter was published in
Cardiovascular Engineering and Technology, 2018.

Uncertainty Quantification and Sensitivity Analysis for Computational FFR Estimation in Stable Coronary Artery Disease

F.E. Fossan, J. Sturdy, L.O. Müller, A. Strand, A. Bråten, A. Jørgensen, R. Wiseth, L.R. Hellevik

Chapter 8

Impact of baseline coronary flow and its distribution on fractional flow reserve prediction

The content of this chapter was published in
International Journal of Numerical Methods in Biomedical Engineering, 2019.

Impact of baseline coronary flow and its distribution on fractional flow reserve prediction

L.O. Müller, F.E. Fossan, A. Bråten, A. Jørgensen, R. Wiseth, L.R. Hellevik

Received: 1 March 2019 | Revised: 27 June 2019 | Accepted: 25 July 2019

DOI: 10.1002/cnm.3246

SPECIAL ISSUE ARTICLE

WILEY

Impact of baseline coronary flow and its distribution on fractional flow reserve prediction

Lucas O. Müller[1] | Fredrik E. Fossan[1] | Anders T. Bråten[2,4] | Arve Jørgensen[3,4] | Rune Wiseth[2,4] | Leif R. Hellevik[1]

[1] Department of Structural Engineering, Norwegian University of Science and Technology, Trondheim, Norway

[2] Clinic of Cardiology, St. Olavs Hospital, Trondheim, Norway

[3] Department of Radiology and Nuclear Medicine, St. Olavs Hospital, Trondheim, Norway

[4] Department of Circulation and Medical Imaging, Norwegian University of Science and Technology, Trondheim, Norway

Correspondence
Fredrik E. Fossan, Department of Structural Engineering, Norwegian University of Science and Technology, Trondheim, Norway.
Email: fredrik.e.fossan@ntnu.no

Present Address
Frederik E. Fossan, Richard Birkelands, vei 1A,7491 Trondheim, Norway

Abstract

Model-based prediction of fractional flow reserve (FFR) in the context of stable coronary artery disease (CAD) diagnosis requires a number of modelling assumptions. One of these assumptions is the definition of a baseline coronary flow, ie, total coronary flow at rest prior to the administration of drugs needed to perform invasive measurements. Here we explore the impact of several methods available in the literature to estimate and distribute baseline coronary flow on FFR predictions obtained with a reduced-order model. We consider 63 patients with suspected stable CAD, for a total of 105 invasive FFR measurements. First, we improve a reduced-order model with respect to previous results and validate its performance versus results obtained with a 3D model. Next, we assess the impact of a wide range of methods to impose and distribute baseline coronary flow on FFR prediction, which proved to have a significant impact on diagnostic performance. However, none of the proposed methods resulted in a significant improvement of prediction error standard deviation. Finally, we show that intrinsic uncertainties related to stenosis geometry and the effect of hyperemic inducing drugs have to be addressed in order to improve FFR prediction accuracy.

KEYWORDS

coronary flow, fractional flow reserve, reduced-order model

Abbreviations: CAD, coronary artery disease; CCTA, coronary computed tomography angiography; CO, cardiac output; DBP, diastolic blood pressure; DM, distal murray; FFR, fractional flow reserve; HR, heart rateY age; HU, houndsfield units; ICA, invasive coronary angiography; LAD, left anterior descending; LCX, left circumflex; LM, left main; LVM, left ventricle mass; MAP, mean arterial pressure; PCI, percutaneous coronary intervention; PM, proximal murray; PP, pulse pressure; QCA, quantitative coronary angiography; RCA, right coronary artery; RPDA, right posterior descending artery; SBP, systolic blood pressure; SD, stenosis degree; SV, stroke volume; TAG, transluminal attenuation gradient; TMM, total myocardial mass; US, ultrasound; W, weight.

1 | INTRODUCTION

Fractional flow reserve (FFR) is an index to characterise the functional significance of coronary artery stenoses.[1,2] Although FFR is computed as the ratio between invasively measured post-stenotic and central aortic pressures, this index was originally derived to represent the ratio between the actual transtenotic flow over the hypothetical flow that would be observed in the absence of the stenosis under examination.[3] The theoretical derivation of FFR assumes constant peripheral resistance, which in turn is considered to be achieved under maximal vasodilation.[3] As a consequence, FFR is measured in hyperemic conditions, normally caused by the administration of a drug, such as adenosine, that selectively vasodilates the coronary peripheral vasculature.[4] A key advantage of FFR over more conventional methods, such as quantitative coronary angiography (QCA), is that, in addition to taking into account the geometry of a given lesion, it implies considering information about flow (under hyperemic conditions). In fact, after having been tested in large trials,[5-7] FFR is nowadays recommended to guide revascularization strategy in patients with stable coronary artery disease (CAD) without evidence of ischemia in non-invasive testing.[8] In practice, if a lesion is below a certain threshold, $FFR \leq FFR_{threshold}$, with $FFR_{threshold}=0.8$, the recommendation is to intervene by performing percutaneous coronary intervention (PCI) or in some instances bypass surgery, while a negative outcome, ie, $FFR>FFR_{threshold}$, results in treating the patient with optimal medical therapy.[8] Besides the proven validity of FFR as a a tool for functional assessment of stenosis severity, it remains an invasive procedure with associated risks. Moreover, in a study comprising almost 400 000 patients with suspected CAD from 663 US hospitals, almost two-thirds of the patients who underwent elective cardiac catheterisation proved to have non-obstructive CAD as determined by invasive angiography.[9] These considerations have motivated the search for non-invasive tests to reduce the number of invasive procedures. One of the most promising methods so far is coronary computed tomography angiography (CCTA). CCTA is a non-invasive anatomical imaging modality that allows to quantify the geometrical significance of a lesion and has a high diagnostic accuracy when compared with invasive coronary angiography-based diagnosis. A recent randomised trial suggested that CCTA improves patient outcome compared with standard care,[10] and guidelines currently suggest considering CCTA as a first-line test in all patients with suspected stable CAD.[11] CCTA has shown to be very selective in terms of correctly identifying CAD ($FFR \leq FFR_{threshold}$), while its performance to exclude CAD ($FFR>FFR_{threshold}$) is not as satisfactory, resulting in many false positive recommendations, ie, many patients undergo an invasive procedure for FFR measurement that could have been avoided if a more selective non-invasive method would have been used.[12]

In this scenario, CCTA-derived FFR has emerged as a possible response to the need for reducing false positive CCTA recommendations. Over the last decade, a significant number of methods for non-invasive computation of FFR based on CCTA have been proposed.[13] Such methods aim at predicting FFR for a given patient by using non-invasive information only and have already shown potential to be used as a screening tool on top of CCTA assessment.[14] These methods, based on reproducing the fluid mechanics in coronary vessels, share some common general steps that must be followed to deliver FFR predictions: (i) define the computational domain of coronary vessels; (ii) define a mathematical model for fluid mechanics valid in the domain defined in (i); (iii) define boundary conditions; (iv) solve the mathematical model; and (v) evaluate predicted FFR at desired locations. Although such steps can be found in any model-based FFR prediction method, the way in which each of these steps is performed varies greatly. In this paper, we address two aspects of this pipeline. First, we consider steps (ii) and (iv), working on the improvement and validation of a reduced-order model for the coronary circulation that allows for fast and accurate FFR prediction. Then, we focus on step (iii), investigating the impact of several methods for baseline coronary flow estimation and flow distribution proposed so far in the literature on FFR prediction.

Step (ii) of the general modelling strategy defined above requires making a choice on the mathematical model to be used for describing blood flow in coronary arteries. While in principle, many options are available, the most frequent choices found in the literature are 3D incompressible Navier-Stokes in rigid domains and 1D blood flow models in deformable vessels or fully lumped-parameter models. In general, 1D or lumped-parameter models are called reduced-order models. Several reduced-order models for FFR prediction have been proposed previously.[15-19] However, validation by comparison of predicted FFR with respect to results obtained by using more complex models was undertaken only in.[17-19] In Boileau et al,[18] a virtual population constructed from a single patient was used, while in Blanco et al,[17] a population of 20 patients was considered. Here, we modify the method proposed in Fossan et al[19] and validate it on a set of 63 patients (105 FFR measurements). For each patient, we perform simulations using a 3D model for the coronary vessels' domain and use those results as reference. To the best of our knowledge, such an extensive validation of the capacity of a reduced-order model to reproduce fluid mechanical aspects of model-based FFR prediction has not been performed so far.

The definition of boundary conditions for model-based FFR prediction is an unavoidable step. The sensitivity of predicted FFR to these boundary conditions was explored in previous studies[19-21] and was shown to be extremely relevant. In particular, Fossan et al[19] and Morris et al[21] showed that parameters that determine the hyperemic coronary flow have the highest influence on predicted FFR, for realistic ranges of other parameters. Motivated by this fact, we consider two aspects related to the definition of coronary flow, namely, baseline coronary flow and its distribution among the vessels of the network. In fact, virtually all methods for FFR prediction proposed so far require a baseline flow to be imposed and a criterion to distribute it among vessels in the network. Here, we have selected a set of representative methods for the definition of baseline coronary flow from published works, as well as three alternative methods to distribute such flow among coronary vessels, in order to assess the impact of these modelling choices on FFR prediction. Finally, we perform a sensitivity analysis where we compare the influence of baseline coronary flow to other parameters that are known to be important, namely, the stenosis geometry and the reduction in coronary peripheral resistance from baseline to hyperemic conditions.

The rest of this paper is structured as follows. In Section 2, we describe the acquisition of patient-specific data (Section 2.1), a reduced-order model for FFR prediction (Section 2.2), the 3D modelling framework used for validation purposes (Section 2.3), the overall modelling strategy for FFR prediction (Section 2.4), several methods to determine baseline coronary flow (Section 2.5) and its distribution among coronary vessels (Section 2.6), and the method by which a sensitivity analysis of predicted FFR to relevant model parameters was performed (Section 2.7). Section 3 provides a summary of main characteristics of patients involved in the study (Section 3.1), results on the validation of the reduced-order model (Section 3.2), and results on the impact of explored modelling strategies on FFR prediction (Section 3.3). Finally, Section 4 includes a detailed analysis of reported results, as well as considerations on the study limitations and the steps to be taken to (a) improve the reduced-order model description to better capture the fluid mechanical aspects of the problem under consideration and (b) reduce uncertainty in FFR predictions.

2 | METHODS

2.1 | Patients and data acquisition

2.1.1 | Recruitment

Patients were recruited as part of an ongoing clinical trial at St. Olavs hospital, Trondheim, Norway.[22] Patients included in this study had undergone CCTA because of chest pain and suspicion of stable CAD. Patients were enrolled with the findings of at least one coronary stenosis at CCTA examination and were further referred to invasive coronary angiography (ICA) with invasive FFR measurements. Exclusion criteria included nondiagnostic quality of the CCTA, previous percutaneous coronary intervention or bypass surgery, contraindications to adenosine, age (75 years or older), obesity (body mass index greater than 40), and hospitalisation due to unstable CAD after CCTA.

2.1.2 | Medical data acquisition

CCTA

CCTA was performed using 2×128 detector row scanners (Siemens dual source Definition Flash) and 256 detector row CT scanners (Revolution CT, GE Healthcare, Waukesha, Wisconsin, US) with a standardised protocol.[23] Left ventricle mass (LVM) was quantified using a commercial software (Syngo.via, Siemens, Germany).

Ultrasound

Echocardiographic imaging was performed using a GE Vivid E95 scanner (GE Vingmed Ultrasound, Horten, Norway). Cardiac output (CO) was calculated on the basis of the cross-sectional area of the left ventricle outflow tract (measured immediately proximal to the points of insertion of the aortic leaflets) and velocity time integral derived from PW Doppler.

Fractional flow reserve

FFR was measured using Verrata Plus (Philips Volcano, San Diego, USA) pressure wires according to standard practice. Intra-coronary nitroglycerine (0.2 mg) was given to all patients before advancing the pressure wire into the coronary arteries, and hyperemia was induced by continuous intravenous infusion of adenosine at a rate of at least 140μg/kg/min. Pressure was measured over several cardiac cycles, and FFR measurements were taken during the nadir (lowest

observed value). After measurement, the interventional cardiologist removed the pressure wire back to the equalisation point at the tip of the guiding catheter to ensure that there was no drift. Invasive pressure tracings were recorded and made available for further processing.

Clinical data

Standard non-invasive diastolic/systolic pressure measurements were performed on both arms as part of clinical routine before ICA using an automatic, digital blood pressure device, Welch Allyn ProBP 3400.

2.2 | Reduced-order model

Here, we briefly describe the methodology presented in Fossan et al[19] for the computation of FFR using a reduced-order model. FFR predictions obtained with the exact setting proposed in Fossan et al[19] will be denoted as FFR_{RO^*}, while predictions obtained using the improved version of the reduced-order model introduced in this section will be denoted as FFR_{RO^*}. This is valid throughout the rest of the paper unless otherwise specified.

2.2.1 | Vessels segmentation and computational domain meshing

Segmentation of coronary vessels is performed using the open-source software ITK-SNAP. [24] The output of ITK-SNAP is a labelled voxel volume identifying segmented vessels and a surface mesh of the segmented volume (in VTK format). Coronary arteries are segmented until their presence is not distinguishable from surrounding tissue. With this, the resulting average (±standard deviation) outlet radius of coronary arteries included in the computational domain is 0.9±0.23 mm. Surface mesh processing, addition of flow extensions, and 3D meshing are performed using the open-source library Vascular Modeling ToolKit (VMTK).[25,26] The 3D volume meshes form the basis for both the reference 3D model and the reduced-order model. For the latter, centerlines are extracted from 3D domains using a centerline extraction algorithm available in VMTK.

2.2.2 | Domain definition

The resulting network of centerlines obtained by the processing steps briefly illustrated in Section 2.2.1 can be conceptually described as a directed graph $G = (V, E)$, where

- V are the vertices of the graph, which in this application can represent junctions/bifurcations, a root node, and terminal nodes of the network, hereafter called outlets.
- E is a set of ordered pairs of vertices, in this case representing vessels.

Graph G will have M edges (or vessels) and N vertices. v_{root} is the vertex at the root of the network, while v^j_{out}, $j = 1, \ ..., N_{out}$, are outlets and v^j_b, $j = 0, \ ..., N_b$, are vertices representing coupling points among vessels, see Figure 1. Vessel e_j is described by a set of K^j nodes produced by the centerline extraction algorithm cited in Section 2.2.1. Each node k^j_l, $l = 1, \ ..., |K^j|$, is marked as belonging to a bifurcation region ($K^j_b \in K^j$), belonging to a stenosis ($K^j_s \in K^j$), or belonging to a 1D domain ($K^j_{1D} \in K^j$). The masking of such regions is explained in detail in Fossan et al.[19]

Here, we modify the domain definition reported in Fossan et al[19] as follows:

- the spacing between nodes k is reduced from 0.5mm to 0.125mm;
- an additional criteria for masking stenotic regions on the basis of the gradient of the radius in the longitudinal direction is added. In Fossan et al,[19] a detected stenosis was marked until the estimated stenosis degree (SD) was below 12%. Here, we require that $SD > 12\% \vee |\frac{dr}{dx}| < 0.05$. In practice, even though the estimated stenosis degree is below 12%, we continue to mark the region as a stenosis if the location represents a compression $\frac{dr}{dx} < 0.05$ or an expansion $\frac{dr}{dx} > 0.05$.

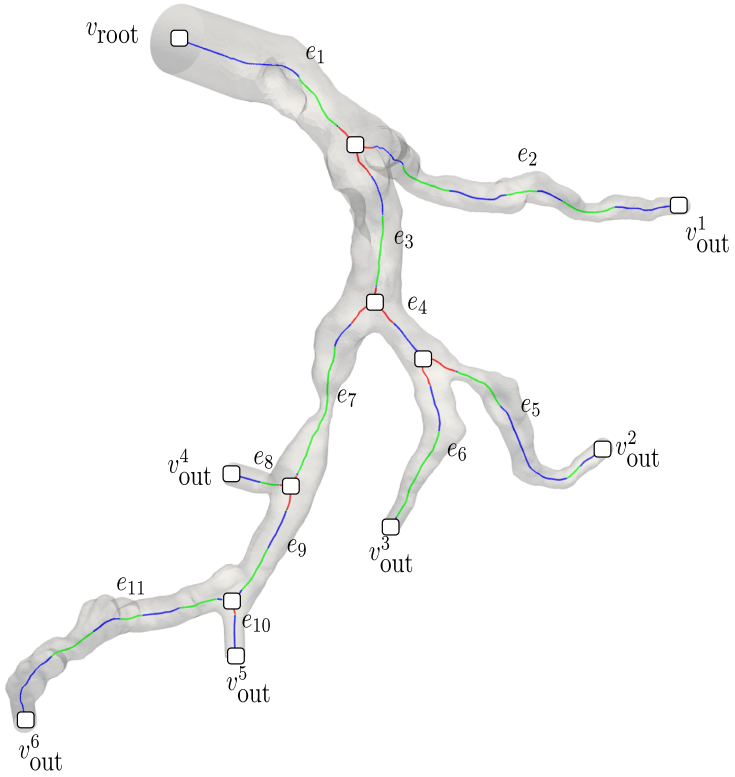

FIGURE 1 Centerline extracted from one subject of the study population. Graph G structure is shown with white rectangles representing vertices. In particular, root, outlet vertices, and edges are evidenced. Edges' regions marked as bifurcation areas are shown in red, stenotic areas are shown in green, and 1D domains are shown in blue. The original 3D segmentation from which centerlines are extracted is shown as a transparent surface

2.2.3 | Mathematical models

Let us consider a single vessel e_j. In regions of e_j labelled as 1D domain, ie, $K^j_{1D} \in K^j$, blood flow is modelled according to a 1D steady state blood flow model, ie,

$$\frac{\partial Q}{\partial x} = 0, \tag{1a}$$

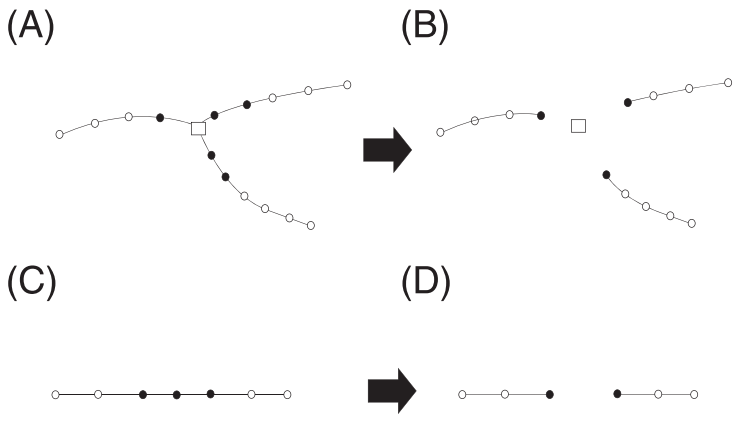

FIGURE 2 A, Vessels at a bifurcation (graph vertex depicted as a hollow square) with corresponding nodes (circles), nodes masked as belonging to the bifurcation region depicted as filled circles. B, Bifurcation region, nodes are collapsed into one node per vessel (filled circles), at which vessels are coupled using (2b). C, Single vessel with corresponding nodes (circles), nodes masked as belonging to a stenotic region are depicted as filled circles. D, Vessel is split into two vessels, stenosis region nodes collapsed into one node per vessel (filled circles), at which the resulting vessels are coupled using (2b) and (3)

$$\frac{\partial}{\partial x}\left(\frac{Q^2}{A}\right) = -\frac{A\partial P}{\rho\,\partial x} + \frac{-2(\zeta+2)\mu\pi Q}{\rho \quad A}, \tag{1b}$$

where A is the cross-sectional area of the vessel, Q is the blood flow rate, and P is the blood pressure. Moreover, ζ=4.31,[19] ρ=1.05g/cm^3 is the blood density, and μ=0.035 dyne/cm^{2}s is the blood viscosity. The cross-sectional area A is assumed constant in time and equal to the area obtained from the segmentation of medical images. Then, the problem unknowns are pressure P and flow rate Q.

Regions masked as bifurcations and stenoses are not modelled using a continuous model. Nodes belonging to such regions are collapsed into a single point, and coupling conditions apply. See Figure 2 for a graphical illustration of this aspect. Coupling for both connection types (bifurcations and stenoses) is performed by enforcing the following relations at the coupling point

$$\sum_{i=1}^{T} Q_i = 0, \tag{2a}$$

$$P_1 + \lambda\frac{\rho}{2}U_1^2 = P_i + \lambda\frac{\rho}{2}U_i^2 + \Delta P_i \quad i = 2,\ \ldots,\ T, \tag{2b}$$

where T is the number of vessels sharing a vertex with the bifurcation/stenosis. For stenoses, we have that T=2, while in the case of bifurcations, we have $T \geq 2$. ΔP is an additional pressure loss, and λ is a coefficient that can assume values between zero and one. At bifurcations, ΔP is set to zero and λ is set to one, so that Equation (2a) describes continuity of total pressure. At coupling points representing stenoses, we set λ=0, and ΔP is computed as proposed in Seeley and Young,[27] namely

$$\Delta P = \frac{K_v\mu}{A_0 D_0}Q + \frac{K_t\rho}{2A_0^2}\left(\frac{A_0}{A_s}-1\right)^2 Q|Q|, \tag{3}$$

where A_0 and A_s refer to cross-sectional areas of the normal and stenotic segments, respectively. Similarly, D_0 and D_s represent the normal and stenotic diameters. Furthermore, K_v and K_t are empirical coefficients, with $K_v = 32(0.83L_s + 1.64D_s)\cdot(A_0/A_s)^2/D_0$, K_t=1.52,[27] whereas L_s is the length of the stenosis.

2.2.4 | Boundary conditions

In this work, we consider two alternative sets of outlet boundary conditions: prescribed flow rate at outlets or resistive elements coupled to outlets. See Section 2.4 for motivation on the two different setups introduced here.

Prescribed flow rates at outlets

Pressure is prescribed at v_{root}, namely $P_{\text{root}} = \hat{P}_{\text{root}}$, where $\hat{P}_{\text{root}}$ is the prescribed pressure. Then, we set $Q^j_{\text{out}} = \hat{Q}^j,\ j = 1,\ \ldots,\ N_{\text{out}}$, where $\hat{Q}^j,\ j = 1,\ \ldots,\ N_{\text{out}}$, are the flows to be prescribed deriving from methods described in Sections 2.5 and 2.6. Defining flow rate at outlets implies that flow rate over the entire network is fixed. Then, the only remaining unknown is pressure along 1D domains, and pressure drops over stenotic regions. Such pressure is obtained integrating (1) for Q given along the 1D domains and evaluating coupling relations (2b) and (3) where appropriate. A reasonable strategy is to start at v_{root} and traverse the entire tree, but other choices are possible.

Resistive elements coupled to outlets

As in the previous case, pressure is prescribed at v_{root}, namely $P_{\text{root}} = \hat{P}_{\text{root}}$. Then, we consider resistive elements coupled to outlets with resistances $R^j_{\text{out}},\ j = 1,\ \ldots,\ N_{\text{out}}$. In this case, flow rate is unknown over the entire network, and a nonlinear algebraic system has to be solved to find the flow rates at outlets $Q^j_{\text{out}},\ j = 1,\ \ldots,\ N_{\text{out}}$, which solve (1), (2b), (3), and $P_{\text{root}} - \hat{P}_{\text{root}} = 0$. More details on the numerical treatment of the modelling setup strategies presented here are given in Fossan et al.[19]

2.3 | 3D modelling

3D simulations are used to validate the reduced-order model proposed in Fossan et al[19] and improved in this work. These simulations are performed considering segmented coronary trees as rigid domains with a prescribed pressure as inlet boundary condition and either prescribed flows (via prescribed parabolic velocity profile) or lumped-parameter models attached to each network outlet, according to the modelling pipeline described in Section 2.4. Furthermore, the flow is assumed laminar, and blood is modelled as an incompressible Newtonian fluid. The open-source library CBCFLOW,[28] based on FEniCS[29] is used to solve the resulting mathematical model. The incompressible Navier-Stokes equations are solved using the incremental pressure correction scheme, described in Simo and Armero.[30] Tetrahedral elements compose the computational mesh where the velocity field is approximated using piecewise-quadratic polynomials, while linear polynomials are used for pressure. The solver implementation follows very closely the one reported in Mortensen and Valen-Sendstad.[31] 3D meshes were constructed using the open-source library VMTK.[25,26] The meshing refinement level was determined by a meshing algorithm parameter called edge-length factor l_f, which was set to l_f=0.21 for all simulations. A mesh independence study showed that such discretisation provides mesh-independent FFR predictions for a set of four patient-specific geometries. A full description of the underlying mathematical models and their numerical treatment is provided in Fossan et al[19] and references cited therein.

2.4 | Overall modelling strategy

FFR is normally measured at one or more points in the coronary tree. In the current computational context, we simulate a hyperemic state for the entire coronary tree. Therefore, we refer to a hyperemic state as the condition under which virtual FFR measurements are performed. Assuming that a network of coronary branches for a given patient with related parameters is available (see Section 2.2), we proceed as follows in order to obtain a hyperemic state:

1. define total baseline coronary flow by one of the methods described in Section 2.5: q;
2. distribute flows among the network's N_{out} outlets according to one of the methods described in Section 2.6: $Q_{\text{out},l}$, with l=1,...,N_{out};
3. perform a simulation with prescribed inlet pressure P_{root}=P_{proximal} and prescribed outlet flows defined in previous step to find $P^{\text{bln}}_{\text{out},l}$, with $l = 1,\ \ldots, N_{\text{out}}$;
4. compute resistances at outlets as
$$R^{\text{bln}}_{\text{out},l} = \frac{P^{\text{bln}}_{\text{out},l} - P_v}{Q^{\text{bln}}_{\text{out},l}}, \text{ with } l = 1,\ \ldots, N_{\text{out}}, \tag{4}$$
where $P^{\text{bln}}_{\text{out},l}$ is the pressure at the l-th outlet resulting from the simulation performed in previous step and P_v is a reference venous pressure, which is set to P_v=5 mmHg throughout this work;
5. perform a simulation with prescribed inlet pressure P_{root}=P_{proximal} and prescribed resistances at outlets. Such resistances are computed as
$$R^{\text{hyp}}_{\text{out},l} = \frac{R^{\text{bln}}_{\text{out},l}}{\text{TCRI}}, \text{ with } \ l = 1,\ \ldots, N_{\text{out}}, \tag{5}$$
where TCRI is the so-called total coronary resistance index, ie, the factor by which peripheral coronary resistance drops from its value at baseline conditions to its value in hyperemia. In this work we use TCRI=4, unless otherwise stated.[4]

TABLE 1 Parameters needed to run a simulation using pipeline described in Section 2.4

Parameter/Data	Symbol	Source/Equation/Table
Coronary tree centerlines with radii	-	post-processed CCTA-derived segmentation
Pressure at inlet	P_{proximal}	Clinical non-invasive measurement
Baseline flow	q	Table 3
Branch split	-	Table 4 or coupled branches (see Section 2.6)
Total coronary resistance index	TCRI	TCRI=4, as in Wilson et al[4]

[a]Abbreviation: CCTA, coronary computed tomography angiography.

Simulation results from point 5 of the previous list represent the hyperemic state from which FFR can be evaluated at any point of the network as

$$\mathrm{FFR}^{j}_{\mathrm{RO}} = \frac{P_j}{P_{\mathrm{proximal}}}, \tag{6}$$

where P_j is the predicted pressure at the jth node of the network. We remind the reader about the fact that if predictions are obtained with the setting proposed in Fossan et al,[19] ie, without the modifications introduced in Section 2.2.2, then those predictions will be denoted as $\mathrm{FFR}_{\mathrm{RO}^*}$. Table 1 summarises necessary data and parameters for prediction of FFR with the reduced order model.

2.5 | Methods for baseline coronary flow estimation

In this work, we explore a number of methods to estimate baseline coronary flow, q. In selecting the methods to be used, we sought to include methods that use different types of data. In particular, we included methods that rely on CO estimation, as well as methods that use LVM and a method based on population studies. A description of such methods follows.

2.5.1 | CO-based methods for baseline coronary flow estimation

We consider two alternative methods to determine CO. The first method consists of simply using the CO derived from patient-specific ultrasound (US) measurements acquired as explained in Section 2.1.2. CO derived from US measurements will be called $\mathrm{CO}_{\mathrm{US}}$ hereafter. The second method uses a formula to estimate stroke volume from patient-specific parameters.[32] Such formula, originally proposed in de Simone et al,[33] is given as

$$\mathrm{SV} = \mathrm{PP}^{*} \times [(0.013 \times \mathrm{W}) - (0.007 \times \mathrm{Y}) - (0.004 \times \mathrm{HR}) + 1.307], \tag{7}$$

where W is weight in kilograms, Y is age in years, and HR is heart rate in beats per minute. Moreover, PP^{*} is

$$\mathrm{PP}^{*} = (0.49 \times \mathrm{PP}) + (0.3 \times \mathrm{Y}) + 7.11, \tag{8}$$

where PP is pulse pressure, PP=SBP−DBP, with SBP and DBP being systolic and diastolic blood pressure (in mmHg), respectively. Then, CO is computed as

$$\mathrm{CO}_{\mathrm{DeSimone}} = \mathrm{HR} \times \mathrm{SV}. \tag{9}$$

Once CO is estimated by either of the two methods, we compute baseline coronary flow as

$$q^{\mathrm{X}}_{\mathrm{Guyton}} = \gamma \mathrm{CO}_{\mathrm{X}}, \tag{10}$$

where γ=0.045 is the fraction of CO that flows into the coronary branches,[34] and X={US,DeSimone} are the two considered CO estimation methods.

2.5.2 | LVM-based methods for baseline coronary flow estimation

Alternatively to the use of CO to determine total baseline coronary flow q, several investigators have used LVM to perform such estimate. Here, we select two methods and propose modifications to them. In Kishi et al,[35] q is computed as

$$q_{\mathrm{Kishi}} = \beta \times \mathrm{TMM}, \tag{11}$$

where β=0.8 mL/min/g is a reference value for myocardial tissue perfusion,[36] and TMM stands for total myocardial mass, computed as

TABLE 2 Baseline coronary flows from Sakamoto et al[40]

Branch	Symbol	Flow, mL/min (Right-dominant)	Flow, mL/min (Left-dominant)
Left branch	$q_{\text{Sakamoto}}^{\text{LB}}$	156.58	209.27
Right branch	$q\text{Sakamoto}^{\text{RB}}$	113.42	57.73
Total	q_{Sakamoto}	270.00	267.00

$$\text{TMM} = \frac{3}{2} \times \text{LVM}. \tag{12}$$

It is worth noting that no other patient-specific information than LVM is used. A method that accounts for additional patient-specific information is the one used for FFR prediction in Sharma et al.[37] In this case, the observed association between the product SBP×HR is considered in the computation of baseline flow, which reads

$$q_{\text{Sharma}} = (0.08 \times (0.7 \times \text{HR} \times \text{SBP} \times 0.001 - 0.4)) \times \text{TMM}, \tag{13}$$

where TMM is computed with (12). Since, as it will be shown later in Section 3.1, Table 2, baseline coronary flows computed using (11) and (13) are very low compared with reference values, we propose to modify both methods. The reason for the underestimation of baseline coronary flow in these cases is related to the rather low TMM derived from the hypothesis stated in (12). In both modified methods, we use

$$\text{TMM}_{\text{Molina}} = 2.4 \times LVM. \tag{14}$$

The constant value 2.4 was determined by considering that the ratio of reference TMM reported in Molina and DiMaio[38,39] over LVM for patients included in this study (2.39 (0.34) and 2.34 (0.42) for men and women, respectively). Moreover, in the case of q_{Sharma}, the constant 0.08 was replaced by 0.14 in order to force average flow over the population to be in accordance with reference values.[40] See Table 2 for details. Modified baseline flow estimates are denoted as $\widehat{q}_{\text{Kishi}}$ and $\widehat{q}_{\text{Sharma}}$ for q_{Kishi} and q_{Sharma}, respectively.

2.5.3 | Population-based methods for baseline flow estimation

Here, we simply specify flows to left and right coronary branches as specified in Sakamoto et al. [40] Average flows are differentiated according to the dominance of the coronary vasculature. Table 2 summarises the different values for total coronary flow, as well as for left and right branches.

Table 3 summarises the different methods used to determine coronary flow and how they are computed.

TABLE 3 Summary of baseline coronary flow estimation methods

Method	Data	Equations
$q_{\text{Guyton}}^{\text{US}}$	CO_{US}	(10)
$q_{\text{Guyton}}^{\text{DeSimone}}$	W, Y, HR, SBP, DBP	(10)
q_{Kishi}	LVM	(11), (12)
$\widehat{q}_{\text{Kishi}}$	LVM	(11), (14)
q_{Sharma}	LVM, HR, SBP	(13), (12)
$\widehat{q}_{\text{Sharma}}$	LVM, HR, SBP	(13)-mod, (14)
q_{Sakamoto}	Table 2	-

Note. All data used was acquired non-invasively in ambulatory conditions unless otherwise stated.

Abbreviation: CO, cardiac output; DBP, diastolic blood pressure; HR, heart rate; LVM, left ventricle mass; SBP, systolic blood pressure; US, ultrasound; W, weight (in kilograms); Y, age (in years).

2.6 | Flow distribution

There is a variety of methods used in the literature to distribute baseline coronary flow among the coronary vessels. A major difference is given by the fact that some practitioners model a single branch (left or right), while others consider both branches simultaneously. In order to account for this aspect, we have applied the methods described below in two different settings, namely, applying the methods on single branches or on both coupled branches.

2.6.1 | Distal Murray

Murray's law[41] is the most commonly used method to distribute coronary flow; see previous studies[37,42] for example. It expresses a proportionality between flow and vessel diameter

$$Q \propto d^{\xi}, \tag{15}$$

with ξ=3 from theoretical considerations on minimum work. Distal Murray (DM) flow distribution implies that for a given network with N_{out} outlets, flow is distributed among all outlets using (15) and outlets' diameters.

2.6.2 | Proximal Murray

In this case, one traverses a given network from its root, and flow is split at each bifurcation applying (15) among daughter vessels. The diameter used here was taken as the average vessel diameter, computed over vessel nodes that were not marked as belonging to stenoses or bifurcation areas. See Section 2.2 for an explanation and further references on how these nodes are marked. This method was used in previous studies,[35,43] in the context of FFR prediction.

2.6.3 | Transluminal Attenuation Gradient

Here, we implement the method proposed in Kishi et al,[35] where authors hypothesise an inverse relation between flow and transluminal attenuation gradient (TAG), ie, $Q \propto -1/\text{TAG}$. The interesting feature of this approach is that it uses information on flow distribution properties of a given patient by directly looking into how contrast is advected in the coronary tree during CCTA acquisition. TAG is essentially the gradient of voxel intensities, quantified as Hounsfield Units (HU) in the CCTA image averaged along a given vessel. TAG is computed for each terminal point of the vessel network by computing HU along centerline nodes and fitting a first-order polynomial to the resulting data points (arc-length versus HU: $\text{HU}(x)=\text{HU}_0+\text{TAG}\cdot x$, with x the centerline arc-length). Intensities along the path are computed by averaging CCTA voxel intensities around each centerline node. Candidate voxels are those in a volume of 5×5×5 voxels centred at a given centerline node. In order to be included, a candidate voxel has to fall within the segmented vessel lumen and has to have a HU value that is below a threshold in order to exclude calcifications and artefacts. Such threshold is set equal to the average plus two standard deviations of HU values for all voxels contained in the segmented lumen volume. For a detailed definition of TAG and its computation in coronary trees; see Kishi et al[35] and references cited therein. TAG is computed for each patient considered in this study using CCTA images, segmented vessels lumen volume, and extracted centerlines.

2.6.4 | Branch flow split for single branch distribution

In the case in which a single coronary branch is considered for simulation, a further assumption is necessary since we depart from total baseline coronary flow, and a branch-specific flow is needed. Two strategies are followed. One strategy consists of splitting flow between left and right branches as observed in Sakamoto et al[40] and reported in Table 4. The second one regards simply imposing average coronary flows to left and right branches, specified in Table 2.

TABLE 4 Baseline coronary flow splits derived from Sakamoto et al[40]

Branch	Right-Dominant Percentage of Total Flow	Left-Dominant Percentage of Total Flow
Left branch	58.00	78.38
Right branch	42.00	21.62

TABLE 5 Summary of baseline coronary flow estimation and split methods

Branch Treatment	Baseline Flow	Branch Split	Flow Distribution
Single branch	$q^{\mathrm{US}}_{\mathrm{Guyton}}$	Table 4	DM/PM/TAG
	$q^{\mathrm{DeSimone}}_{\mathrm{Guyton}}$	Table 4	DM/PM/TAG
	$\bar{q}^{\mathrm{US}}_{\mathrm{Guyton}}$	Table 4	DM/PM/TAG
	q_{Kishi}	Table 4	DM/PM/TAG
	$\hat{q}_{\mathrm{Kishi}}$	Table 4	DM/PM/TAG
	q_{Sharma}	Table 4	DM/PM/TAG
	$\hat{q}_{\mathrm{Sharma}}$	Table 4	DM/PM/TAG
	q_{Sakamoto}	Table 2, first and second rows	DM/PM/TAG
Coupled branches	$q^{\mathrm{US}}_{\mathrm{Guyton}}$	-	DM/PM/TAG
	$q^{\mathrm{DeSimone}}_{\mathrm{Guyton}}$	-	DM/PM/TAG
	$\bar{q}^{\mathrm{US}}_{\mathrm{Guyton}}$	-	DM/PM/TAG
	q_{Kishi}	-	DM/PM/TAG
	$\hat{q}_{\mathrm{Kishi}}$	-	DM/PM/TAG
	q_{Sharma}	-	DM/PM/TAG
	$\hat{q}_{\mathrm{Sharma}}$	-	DM/PM/TAG
	q_{Sakamoto}	Table 2, third row	DM/PM/TAG

Abbreviation: DM, distal Murray; PM, proximal Murray; TAG, transluminal attenuation gradient.

Having defined the three flow distribution strategies that will be explored in this work, we can define a set of simulation settings that will be used for each of the baseline flow estimation methods described in Section 2.5 and summarised in Table 3. In fact, for each one of those baseline flows, we have Y_{Z} flow splits, with Y={PM,DM,TAG} and Z={S,C}. S and C correspond to cases where flow distribution is applied to single and coupled branches, respectively. Table 5, together with Table 3, provides the reader with a complete overview of all modelling assumption combinations used in this study, so that the equations and parameters used for a specific simulation setup can be easily retrieved.

2.7 | Sensitivity analysis

We conduct uncertainty quantification and sensitivity analysis (UQ&SA) to rank the influence of uncertain input parameters on FFR prediction. In Fossan et al,[19] a wide range of parameters were analysed in terms of UQ&SA; however, the most influential parameters were those related to coronary flow, TCRI, and minimum stenotic radius. Other input parameters such as P_{proximal}, Murray coefficient, and rheological parameters (ρ, μ) were less influential. On the basis of these considerations, we perform a sensitivity analysis on the uncertain input parameters q, TCRI, and SD, with the uncertainty in SD affecting the minimum radius. q was modelled as a (truncated at ± 3 std) normal distribution with a mean and standard deviation deriving from the per patient mean and standard deviation obtained with four of the patient-specific baseline coronary flow estimates studied in this work, $q^{\mathrm{US}}_{\mathrm{Guyton}}$, $q^{\mathrm{DeSimone}}_{\mathrm{Guyton}}$, $\hat{q}_{\mathrm{Kishi}}$, and $\hat{q}_{\mathrm{Sharma}}$. We model the hyperemic factor TCRI as a gamma distribution with shape parameter 3, scale factor 0.75, and shifted to 1.[19] For our dataset of 105 FFR measurements, clinically relevant stenoses were quantified in terms of SD using QCA and $\mathrm{QCA_{CT}}$, where $\mathrm{QCA_{CT}}$ denotes QCA evaluated on the basis of segmented geometries. The standard deviation of $\mathrm{QCA}-\mathrm{QCA_{CT}}$ was 20% SD. To account for the uncertainty in stenosis geometry, we introduce a global parameter ΔSD, to be applied to all stenotic regions of a network such that the stenosis degree is given by $\mathrm{SD}=\mathrm{SD}_{\mathrm{segmented}}+\Delta\mathrm{SD}$, where $\mathrm{SD}_{\mathrm{segmented}}$ is the stenosis degree obtained from the original segmentation. Since we adopt a conservative approach where all detected stenoses are included in a global parameter, we model ΔSD as a normal distribution with a mean of 0 and with a standard deviation of 15%.

Sobol sensitivity indices, first-order (S_i) and total ($S_{T,i}$), are widely employed[44] and defined as

$$S_i = \frac{\mathbb{V}[\mathbb{E}[Y \quad |Z_i]]}{\mathbb{V}[Y]}, \tag{16a}$$

$$S_{T,i} = 1 - \frac{\mathbb{V}[\mathbb{E}[Y|\mathbf{Z}_{\neg i}]]}{\mathbb{V}[Y]}. \tag{16b}$$

Here, $\mathbb{E}[Y|\mathbf{Z}_{\neg i}]$ represents the expected value of the output Y for a fixed value of the uncertain input, Z_i, and $\mathbb{V}[X]$ is the variance of some variable, X. $\mathbf{Z}$ is a vector that represents the uncertain input variables, ($\mathbf{Z} = [q, \text{TCRI}, \text{SD}]$), and $\mathbf{Z}_{\neg i}$ contains all elements of $\mathbf{Z}$ except Z_i. SA results (which are obtained on a per patient basis) are summarised by averaging the first-order and total Sobol sensitivity indices over the population. Moreover, we compute weighted first-order sensitivity indices

$$AS_i = \frac{\sum_{k=1}^{n} S_i^k \mathbb{V}[Y_k]}{\sum_{k=1}^{n} \mathbb{V}[Y_k]}, \tag{17}$$

and total sensitivity indices

TABLE 6 Study population characteristics. If not specified, presented results are reported as "mean (standard deviation)"

Characteristic	Units	Mean(std)
Generic data		
No. of patients	-	63
No. of male patients	Datum (percentage)	35 (55.56)
Age	y	59.87 (7.77)
Height	cm	173.62 (10.03)
Weight	kg	85.28 (15.02)
Body mass index	kg/cm^2	28.17 (3.69)
MAP	mmHg	103.48 (10.70)
Cardiac output	L per min	5.07 (0.97)
CAD risk factor	Datum (percentage)	
Diabetes		8 (12.70)
Hypertension		33 (52.38)
Dislipidemia		18 (28.57)
Smoking		11 (17.46)
Previous CAD events		0 (0)
Invasive FFR measurements		
FFR	-	0.81 (0.14)
FFR per vessel prevalence	Datum (percentage)	33/105 (31.43)
FFR per patient prevalence	Datum (percentage)	25/63 (39.68)
Lesions location		
LAD artery	Datum (percentage)	45 (42.86)
RCA	Datum (percentage)	22 (20.95)
LCX artery	Datum (percentage)	13 (12.38)
Diagonals	Datum (percentage)	12 (11.43)
Marginals	Datum (percentage)	8 (7.62)
RPDA	Datum (percentage)	4 (3.81)

[a]Abbreviation: CAD, coronary artery disease; FFR, fractional flow reserve; LAD, left anterior descending; LCX, left circumflex; MAP, mean arterial pressure; RCA, right coronary artery; RPDA, right posterior descending artery.

TABLE 7 LVM and TMM quantification from CCTA. Reported values are average (standard deviation)

Sex	LVM, g	Reference LVM, g[48]	TMM (12)	TMM (14)	Reference TMM[38,39]
Male	141 (21)	116 (20)	211 (32)	338 (51)	331 (56)
Female	108 (19)	85 (14)	162 (28)	259 (45)	245 (52)

[a]Abbreviation: CCTA, coronary computed tomography angiography; LVM, left ventricle mass; TMM, total myocardial mass.

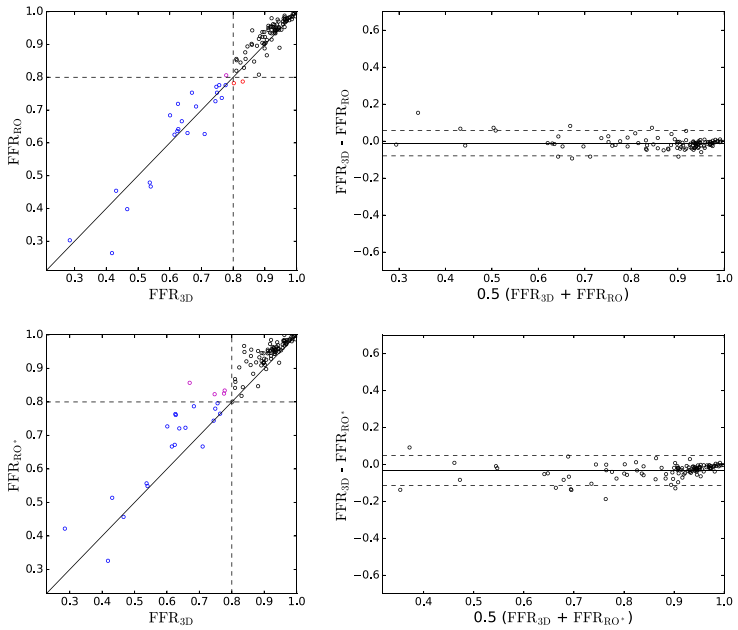

FIGURE 3 Scatter plot and Bland-Altman of FFR_{RO} vs FFR_{3D} (top row) and $FFR_{RO'}$ vs FFR_{3D} (bottom row). The rest of the settings are single branch treatment, q^{US}_{Guyton} baseline flow, and DM flow distribution. DM, distal Murray; FFR, fractional flow reserve; RO, reduced-order; US, ultrasound

$$AS_{T,i} = \frac{\sum_{k=1}^{n} S^{k}_{T,i} \mathbb{V}[Y_k]}{\sum_{k=1}^{n} \mathbb{V}[Y_k]}, \tag{18}$$

where Si^k and $S^k_{T,i}$ are the sensitivities due to input i for FFR-prediction k, and $\mathbb{V}[Y_k]$ is the variance of FFR-prediction k.[19,45]

Measures of uncertainty and sensitivity are estimated by the Monte Carlo method as described by Saltelli,[46] and the accuracy of UQ&SA results are assessed by evaluating the standard deviation of the estimates from 10 bootstrapped samples[47] until the standard deviation is below 0.033 (ie, 99% confident that obtained value is within ±0.1.).

TABLE 8 Comparison of FFR_{RO} vs FFR_{3D} and $FFR_{RO'}$ vs FFR_{3D} for selected 1D settings. Settings are single branch treatment, q^{US}_{Guyton} baseline flow, and DM flow distribution

Terminal	RO Model Version	*a*	*b*	*r*	$FFR_X - FFR_{3D}$	Acc.	Sen.	Spe.	PPV	NPV
Resistive	X=RO	1.06	−0.04	0.98	−0.01 (0.03)	97.14	95.65	97.56	91.67	98.77
	X=RO*	0.89	0.12	0.96	−0.03 (0.04)	96.19	82.61	100	100	95.35
3D flows	X=RO	1.05	−0.03	0.94	−0.013 (0.056)	96.19	95.65	96.34	88.00	98.75
	X=RO*	0.77	0.24	0.90	−0.043 (0.061)	92.38	65.22	100.00	100.00	91.11

Note. *a* and *b* are coefficients for linear fitting: $FFR_X = a\,FFR_{3D} + b$, while *r* is Pearson correlation coefficient.

Abbreviation: DM, distal Murray; FFR, fractional flow reserve; RO, reduced-order; US, ultrasound.

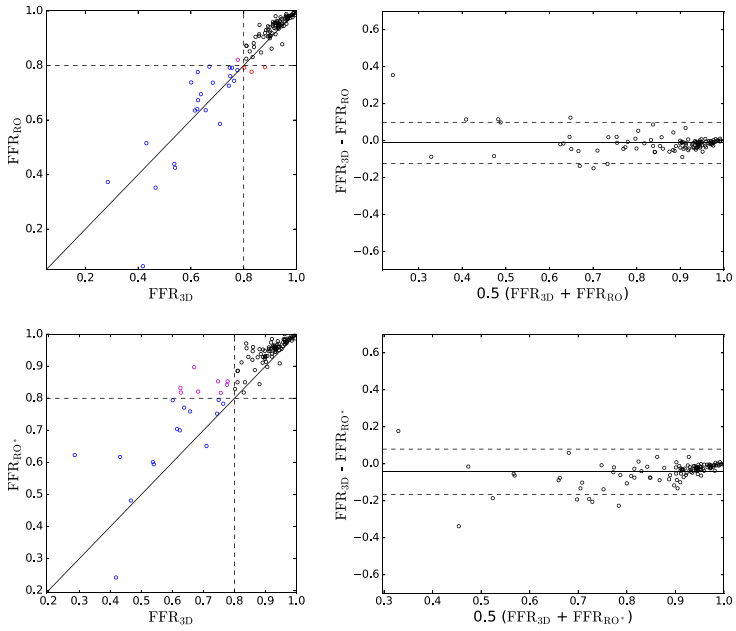

FIGURE 4 Scatter plot and Bland-Altman of FFR_{RO} vs FFR_{3D} (top row) and FFR_{RO^*} vs FFR_{3D} (bottom row). The rest of the settings are single branch treatment, q^{US}_{Guyton} baseline flow, and DM flow distribution. FFR_{RO} and FFR_{RO^*} were obtained by prescribing the hyperemic outlet flows from the 3D solution instead of running the FFR-pipeline described in Section 2.4. DM, distal Murray; FFR, fractional flow reserve; RO, reduced-order; US, ultrasound

3 | RESULTS

3.1 | Patient population and invasive measurements characteristics

A total of 63 patients that underwent invasive angiography and FFR measurements after clinical and CCTA examinations indicated stable CAD were recruited. From these patients, a total of 105 FFR measurements were collected. FFR measurements had a mean of 0.81 and a standard deviation of 0.14, with a per vessel positive FFR prevalence of 31.43% and a per patient positive FFR prevalence of 39.68% for a cut-off value of $FFR \leq 0.8$. See Table 6 for a summary of population characteristics.

Table 7 shows a comparison of LVM for the study population versus reference values taken from a large CT study for healthy young subjects.[48]

TABLE 9 Comparison of FFR_A vs FFR_B for selected cases where FFR_{3D} was available. Other settings common to all simulations are single branch treatment and q^{US}_{Guyton} baseline flow

Comparison Type	Flow Distribution	*a*	*b*	*r*	$FFR_A - FFR_B$	Acc.	Sen.	Spe.	PPV	NPV
RO vs 3D	DM	1.06	−0.04	0.98	−0.01 (0.03)	97.14	95.65	97.56	91.67	98.77
	PM	1.06	−0.04	0.98	−0.01 (0.03)	95.24	84.62	98.73	95.65	95.12
	TAG	1.08	−0.05	0.98	−0.01 (0.04)	94.29	80.00	100.00	100.00	92.59
RO vs invasive measurement	DM	0.64	0.34	0.58	−0.05 (0.13)	81.90	57.58	93.06	79.17	82.72
	PM	0.63	0.34	0.57	−0.04 (0.14)	80.95	54.55	93.06	78.26	81.71
	TAG	0.77	0.21	0.62	−0.03 (0.14)	83.81	60.61	94.44	83.33	83.95
3D vs invasive measurement	DM	0.62	0.35	0.60	−0.04 (0.12)	80.95	54.55	93.06	78.26	81.71
	PM	0.64	0.33	0.62	−0.03 (0.12)	81.90	60.61	91.67	76.92	83.54
	TAG	0.75	0.22	0.66	−0.01 (0.12)	83.81	69.70	90.28	76.67	86.67

Note. *a* and *b* are coefficients for linear fitting: $FFR_A = a\,FFR_B + b$, while *r* is Pearson correlation coefficient.

Abbreviation: DM, distal Murray; FFR, fractional flow reserve; PM, proximal Murray; RO, reduced-order; TAG, transluminal attenuation gradient; US, ultrasound.

TABLE 10 Comparison of total baseline coronary flow, q, and coronary perfusion assuming TMM is 1.5 or 2.4 times LVM

	q^{US}_{Guyton}	$q^{DeSimone}_{Guyton}$	$\bar{q}^{US}_{Guyton}$	$q_{Sakamoto}$	q_{Kishi}	$\hat{q}_{Kishi}$	q_{Sharma}	$\hat{q}_{Sharma}$
q, mL/min	227±42	278±53	229±0	270±1	151±32	241±52	93±27	261±77
q/(1.5×LVM), mL/g/min	1.2±0.3	1.5±0.5	1.3±0.3	1.5±0.3	0.8±0.0	1.3±0.0	0.5±0.1	1.4±0.3
q/(2.4×LVM), mL/g/min	0.8±0.2	1.0±0.3	0.8±0.2	0.9±0.2	0.5±0.0	0.8±0.0	0.3±0.1	0.9±0.2

Note. Reported values are averages (standard deviation) for all 63 patients.

Abbreviation: LVM, left ventricle mass; TMM, total myocardial mass.

3.2 | Validation of reduced-order model versus 3D

Figure 3 shows scatter plots and Bland-Altman plots for a comparison of FFR predicted by 3D and reduced-order models, while a numerical characterisation of the comparison is given in Table 8. The modelling setup used to obtain such results was described in Section 2.4, while the particular model parameter definition used included single branch treatment, q^{US}_{Guyton} baseline coronary flow, and DM flow distribution. Results are shown for the domain definition setup described in Fossan et al[19] and the modified version proposed here. Figure 4 and Table 8 show results for FFR predictions obtained with current method and the one originally proposed in Fossan et al[19] for the case in which the hyperemic simulation is performed replacing resistive elements at outlets with the flows extracted from 3D simulations.

Table 9 reports indexes on the agreement of predicted FFR by the reduced-order model with respect to results obtained using 3D simulations, as well as comparisons of reduced-order model predicted FFR and 3D model predicted FFR versus invasive measurements, for the three flow distribution strategies considered in this work.

3.3 | Baseline coronary flow and FFR prediction by different strategies

Table 10 shows resulting baseline coronary flows and perfusion indexes for strategies proposed in Section 2.5.

Table 11 shows accuracy indexes for predicted FFR with respect to invasive FFR for all possible combinations of baseline flow estimation and flow distribution strategies. Only results using q_{Kishi} and q_{Sharma} are not reported, since baseline flows obtained with these two methods resulted in values well below physiological ranges with 151±32mL/min and 93±27mL/min for q_{Kishi} and q_{Sharma}, respectively (see Table 10). Moreover, Table 12 shows results for coupled branches treatment and $\bar{q}^{US}_{Guyton}$ baseline flow on a per vessel basis, differentiating results among (major branches departing from) left anterior descending artery (LAD), left circumflex artery (LCX), and right coronary artery (RCA).

3.4 | UQ and SA

Figure 5 shows results from the sensitivity analysis described in Section 2.7 in terms of the averaged and uncertainty weighted (see (17) and (18)) sensitivity indices. In the top panel, we have summarised the sensitivity indices when all 105 cases are considered, whereas in the bottom panel, only cases (N=37) where average predicted FFR is $0.7<FFR_{RO}<0.9$ are considered.

4 | DISCUSSION

4.1 | Patient population and derived measurements

The study population is considered representative for patients with suspected CAD being referred for CCTA.

Since two of the methods to determine baseline coronary flow introduced in Section 2.5 depend on TMM, it is important to discuss results presented in Table 7. We observe that average LVM values for males and females are normally larger than the ones reported as reference values for healthy subjects in Fuchs et al.[48] The higher-than-reference LVM values observed for the population under study are supported by reported left ventricle hypertrophy in patients with stable treated chest angina[49] and by the fact that elevated LVM is a recognised marker for cardiovascular risk.[50] Moreover, TMM values obtained using relation (12) are well below reference values, while usage of relation (14) produces TMM estimates slightly above TMM reference values, in line with what is observed for LVM values. This apparent underestimation of TMM by relation (12) will have an impact in flow computations, as we will discuss later in Section 4.3.

TABLE 11 Comparison of FFR_{RO} vs FFR_m for all cases with exception of those obtained using q_{Kishi} and q_{Sharma}; see text for motivation

Branch Treatment	Baseline Flow	Flow Distribution	*a*	*b*	*r*	$FFR_{RO}-FFR_m$	Acc.	Sen.	Spe.	PPV	NPV
Single	q^{US}_{Guyton}	DM	0.64	0.34	0.58	−0.05 (0.13)	81.90	57.58	93.06	79.17	82.72
		PM	0.63	0.34	0.57	−0.04 (0.14)	80.95	54.55	93.06	78.26	81.71
		TAG	0.77	0.21	0.62	−0.03 (0.14)	83.81	60.61	94.44	83.33	83.95
	$q^{DeSimone}_{Guyton}$	DM	0.72	0.25	0.57	−0.02 (0.15)	81.90	63.64	90.28	75.00	84.42
		PM	0.71	0.25	0.57	−0.02 (0.15)	79.05	57.58	88.89	70.37	82.05
		TAG	0.87	0.11	0.61	0.00 (0.15)	82.86	69.70	88.89	74.19	86.49
	$\bar{q}^{US}_{Guyton}$	DM	0.66	0.32	0.57	−0.05 (0.14)	81.90	57.58	93.06	79.17	82.72
		PM	0.65	0.33	0.56	−0.04 (0.14)	80.95	57.58	91.67	76.00	82.50
		TAG	0.79	0.19	0.61	−0.02 (0.14)	86.67	69.70	94.44	85.19	87.18
	$q_{Sakamoto}$	DM	0.75	0.23	0.58	−0.03 (0.15)	84.76	69.70	91.67	79.31	86.84
		PM	0.73	0.24	0.58	−0.02 (0.15)	82.86	69.70	88.89	74.19	86.49
		TAG	0.88	0.10	0.62	0.00 (0.15)	84.76	72.73	90.28	77.42	87.84
	$\hat{q}_{Kishi}$	DM	0.64	0.33	0.57	−0.04 (0.14)	83.81	63.64	93.06	80.77	84.81
		PM	0.63	0.34	0.55	−0.04 (0.14)	83.81	63.64	93.06	80.77	84.81
		TAG	0.77	0.20	0.60	−0.02 (0.14)	85.71	66.67	94.44	84.62	86.08
	$\hat{q}_{Sharma}$	DM	0.67	0.31	0.56	−0.04 (0.14)	81.90	60.61	91.67	76.92	83.54
		PM	0.65	0.32	0.56	−0.03 (0.14)	82.86	60.61	93.06	80.00	83.75
		TAG	0.80	0.17	0.60	−0.01 (0.15)	83.81	60.61	94.44	83.33	83.95
Coupled	q^{US}_{Guyton}	DM	0.67	0.31	0.55	−0.04 (0.15)	80.00	54.55	91.67	75.00	81.48
		PM	0.63	0.34	0.53	−0.04 (0.15)	78.10	48.48	91.67	72.73	79.52
		TAG	0.87	0.11	0.61	−0.01 (0.16)	86.67	78.79	90.28	78.79	90.28
	$q^{DeSimone}_{Guyton}$	DM	0.76	0.22	0.54	−0.02 (0.17)	82.86	66.67	90.28	75.86	85.53
		PM	0.70	0.26	0.52	−0.01 (0.16)	81.90	63.64	90.28	75.00	84.42
		TAG	0.95	0.02	0.61	0.02 (0.17)	85.71	78.79	88.89	76.47	90.14
	$\bar{q}^{US}_{Guyton}$	DM	0.70	0.29	0.54	−0.04 (0.15)	80.95	57.58	91.67	76.00	82.50
		PM	0.65	0.32	0.53	−0.04 (0.15)	77.14	42.42	93.06	73.68	77.91
		TAG	0.91	0.08	0.61	−0.00 (0.16)	88.57	78.79	93.06	83.87	90.54
	$q_{Sakamoto}$	DM	0.78	0.20	0.55	−0.02 (0.16)	82.86	66.67	90.28	75.86	85.53
		PM	0.73	0.24	0.54	−0.01 (0.16)	80.95	60.61	90.28	74.07	83.33
		TAG	0.98	0.00	0.63	0.02 (0.17)	83.81	78.79	86.11	72.22	89.86
	$\hat{q}_{Kishi}$	DM	0.68	0.30	0.55	−0.04 (0.15)	82.86	63.64	91.67	77.78	84.62
		PM	0.63	0.34	0.51	−0.03 (0.15)	81.90	57.58	93.06	79.17	82.72
		TAG	0.88	0.10	0.60	−0.00 (0.16)	87.62	78.79	91.67	81.25	90.41
	$\hat{q}_{Sharma}$	DM	0.70	0.28	0.54	−0.03 (0.15)	82.86	63.64	91.67	77.78	84.62
		PM	0.64	0.32	0.51	−0.03 (0.16)	79.05	54.55	90.28	72.00	81.25
		TAG	0.88	0.09	0.59	0.00 (0.16)	87.62	78.79	91.67	81.25	90.41

Note. For each column representing different accuracy measures, we have highlighted the best (green), second best (blue), and third best (red) measures. *a* and *b* are coefficients for linear fitting: $FFR_{RO}=a\,FFR_m+b$, while *r* is Pearson correlation coefficient.

Abbreviation: DM, distal Murray; FFR, fractional flow reserve; PM, proximal Murray; TAG, transluminal attenuation gradient.

TABLE 12 Comparison of FFR_{RO} vs FFR_m for different coronary segments. The rest of the settings are: coupled branches treatment and $\bar{q}^{US}_{Guyton}$ baseline flow

Coronary segments	Flow Distribution	a	b	r	$FFR_{RO}-FFR_m$	Acc.	Sen.	Spe.	PPV	NPV
All	DM	0.70	0.29	0.54	−0.04 (0.15)	80.95	57.58	91.67	76.00	82.50
	PM	0.65	0.32	0.53	−0.04 (0.15)	77.14	42.42	93.06	73.68	77.91
	TAG	0.91	0.08	0.61	−0.00 (0.16)	88.57	78.79	93.06	83.87	90.54
LAD	DM	0.72	0.29	0.56	−0.06 (0.15)	80.70	57.14	94.44	85.71	79.07
	PM	0.74	0.27	0.60	−0.06 (0.14)	77.19	38.10	100.00	100.00	73.47
	TAG	1.02	−0.01	0.70	−0.01 (0.14)	91.23	80.95	97.22	94.44	89.74
LCX	DM	0.58	0.34	0.44	−0.00 (0.21)	71.43	57.14	78.57	57.14	78.57
	PM	0.38	0.51	0.32	−0.02 (0.22)	66.67	42.86	78.57	50.00	73.33
	TAG	0.73	0.17	0.46	0.05 (0.25)	76.19	85.71	71.43	60.00	90.91
RCA	DM	0.90	0.11	0.72	−0.03 (0.08)	88.46	60.00	95.24	75.00	90.91
	PM	1.11	−0.10	0.75	0.01 (0.09)	84.62	60.00	90.48	60.00	90.48
	TAG	0.54	0.43	0.55	−0.03 (0.08)	92.31	60.00	100.00	100.00	91.30

Note. For each column representing different accuracy measures, we have highlighted the best (green), second best (blue), and third best (red) measures. *a* and *b* are coefficients for linear fitting: $FFR_{RO}=a\,FFR_m+b$, while *r* is Pearson correlation coefficient.

Abbreviation: DM, distal Murray; FFR, fractional flow reserve; PM, proximal Murray; TAG, transluminal attenuation gradient.

4.2 | Validation of reduced-order model

Validation of the reduced-order model using a 3D model as reference is significantly more extensive than previously published results. In Fossan et al,[19] an earlier version of the reduced-order model described here was validated on a population of 13 patients and 23 FFR measurements for a single flow configuration. Moreover, in Blanco et al,[17] a population of 20 patients and 32 FFR measurements for a single flow configuration was considered. Here, we consider 63 patients, 105 FFR measurements, and three different flow configurations.

Results depicted in Figure 3 show that the agreement between predicted FFR values by both models is satisfactory, as confirmed by results reported in Table 8. It is worth noting that the presented results allow to make a two-fold assessment of the reduced-order model results. On one hand, while using resistive elements at terminals, we can see how the entire modelling pipeline described in Section 2.4 is affected by using a simpler and computationally cheaper model with respect to using the 3D model. On the other hand, by imposing terminal flows from the results obtained using

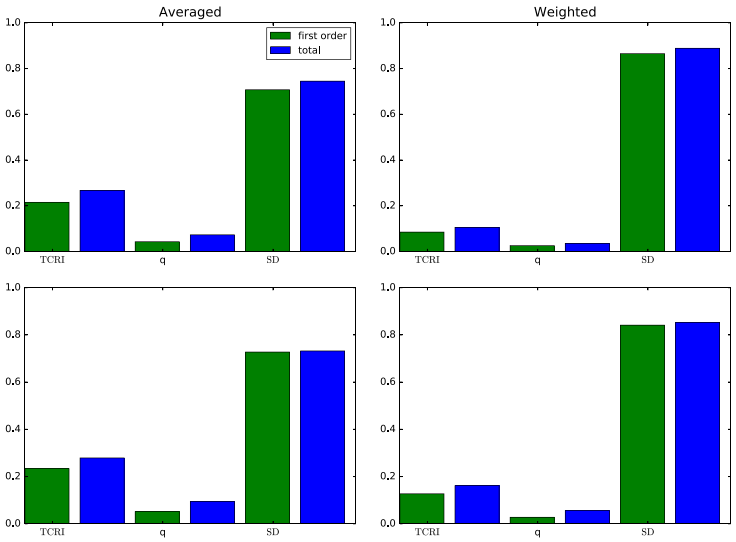

FIGURE 5 The average first-order and total sensitivity indices. The top two bar plots represent sensitivities when all 105 cases were considered, whereas in the bottom two, only cases (N=37) where fractional flow reserve (FFR) is in the critical region $0.7<FFR_{RO}<0.9$ are considered

the 3D model, we can focus on how well the reduced-order model reproduces pressure drops for fixed flows. As it can be clearly seen, the mismatch between results obtained using both models are larger in the case of prescribed flows at outlets of the reduced-order model. Consequently, this is the case where the benefits obtained by modifications to the original model proposed in Fossan et al[19] can be better observed. Furthermore, results reported in Table 9 show that predicted FFR deviations of the reduced-order model with respect to FFR predicted with the 3D model are small compared with errors in FFR prediction versus invasive measurements with bias (standard deviation) of −0.01 (0.03) and −0.05 (0.13) for FFR_{3D} versus FFR_{RO} and FFR_m versus FFR_{RO}, respectively. Importantly, when comparing diagnostic accuracy indexes for reduced-order and 3D model predicted FFR versus invasive measurements, one can see that these are only marginally affected by the used model. These considerations allow us to conclude that results discussed in the following sections are mostly affected by the different modelling hypotheses used (boundary conditions) and not by errors in the description of the fluid mechanics introduced by the reduced-order model. Nevertheless, we note that the disagreement between reduced-order model results and 3D model results leaves room for further reduced-order model improvement, as discussed in Section 4.5.

4.3 | Baseline coronary flow and FFR prediction by different strategies

4.3.1 | Predicted baseline coronary flow

When comparing FFR predictions by different model setups made in Section 3.3, we have excluded results obtained using baseline coronary flows q_{Sharma} and q_{Kishi}. The reason for this choice can be inferred from average baseline coronary flows reported in Table 10. In fact, predicted average flows for q_{Sharma} and q_{Kishi}, as well as average myocardium perfusion rate for q_{Sharma}, are well below physiological values of 250 mL/min and 0.8 mL/g/min.[34] Moreover, it is remarkable how these quantities are in line with reference values for methods using relation (14) to compute TMM and where flow is not derived from perfusion rates, ie, q^{US}_{Guyton}, $q^{DeSimone}_{Guyton}$, $q_{Sakamoto}$, and $\hat{q}_{Sharma}$.

4.3.2 | Effect of baseline coronary flow and its distribution on FFR prediction

Results presented in Table 11 clearly show that the flow distribution strategy for which our reduced-order model delivers better agreement with invasive measurements is the one based on TAG. In fact, linear fit coefficients and Pearson correlation coefficient are always better for TAG for fixed branch treatment and baseline flow estimation strategy. A closer look into how flow distribution methods effect FFR prediction on a vessel basis can be done from data shown in Table 12. Here, it becomes evident that TAG outperforms other flow distribution strategies for LAD and LCX but not for RCA. The overall better performance is due to the fact that lesions located in LAD and LCX (and their branches) account for almost 83 % of total lesion number, in combination with the fact that TAG systematically results in more blood flowing into the LAD with respect to flows obtained with DM and Proximal Murray (PM). For example, for coupled branches treatment and $\bar{q}^{US}_{Guyton}$, average (standard deviation) flow in the LAD are 74 (26), 71 (26), and 89 (32)mL/min for DM, PM, and TAG flow distribution strategies, respectively. Such a pattern can be observed for all simulations reported in Table 11. The larger flow can compensate for underestimated stenosis severity or it can simply mean that TAG is better reflecting the flow distribution among vessels. This last observation is supported by the fact that TAG incorporates patient-specific information about flow distribution (via intensity gradients along vessels), while DM and PM are based on geometrical information alone.

The best performing method in terms of correlation to invasive measurements has the following setting: coupled branches treatment, $q_{Sakamoto}$, and TAG flow distribution. On the other hand, the best method in terms of diagnostic accuracy has the following setting: coupled branches treatment, $\bar{q}^{US}_{Guyton}$, and TAG flow distribution. Since this last method ranks second in terms of linear fitting coefficients, we will denote it as FFR^{OPT}_{RO} throughout the rest of this work.

Diagnostic performance for different modelling choices can vary significantly. In particular, sensitivity among explored model setups varies between 48.48% and 78.79%. It is interesting to observe that maximum sensitivity (78.79%) is achieved for coupled branches treatment, TAG flow distribution, and all baseline coronary flow estimation methods, pointing out to the fact that flow distribution is more determinant than baseline coronary flow estimation.

Although errors ($FFR_{RO}-FFR_m$) standard deviation varies for different model setups, such fluctuations are very small with respect to standard deviation absolute values, with larger variations among results obtained using different baseline flow definition methods rather than within single baseline flow definition methods. In other words, standard

TABLE 13 Comparison of FFR_{RO} vs FFR_m for different ways of estimating the proximal boundary condition. The rest of the settings are coupled branches treatment, $\bar{q}^{US}_{Guyton}$ baseline flow, and TAG flow distribution

Inlet pressure	*a*	*b*	*r*	$FFR_{RO}-FFR_m$	Acc.	Sen.	Spe.	PPV	NPV
Clinic	1.03	−0.03	0.65	0.00 (0.16)	89.47	79.31	93.94	85.19	91.18
100	1.02	−0.02	0.65	0.00 (0.16)	88.42	79.31	92.42	82.14	91.04
Invasive	1.04	−0.04	0.66	0.00 (0.16)	88.42	79.31	92.42	82.14	91.04

[a]: FFR, fractional flow reserve; TAG, transluminal attenuation gradient.

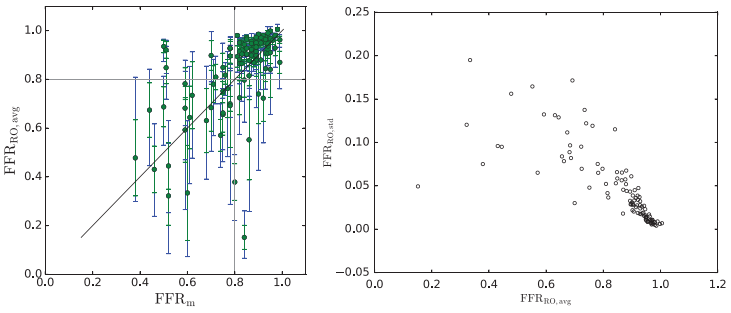

FIGURE 6 Left panel shows a scatter plot of $FFR_{RO,avg}$ vs FFR_m, where $FFR_{RO,avg}$ is the average FFR predicted from the simulations summarised in Table 11. The range (blue) of predicted FFR_{RO} and standard deviation, $FFR_{RO,std}$ (green) are also indicated by the vertical error bars. Right panel shows $FFR_{RO,std}$ as a function of $FFR_{RO,avg}$

deviation changes seem to be mainly due to the use of different baseline flow estimation methods, rather than by flow distribution strategies. Another conclusion that can be made from standard deviation variation across used modelling setups is that none of the investigated methods seems to reduce error standard deviation significantly, although several of them imply using patient-specific information. This result is not surprising if one considers the origin of patient-specific information used by the different methods. In q^{US}_{Guyton}, we use ultrasound-derived CO, for which measurement errors of 690mL/min have been reported. Such errors propagate to baseline coronary flow, which, in this case, is computed as 4.5 % of CO and imply an error in flow of approximately 31 mL/min or 14 % of baseline coronary flow. The standard deviation of q^{US}_{Guyton} in our population is 42 mL/min and is thus comparable with the measurement error. Another method using CO estimates is $q^{DeSimone}_{Guyton}$, where the formula for determining stroke volume (7) was obtained by fitting experimental data, with a resulting Pearson correlation coefficient r=0.45, [33] denoting large uncertainty in predicted values. Moving forward among methods, we consider now $\hat{q}_{Sharma}$. In this case, (13) is used. This relation involves a fitting of experimental data (on dogs) relating HR and SBP to oxygen consumption, with r=0.87, [51] combined then to another fitting of experimental data on the relation between coronary flow and oxygen consumption.[52] There are additional sources of errors for these patient-specific baseline flow estimation methods. The fraction of CO that flows into the coronaries, γ in (10), is assumed constant. Moreover, as already discussed, some methods make use of SBP and HR. These quantities are known to vary for the same patient depending on many factors. For our patient population, we observe that Pearson correlation coefficients for SBP and HR when comparing quantities acquired non-invasively and quantities measured during invasive FFR procedures are 0.09 and 0.29, for SBP and HR, respectively. All these considerations support the results shown here that evidence no benefit in terms of error standard deviation reduction by using patient-specific baseline flow estimation methods. However, this conclusion does not preclude that a better, currently nonreported baseline flow estimation method would result in improved FFR predictions.

Previously reported relative low impact of prescribed inlet pressure in FFR prediction frameworks[19,21] was confirmed in this study. Table 13 shows the completely neglectable impact of using different values for the prescribed inlet pressure, including pressure measured non-invasively, pressure acquired during invasive FFR measurement (the actual value to compute invasive FFR), and a fixed value of 100 mmHg, demonstrating that this parameter is of little importance when predicting FFR.

Figure 6, left panel, shows a scatter plot of invasive FFR versus average predicted FFR (for all methods shown in Table 11), including maximum variation ranges and standard deviation. Average standard deviation is 0.048, with larger values for lower FFR values, as it can be seen in Figure 6, right panel. These results reinforce observations made while analysing data reported in Table 11 on the fact that baseline coronary flow estimation and flow distribution strategies

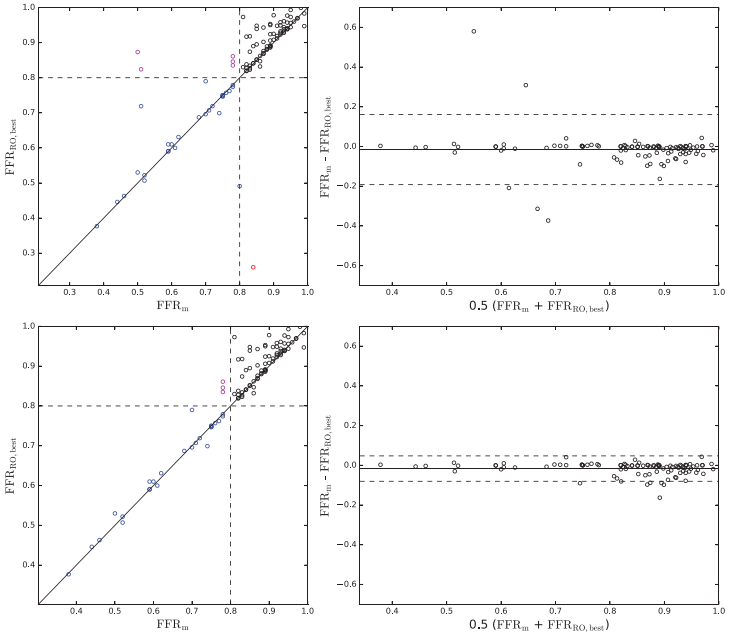

FIGURE 7 Scatter plot and Blant-Altman of $FFR_{RO,best}$ vs FFR_m, where FFR_{best} is the best FFR prediction (in terms of absolute error) from all the simulations summarised in Table 11. The top panel shows results when all measurements are included, whereas those in the bottom row (5) measurements which had errors ($FFR_{RO,best}-FFR_m$) larger than two standard deviations were excluded. $FFR_{RO,best}-FFR_m$ are −0.02 (0.09) and −0.02 (0.03) for the top and bottom panels, respectively. FFR, fractional flow reserve

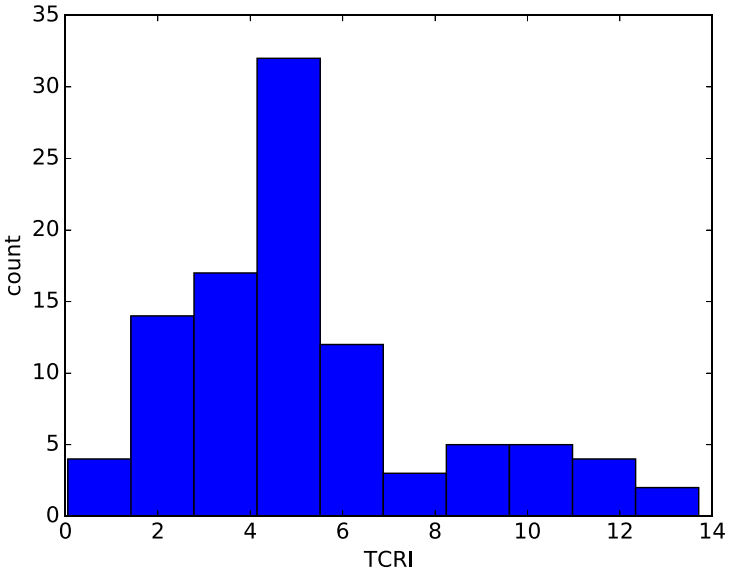

FIGURE 8 Histogram of TCRI, where TCRI in this case is calculated on the basis of the baseline resistance of simulations corresponding to the best performing setting (coupled branches treatment, $\bar{q}^{US}_{Guyton}$ baseline flow, and TAG flow distribution) and hyperemic resistance corresponding to FFR_{best}. Measurement locations which had errors ($FFR_{RO,best}-FFR_m$) larger than two standard deviations where excluded and cases which resulted in TCRI values larger than 15 were excluded from this analyses. FFR, fractional flow reserve; TCRI, total coronary resistance index

have limited impact on overall performance of the FFR prediction framework: Average of predicted FFR standard deviation to baseline flow and flow distribution methods is 0.048 while predicted FFR measurement error standard deviation is 0.15. This fact indicates that the availability of better baseline flow estimation and flow distribution methods will have a significant but limited impact on FFR prediction performance. Such impact can increase if one considers that the precise definition of one of the parameters with larger impact on FFR predictions, the TCRI,[19,21] depends on a baseline condition. These findings are further supported by our sensitivity analysis, where we see that the effect of the uncertainty in baseline coronary flow is rather low, compared with the influence of TCRI and SD. Results indicate

that the uncertainty in the stenosis degree has the largest influence on FFR-prediction uncertainty, with average first-order and total sensitivity indices of 0.71 and 0.74, and uncertainty weighted sensitivity indices of 0.87 and 0.89, respectively. TCRI has a significant but much lower influence with average first-order and total sensitivity indices of 0.22 and 0.27 and uncertainty weighted sensitivity indices of 0.08 and 0.11, respectively. Baseline coronary flow has a minor influence in comparison, with average first order and total sensitivity indices of 0.04 and 0.07 and uncertainty weighted sensitivity indices of 0.03 and 0.04, respectively. The influence of TCRI and q is slightly increased when only cases in the critical region $0.7<FFR_{\mathrm{RO}}<0.9$ are considered. The average standard deviation in predicted FFR is 0.12. However, we note that the uncertainty in how the flow is distributed is not considered and may be seen in relation to the fact that the average standard deviation resulting from the UQ&SA (0.12) is slightly lower than average predicted FFR measurement error standard deviation (0.15).

The above made observations allow us to conclude that other parameters than the ones studied here have to be addressed in order to improve FFR prediction accuracy. In particular, we consider now TCRI and make a post-processing experiment by:

- extracting best matching FFR predictions of all simulations shown in Table 11;
- considering $\mathrm{FFR}_{\mathrm{RO}}^{\mathrm{OPT}}$ as the setting for reference baseline conditions; and
- compute TCRI as the ratio of peripheral resistance (with respect to FFR measurement location) for best matching simulation versus peripheral resistance for reference baseline setting.

Selected best matching predictions versus measurements are shown in Figure 7, while Figure 8 shows a histogram of obtained TCRIs. Such results show that, for the given modelling framework, available segmentations and flows in physiological ranges, rather accurate FFR predictions can be obtained, if a highly variable TCRI is considered. Corresponding accuracy, sensitivity, and specificity are 94%, 85%, and 99% when all measurements are included and 97%, 90%, and 100% when outliers are excluded. Interestingly, TCRI distribution emerging from this analysis reflects the high variability observed in coronary flow reserve, which has shown to display a gamma distribution shape when directly measured on patients.[53]

4.4 | Use of reduced-order models for the development of clinical decision support tools

The capacity of exploring a large number of modelling hypotheses, as well as parameter space via sensitivity analysis, is facilitated by the fact that we use an accurate reduced-order model of the problem under investigation. This fact points to one of the strengths of reduced-order models, which is that of being computationally cheaper and generally more robust than more complex models in terms of numerical issues such as convergence and stability of the overall algorithm. Advantages in terms of problem setup, preprocessing, and postprocessing over more complex models are also relevant. Moreover, errors introduced by reduced-order models can be compensated by the fact that one can explore a larger portion of possible solutions. However, such errors must be acceptable, which in the context of this work means that clinical decisions should not be affected by them.

4.5 | Limitations and future work

The present work has several limitations. The most relevant one is probably the fact that, although we explore certain modelling hypotheses, other are kept fixed and are inherent to our FFR prediction framework (segmentation method, modelling pipeline, etc). This fact is kept in mind throughout the text and only claims that we think are valid for any model-based FFR prediction framework are mentioned as such. The impact of patient-specific TCRI on FFR prediction diagnostic accuracy was only partially addressed. In fact, in Section 4.3.2 we show that a highly variable TCRI would have a significant impact in the diagnostic accuracy of our FFR prediction method. Ideally, we should assess how a patient-specific TCRI computation would perform in comparison to other methods, but to the best of our knowledge, no methodology to estimate TCRI non-invasively and without the use of drugs or additional imaging is currently available. Another component that can vary greatly among patients is total baseline coronary flow. In this case, we have considered quantification methods that depend on patient-specific information such as CO or LVM. However, one should ideally use a direct total baseline coronary flow measurement method. Such methods are being developed in the context of ultrasound imaging and magnetic resonance imaging and, once available, have the potential to provide

highly valuable information for FFR prediction tools. See Fiorentini et al[54] and Schwitter et al[55] for recent developments in ultrasound and magnetic-resonance coronary flow estimation methods.

Another aspect to be considered is the fact that the reduced-order model is not perfectly reproducing 3D model results. Therefore, results are influenced not only by boundary conditions but also by errors in solving fluid mechanics within the computational domain representing epicardial vessels. This is common to any FFR prediction strategy based on reduced-order models. Here, we prefer to be aware of such errors and try to minimise them, rather than to embed them in the modelling framework and lose control on error causes when comparing FFR prediction and invasive measurements.

The prevalence of positive FFR values is not optimal, and one would desire a more homogeneous distribution of invasive FFR values to work with. However, we observe that this is an issue faced by virtually all published works on FFR prediction methods and is probably related to the intrinsic dynamics of how FFR is used in the clinic, with many measurements performed on lesions that reveal to be functionally nonsignificant.

Finally, the results from the UQ & SA depend on the assumed input uncertainties, and here we did not include uncertainties/variability due to differences in how baseline coronary flow is distributed. More importantly, the way in which the uncertainty of the stenosis geometry was modelled, via a global parameter effecting all stenotic regions, may have synthetically increased the influence of this parameter and is not necessarily entirely realistic. Nevertheless, results shown here should still be considered as valid for giving a clear indication to where attention should be focused in order to reduce uncertainty in FFR-prediction.

4.6 | Conclusions and future work

In this work, we have first improved and validated a reduced-order model for FFR prediction and then tested the impact of different methods proposed in the literature to estimate and distribute baseline coronary flow on FFR predictions. Both tasks were performed on a dataset regarding 63 patients with stable CAD and 105 invasive FFR measurements.

The proposed reduced-order model introduces errors with respect to the 3D model, which are significantly smaller than errors observed for predicted FFR versus invasive measurements. Moreover, diagnostic performance was only marginally affected by the use of the reduced-order model for cases in which 3D simulation results were available (63 patients, 105 invasive FFR measurements, 3 different setups for 3D simulations).

We have shown that methods for baseline coronary flow estimation and its distribution can affect the diagnostic performance of an FFR-prediction framework significantly. Moreover, the influence of methods for flow distribution is greater than that of methods for baseline flow estimation, and we find that TAG flow distribution outperforms flow distribution methods based on Murray's law for all tested setups. However, we observe that none of the investigated methods for baseline coronary flow estimation and distribution results in a significant reduction in error standard deviation for predicted FFR versus invasive FFR measurements. Finally, we see that for our modelling framework the diagnostic accuracy on a per-vessel basis can vary significantly.

In future work, we will regard the further improvement of our reduced-order model in terms of its capacity to reproduce the physics of 3D models in a more accurate manner. Moreover, we will look into better ways of characterising baseline coronary flow by means of, for example, non-invasive determination of baseline flow at selected vessels. Finally, we will consider how to better define a patient-specific TCRI, since we think that this factor plays a crucial role in representing patient-specific variability in coronary physiology relevant for FFR prediction.

ACKNOWLEDGEMENTS

This work was partially supported by NTNU Health (Strategic Research Area at the Norwegian University of Science and Technology) and by The Liaison Committee for education, research, and innovation in Central Norway. Computational resources in Norwegian HPC infrastructure were granted by the Norwegian Research Council by Project Nr. NN9545K.

ETHICAL APPROVAL

All procedures performed in studies involving human participants were in accordance with the ethical standards of the institutional and/or national research committee and with the 1964 Helsinki declaration and its later amendments or comparable ethical standards.

ORCID

Fredrik E. Fossan https://orcid.org/0000-0003-0006-5165

REFERENCES

1. Pijls NHJ, Van Gelder B, Van der Voort P, et al. A useful index to evaluate the influence of an epicardial coronary stenosis on myocardial blood flow. *Circulation*. 1995;92(11):3183-3193. https://doi.org/10.1161/01.CIR.92.11.3183
2. Pijls NH, De Bruyne B, Peels K, et al. Measurement of fractional flow reserve to assess the functional severity of coronary-artery stenoses. *N Engl J Med*. 1996;334(26):1703=-1708.
3. Pijls NH, Van Son JA, Kirkeeide R, De Bruyne B, Gould KL. Experimental basis of determining maximum coronary, myocardial, and collateral blood flow by pressure measurements for assessing functional stenosis severity before and after percutaneous transluminal coronary angioplasty. *Circulation*. 1993;87(4):1354-1367.
4. Wilson RF, Wyche K, Christensen BV, Zimmer S, Laxson DD. Effects of adenosine on human coronary arterial circulation. *Circulation*. 1990;82(5):1595-1606. https://doi.org/10.1161/01.CIR.82.5.1595
5. Tonino PA, De Bruyne B, Pijls NH, et al. Fractional flow reserve versus angiography for guiding percutaneous coronary intervention. *N Engl J Med*. 2009;360(3):213-224.
6. Pijls NH, Fearon WF, Tonino PA, et al. Fractional flow reserve versus angiography for guiding percutaneous coronary intervention in patients with multivessel coronary artery disease. *J Am Coll Cardiol*. 2010;56(3):177-184. https://doi.org/10.1016/j.jacc.2010.04.012
7. De Bruyne B, Pijls NH, Kalesan B, et al. Fractional flow reserve-guided PCI versus medical therapy in stable coronary disease. *N Engl J Med*. 2012;367(11):991-1001. https://doi.org/10.1056/NEJMoa1205361
8. 2014 ESC/EACTS Guidelines on myocardial revascularization: The Task Force on Myocardial Revascularization of the European Society of Cardiology (ESC) and the European Association for Cardio-Thoracic Surgery (EACTS)Developed with the special contribution of the European Association of Percutaneous Cardiovascular Interventions (EAPCI). *Eur Heart J*. 2014;35(37):2541-2619. https://doi.org/10.1093/eurheartj/ehu278
9. Patel MR, Peterson ED, Dai D, et al. Low diagnostic yield of elective coronary angiography. *N Engl J Med*. 2010;362(10):886-895. https://doi.org/10.1056/NEJMoa0907272
10. The SCOT-HEART Investigators. Coronary CT angiography and 5-year risk of myocardial Infarction. *N Engl J Med*. 2018;379(10):924-933. https://doi.org/10.1056/NEJMoa1805971
11. NICE. National Institute for Health and care excellence clinical guideline on chest pain of recent onset: assessment and diagnosis; 2010.
12. Rossi A, Papadopoulou SL, Pugliese F, et al. Quantitative computed tomographic coronary angiography: does it predict functionally significant coronary stenoses? *Circ Cardiovasc Imaging*. 2014;7(1):43-51. https://doi.org/10.1161/CIRCIMAGING.112.00027
13. Cook CM, Petraco R, Shun-Shin MJ, et al. Diagnostic accuracy of computed tomography-derived fractional flow reserve: a systematic review. *JAMA Cardiol*. 2017;2(7):803–810. https://doi.org/10.1001/jamacardio.2017.1314
14. Nørgaard BL, Terkelsen CJ, Mathiassen ON, et al. Clinical outcomes using coronary CT angiography and FFRCT guided management of stable chest pain patients. *J Am Coll Cardiol*; 2018;72(18):2123–2134. https://doi.org/10.1016/j.jacc.2018.07.043
15. Itu L, Sharma P, Mihalef V, Kamen A, Suciu C, Lomaniciu D. A patient-specific reduced-order model for coronary circulation. *IEEE*. 2012;■:832-835.
16. Ri K, Kumamaru KK, Fujimoto S, et al. Noninvasive computed tomography-derived fractional flow reserve based on structural and fluid analysis: reproducibility of on-site determination by unexperienced observers. *J Comput Assist Tomogr*. 2017;42(2):256–262. https://doi.org/10.1097/RCT.0000000000000679
17. Blanco PJ, Bulant CA, Müller LO, et al. Comparison of 1D and 3D models for the estimation of fractional flow reserve. *Sci Rep*. 2018;8(1). https://doi.org/10.1038/s41598-018-35344-0
18. Boileau E, Pant S, Roobottom C, et al. Estimating the accuracy of a reduced-order model for the calculation of fractional flow reserve (FFR). *Int J Numer Methods Biomed Eng*. 2018;34(1):e2908. https://doi.org/10.1002/cnm.2908
19. Fossan FE, Sturdy J, Müller LO, et al. Uncertainty quantification and sensitivity analysis for computational FFR estimation in stable coronary artery disease. *Cardiovasc Eng Technol*. 2018;9(4):597–622. https://doi.org/10.1007/s13239-018-00388-w
20. Sankaran S, Kim HJ, Choi G, Taylor CA. Uncertainty quantification in coronary blood flow simulations: impact of geometry, boundary conditions and blood viscosity. *J Biomech*; 2016;49(12):2540-2547. https://doi.org/10.1016/j.jbiomech.2016.01.002
21. Morris PD, Soto DAS, Feher JFA, et al. Fast virtual fractional flow reserve based upon steady-state computational fluid dynamics analysis. *JACC Basic Trans Sci*. 2017;2(4):434-446. https://doi.org/10.1016/j.jacbts.2017.04.003
22. Bråten AT, Wiseth R. Diagnostic accuracy of CT-FFR compared to invasive coronar angiography with fractional flow reserve - full text view - ClinicalTrials. gov; 2017.
23. Gaur S, Øvrehus KA, Dey D, et al. Coronary plaque quantification and fractional flow reserve by coronary computed tomography angiography identify ischaemia-causing lesions. *Eur Heart J*. 2016;37(15):1220-1227. https://doi.org/10.1093/eurheartj/ehv690

24. Yushkevich PA, Piven J, Hazlett HC, Smith RG, Ho S, Gee JC, Gerig G. User-guided 3D active contour segmentation of anatomical structures: significantly improved efficiency and reliability. *NeuroImage*. 2006;31(3):1116-1128. https://doi.org/10.1016/j.neuroimage.2006.01.015
25. Antiga L, Piccinelli M, Botti L, Ene-Iordache B, Remuzzi A, Steinman DA. An image-based modeling framework for patient-specific computational hemodynamics. *Medical & Biological Engineering & Computing*. 2008;46(11):1097-1112. https://doi.org/10.1007/s11517-008-0420-1
26. Srl O. The vascular modeling toolkit website; Accessed: 2017.
27. Seeley BD, Young DF. Effect of geometry on pressure losses across models of arterial stenoses. *J Biomech*. 1976;9(7):439-448. https://doi.org/10.1016/0021-9290(76)90086-5
28. Evju Ø, Alnæs MS. CBCFLOW. Bitbucket repository; 2017.
29. Logg A, Mardal KA, Wells G, eds.. *Automated Solution of Differential Equations by the Finite Element Method. 84 of Lecture Notes in Computational Science and Engineering*. Berlin, Heidelberg: Springer Berlin Heidelberg; 2012.
30. Simo JC, Armero F. Unconditional stability and long-term behavior of transient algorithms for the incompressible Navier-Stokes and Euler equations. *Computer Methods in Applied Mechanics and Engineering*. 1994;111(1–2):111-154. https://doi.org/10.1016/0045-7825(94)90042-6
31. Mortensen M, Valen-Sendstad K. A high-level/high-performance open source Navier-Stokes solver. *Comput Phys Commun*. 2015;188:177-188. https://doi.org/10.1016/j.cpc.2014.10.026
32. Bezerra CG, Hideo-Kajita A, Bulant CA, et al. Coronary fractional flow reserve derived from intravascular ultrasound imaging: validation of a new computational method of fusion between anatomy and physiology. *Catheter Cardiovasc Interv*. 2019;93(2):266-274. https://doi.org/10.1002/ccd.27822
33. de Simone G, Roman MJ, Koren MJ, Mensah GA, Ganau A, Devereux RB. Stroke volume/pulse pressure ratio and cardiovascular risk in arterial hypertension. *Hypertens*. 1999;33(3):800-805. https://doi.org/10.1161/01.HYP.33.3.800
34. Guyton AC, Hall JE. *Textbook of Medical Physiology*. 11th. Philadelphia: Elsevier Saunders; 2006.
35. Kishi S, Giannopoulos AA, Tang A, et al. A framework for personalization of coronary flow computations during rest and hyperemia. *Radiol*. 2017;■:162620. https://doi.org/10.1148/radiol.2017162620
36. Zipes DP, Libby P, Bonow RO, Mann DL, Tomaselli GF, Braunwald E. Braunwald's heart disease: a textbook of cardiovascular medicine. OCLC: 1021152059; 2019.
37. Sharma P, Itu L, Zheng X, et al. A framework for personalization of coronary flow computations during rest and hyperemia. IEEE; 2012:6665-6668.
38. Molina DK, DiMaio VJ. Normal organ weights in men: part I—the heart. *Am J Forensic Med Pathol*. 2012;33(4):362-367. https://doi.org/10.1097/PAF.0b013e31823d298b
39. Molina DK, DiMaio VJ. Normal organ weights in men: part I—the heart. *Am J Forensic Med Pathol*. 2015;36(3):176-181. https://doi.org/10.1097/PAF.0000000000000174
40. Sakamoto S, Takahashi S, Coskun AU, et al. Relation of distribution of coronary blood flow volume to coronary artery dominance. *Am J Cardiol*. 2013;111(10):1420-1424. https://doi.org/10.1016/j.amjcard.2013.01.290
41. Murray CD. The physiological principle of minimum work. *Proc Natl Acad Sci USA*. 1926;12(3):207-214.
42. Taylor CA, Fonte TA, Min JK. Computational fluid dynamics applied to cardiac computed tomography for noninvasive quantification of fractional flow reserve. *J Am Coll Cardiol*. 2013;61(22):2233-2241. https://doi.org/10.1016/j.jacc.2012.11.083
43. Bulant CA. Computational models for the geometric and functional analysis of the coronary circulation. *PhD Thesis*; 2017.
44. Saltelli Andrea. *Global Sensitivity Analysis : The Primer*. Chichester, England: John Wiley,; 2008.
45. Eck VG, Sturdy J, Hellevik LR. Effects of arterial wall models and measurement uncertainties on cardiovascular model predictions. *J Biomech*. 2016;50:188–194. https://doi.org/doi:10.1016/j.jbiomech.2016.11.042
46. Saltelli A. Making best use of model evaluations to compute sensitivity indices. *Comput Phys Commun*. 2002;145(2):280-297.
47. Robert C, Casella G. *Monte Carlo Statistical Methods*. 2nd ed. Springer-Verlag New York: Springer; 2004.
48. Fuchs A, Mejdahl MR, Kühl JT, et al. Normal values of left ventricular mass and cardiac chamber volumes assessed by 320-detector computed tomography angiography in the Copenhagen General Population Study. *European Heart Journal – Cardiovascular Imaging*. 2016;17(9):1009-1017. https://doi.org/10.1093/ehjci/jev337
49. Ang D, Pringle S, Struthers A. The cardiovascular risk factor, left ventricular hypertrophy, is highly prevalent in stable, treated angina pectoris. *Am J Hypertens*. 2007;20(10):1029-1035. https://doi.org/10.1016/j.amjhyper.2007.04.021
50. Abdi-Ali A, Miller RJH, Southern D, et al. LV mass independently predicts mortality and need for future revascularization in patients undergoing diagnostic coronary angiography. *JACC Cardiovasc Imaging*. 2018;11(3):423-433. https://doi.org/10.1016/j.jcmg.2017.04.012
51. Baller D, Bretschneider HJ, Hellige G. Validity of myocardial oxygen consumption parameters. *Clin Cardiol*. 1979;2(5):317-327.
52. Rubio R, Berne RM. Regulation of coronary blood flow. *Prog Cardiovasc Dis*. 1975;18(2):105-122. https://doi.org/10.1016/0033-0620(75)90001-8

53. Matsuda J, Murai T, Kanaji Y, et al. Prevalence and clinical significance of discordant changes in fractional and coronary flow reserve after elective percutaneous coronary intervention. *J Am Heart Assoc*. 2016;5(12). https://doi.org/10.1161/JAHA.116.004400

54. Fiorentini S, Saxhaug L, Bjåstad T., Holte E, Torp H, Avdal J. 3D tracking Doppler for improved quantitative blood flow assessment of coronary arteries. *2017 IEEE International Ultrasonics Symposium (IUS)*. 2017;■:1-4.

55. Schwitter J, DeMarco T, Kneifel S, et al. Magnetic resonance-based assessment of global coronary flow and flow reserve and its relation to left ventricular functional parameters : a comparison with positron emission tomography. *Circulation*. 2000;101(23):2696-2702. https://doi.org/10.1161/01.CIR.101.23.2696

How to cite this article: Müller LO, Fossan FE, Bråten AT, Jørgensen A, Wiseth R, Hellevik LR. Impact of baseline coronary flow and its distribution on fractional flow reserve prediction. *Int J Numer Meth Biomed Engng*. 2019;e3246. https://doi.org/10.1002/cnm.3246

Chapter 9

Machine learning augmented reduced order model for FFR-prediction

The content of this chapter was will be submitted to
Computer Methods in Applied Mechanics and Engineering, 2020.

Machine learning augmented reduced order model for FFR-prediction

F.E. Fossan, L.O. Müller, J. Sturdy, A. Bråten, A. Jørgensen, R. Wiseth, L.R. Hellevik